ABSTRACT

Title of dissertation: QUANTUM INFORMATION PROCESSING WITH TRAPPED ION CHAINS

Timothy Andrew Manning,
Doctor of Philosophy, 2014

Dissertation directed by: Professor Christopher Monroe
Joint Quantum Institute,
University of Maryland Department of Physics
and
National Institute of Standards and Technology

Trapped atomic ion systems are currently the most advanced platform for quantum information processing. Their long coherence times, pristine state initialization and detection, and precisely controllable and versatile interactions make them excellent quantum systems for experiments in quantum computation and quantum simulation. One of the more promising schemes for quantum computing consists of performing single and multi-qubit quantum gates on qubits in a linear ion crystal. Some of the key challenges of scaling such a system are the individual addressing of arbitrary subsets of ions and controlling the growing complexity of motional mode interactions as the number of qubits increases or when the gates are performed faster. Traditional entangling quantum gates between ion qubits use laser pulses to couple the qubit states to the collective motion of the crystal, thereby generating a spin-spin interaction that can produce entanglement between selected qubits. The intrinsic limitations on the performance of gates using this method can be allevi-

ated by applying optimally shaped pulses instead of pulses with constant amplitude. This thesis explains the theory behind this pulse shaping scheme and how it is implemented on a chain of $^{171}Yb^{+}$ ions held in a linear radiofrequency 'Paul' trap. Several experiments demonstrate the technique in chains of two, three, and five ions using various types of pulse shapes. A tightly focused individual addressing beam allows us to apply the entangling gates to a target pair of ions, and technical issues related to such tight focusing are discussed. Other advantages to the pulse shaping scheme include a robustness against detuning errors and the possibility of suppressing undesirable coupling due to optical spillover on neighboring ions. Combined with ion shuttling, we harness these features to perform sequential gates to different qubit pairs in order to create genuine tripartite entangled states and demonstrate the programmable quantum information processing capability of our system.

Quantum information processing with trapped ion chains

by

Timothy Andrew Manning

Dissertation submitted to the Faculty of the Graduate School of the
University of Maryland, College Park in partial fulfillment
of the requirements for the degree of
Doctor of Philosophy
2014

Advisory Committee:
Professor Christopher Monroe, Chair/Advisor
Professor Steve Rolston
Professor Edo Waks
Dr. Ian Spielman
Dr. Gretchen Campbell
Dr. Alexey Gorshkov

Foreword

The work presented in this thesis encompasses only the last two years of my graduate research at the University of Maryland. I joined the lab just as my advisor moved his research group from the University of Michigan to join the Joint Quantum Institute at Maryland. The first three years were devoted to building a cavity QED experiment literally from the ground up. While I worked on the design and machining of the novel ion trap and Fabry-Pérot optical cavity assembly, we were also building shelves and setting up an entire table of lasers and optics from scratch. There were many risks associated with combining a novel ion trap, the electrodes of which could be moved independently *in situ*, with a high finesse optical cavity with dielectric mirror coatings for both ultraviolet and infrared wavelengths. The dream of distributed quantum networks of trapped ions, where material quantum memories are connected by photonic links via heralded entanglement, is significantly hindered by low photon collection efficiencies. Our goal was to couple a single ion to an optical cavity mode in order to use the Purcell effect to extract fluorescence much more efficiently than what is possible with free-space emission. Unfortunately, after years of building the lab and bringing the project to fruition, the combination of several independent problems put an end to the project. We were able to publish one paper from the ion cavity research [1] before retiring it. The next year I worked on a project more closely related to the work in this thesis: the realization of an entangling gate on a chain of trapped ions using a new micro-fabricated surface "chip" trap designed and constructed by the ion trapping group at Sandia National Laboratory. There is much hope surrounding the continuing advance of professionally microfabricated

ion traps that can be plugged into a vacuum chamber socket assembly much like a classical computer processor can be plugged into a motherboard. We successfully trapped $^{171}Yb^{+}$ ions and were on the verge of performing Raman transitions using a 355 nm pulsed laser, but fundamental design limitations prevented us from going further due to unavoidable charging from the Raman beams. So, we switched to an old cadmium ion chamber designed for the first experiments shuttling ions around a junction in 2006. The chamber was retrofitted with Yb ovens in 2009, but sat on the shelf until November 2011 when we installed it on the table. By January 2012 we were loading $^{171}Yb^{+}$ ions and beginning to align Raman beams. A few months later we were performing entangling gates using the pulse shaping technique that is the foundation of this thesis. Our progress from this point was fairly rapid, given the complexity of the hardware and software development that the experiments detailed in the following pages demanded. The next iteration of the experiment coming online soon promises an exciting future for the lab.

To my family

Acknowledgments

It is customary to acknowledge many people by name with detailed personal accounts of how they contributed to and shaped one's graduate research experience. I will break with that tradition because I have worked with so many good people at the University of Maryland I don't want to risk omitting anyone. There are a few people I will specifically acknowledge, though, because it would simply be absurd not to. The first is my advisor, Dr. Chris Monroe. He has consistently been an engaged and practically helpful leader, both for the research group as a whole and for my research projects. He manages to balance the need to give his researchers the freedom to take ownership of their projects with the guidance necessary sometimes to keep them from floundering. I am sincerely grateful to him for the opportunity I've had to work with and learn from him and his preeminent research group. Over the years I worked closely with two distinct sets of lab mates. For the first few years I worked with graduate student Jon Sterk and postdoctoral researcher Dr. Le Luo primarily on a very risky and technically challenging cavity QED project. Together we built the lab completely from scratch, and I learned the foundation of my ion trapping expertise from them. The last half of my career was spent with graduate student Shantanu Debnath and postdoctoral researcher Dr. Taeyoung Choi. They are both talented and dedicated scientists. We learned many things from each other as we built the experiments described in this thesis. It is a rare thing to work so constructively and amiably with coworkers, and I am grateful to them for their role in making these experiments successful and for making my last years in the

group good ones. A special thanks goes to our theory collaborator Dr. Zhexuan Gong for his illuminating discussions and his contributed code. I would also like to acknowledge the love and support that my wife, parents, sisters, and more recently, my daughter have shown me throughout my graduate career.

Table of Contents

List of Figures

Chapter 1: Introduction

A century ago when George Mallory was asked why he climbed Mount Everest, he tersely replied, "Because it's there" [2]. Sometimes people are driven to accomplish great things because there are compelling rational motivations. Sometimes they pursue lofty goals simply because they can, with the hope that they will learn things along the way that justify their endeavors. Nowhere is this facet of the human spirit more exemplified than in quantum information science. It is an exciting nexus between the tangible march of technological progress and the esoteric mysteries of our reality's fundamental nature. The development of quantum mechanics revealed a remarkably different and in some ways unsettling description of some basic concepts of nature. At the core of the theory is the idea of *superposition*. In common experience at our macroscopic scale of existence, things can only be in one mutually exclusive state at a time. A ball can be both round and red, but it cannot be both round and cubic, just as it cannot be simultaneously *here* and *there*. A quantum system, however, *can* be in multiple states simultaneously, with a very precise probability associated with each of those possibilities. On first conception this seems trivial, because a coin flipping in the air has a 50% chance of landing on either side. This coin is not in a superposition, though, and the distinction is any-

thing but trivial. Although *we* might not practically know which side the coin will land on, the *coin* knows which side it will land on; in other words, given the measurable quantities about the coin like its moment of inertia, rotation rate, velocity, and so on, the way the coin will land is already determined by nature in accordance with the laws of classical mechanics. When a quantum system is in a superposition state, *nothing* can know which of the possibilities will manifest, including the system itself, until an interaction (like a measurement) forces it to choose. This is the genesis of Schrödinger's absurd thought experiment about the cat in a superposition of being both alive and dead [3, 4]. Aside from the bizarre nature of the idea of superposition *per se*, the absurdity of Schrödinger's famous feline derives from the fact that superpositions on the magnitude of a cat have never been observed and are astronomically unlikely, but not theoretically impossible. Understanding why this is true leads directly to the quest of engineering such an unnatural system, a task overwhelmingly more challenging than scaling the Earth's tallest mountain yet in many ways driven by the same attitude.

Modern atomic physics research is an expensive game, and there are precious few resources allocated for so-called "pure" research, no matter how noble the pursuit may be. Fortunately for the "because it's there" crowd, new insights into nature often lead to new inventions when clever people are involved. The technological proposals of some very clever scientists over the years effectively launched the field of quantum information science. These technologies promise revolutionary and powerful capabilities for computation and communication, providing the motivation for governments and industry to fund the research toward their realization.

In 1981, Richard Feynman proposed that the best way to explore interesting quantum systems in order to understand them might be to model and simulate them with separate, controllable quantum systems [5]. After all, we have great success using classical systems to simulate other classical systems, whether we mean constructing a physical model of an airplane and placing it in a wind tunnel or instead writing sophisticated software to simulate the mechanics of the airplane according to known material properties and theoretical models. Why would Feynman suggest engineering complicated quantum systems to model other quantum systems instead of utilizing and improving the far more advanced technology of classical computers? To answer this question, we need to elaborate on the concept of superposition and introduce a critical consequence of the idea: entanglement.

Consider the classical binary digit (bit) of modern computers. These are the basic elements of information in the machine, which can be in one of two possible states that we will call 0 and 1. The analogous quantum bit (qubit) is a quantum system that can be in a superposition of the two states $|0\rangle$ and $|1\rangle$, so two numbers are required to specify its state. For two qubits, four numbers are required, because the state is some superposition of $|00\rangle$, $|01\rangle$, $|10\rangle$ and $|11\rangle$. For three qubits, eight numbers are needed. The number of values needed to specify the state of N qubits therefore scales exponentially as 2^N. This is bad news for a classical computer based on classical bits, because even a simple quantum system of 30 qubits would require over a billion numbers, or $\sim$10 MiB, just to specify the state! A moderate increase to 100 qubits requires a ludicrous $\sim$1000 YiB (yobibytes), which is already more storage than is available in all the hard disks in the world. If you only triple the

number of qubits to 300, you need more numbers to specify the state than there are estimated particles in the universe. This is why Feynman's proposal is really a necessity for the research of increasingly complex many-body quantum systems that involve strongly correlated particles.

The potential power of this exponential increase in the state space of quantum systems became even more exciting when in 1985 David Deutsch introduced a way to use entanglement in such systems to allow parallel processing of all 2^N superposition states to compute a function exponentially faster than a classical computer [6]. By 1994, Peter Shor had developed an algorithm based on this idea that could factor numbers faster than the fastest known classical algorithm [7]. This got the attention of security experts worldwide, because the asymmetric difficulty of factoring large numbers versus multiplying large numbers is the foundation of modern encryption techniques. Industry standard encryption protocols like RSA rely on the fact that it is easy to multiply two very large secret numbers together, but the resources it takes to determine what those secret factors are based solely on their product scale exponentially with the size of the factors. Given that there is already a vast amount of data encrypted in this way, anyone that possesses a quantum computer capable of running Shor's algorithm alone would have immense power. Other notable algorithms are the Deutsch-Jozsa algorithm [8] and Grover's search algorithm [9], both of which have been demonstrated with trapped ions [10, 11]. Another important theoretical contribution came from Shor [12] and Steane [13] concerning error correction. Due to the nature of wave function collapse, some worried that anything other than passive stabilization techniques would destroy the delicate states required

of a quantum computer and therefore be infeasible. This challenge can be overcome by using sufficient numbers of extra qubits and error-correcting codes that tolerate specified amounts of inaccuracy and decoherence in the quantum gate operations.

Entanglement is a special and profound type of superposition in which multiple states are correlated in a way that is simply not possible classically. An entangled state involving quantifiable aspects of what we consider "one thing" does not seem exceptionally interesting. For instance, if a quantum ball is in an equal superposition of being red *here* and blue *there*, then it means that half the time we will find it *here* and it will be red and *vice versa*. Although the state of being in two places at the same time is not exactly easy to accept, the situation gets much more confusing when the entangled states are those of entities we typically consider "separate things". In the experiments described in this thesis, for example, the two states are the electronic configurations of two separate ytterbium atoms. Each atom can exist in a superposition of two possible configurations, $|0\rangle$ and $|1\rangle$ (making them qubits). We apply interactions that transform the state of the two atoms from $|00\rangle$ to $|00\rangle + |11\rangle$. A consequence of being in this entangled state is that, regardless of how far apart in spacetime these atoms are separated, their measured states will always be perfectly correlated as either both 0 or both 1. Einstein called this seeming paradox "spooky action at a distance" because it appeared that somehow the qubits would have to coordinate by superluminal communication. Some wanted to believe that the members of an entangled state contained some kind of shared hidden information local to each that would predetermine which state they would choose upon measurement. This rather conspiratorial but understandable idea was laid to

rest by John Bell and other experimentalists that followed him, who pulled what was thought to be metaphysics firmly into the clutches of science with a theorem claiming that no local hidden variable theory is compatible with quantum mechanics [14–17]. Although the philosophical consequences of this fact are as intriguing as they are difficult to grasp, for the purposes of the work presented here, entanglement can be considered a tool to be harnessed for the practical development of a quantum information processor.

David DiVincenzo wrote a concise set of necessary criteria for any quantum system striving to be a platform for quantum computing [18]. In abbreviated form, they are

- A *scalable* physical system with well characterized qubits
- The ability to initialize the qubits to a particular simple state like $|0000\ldots\rangle$
- Coherence times much longer than the time scale of the quantum operations
- A "universal set" of quantum gates
- Individual qubit rotation and measurement

A diverse and vibrant field of quantum information systems have blossomed since these requirements were articulated. There are cold atomic systems like trapped ions and neutral atoms in optical lattices, photonic systems, and a wide range of solid state systems including superconductors, quantum dots, and nitrogen-vacancy centers in diamond [19]. While typically discussed as "competing systems",

given the relatively primitive state of the art, the physics learned and the technology developed by exploring each of these disparate systems inevitably benefits the others. Still, the platforms are by no means equal in proven capability and feasible scalability. In the context of DiVencenzo's criteria and comparative metrics, trapped ions are currently the most advanced quantum information processing (QIP) platform, with the $^{171}Yb^{+}$ ion specifically boasting several advantages. Individual qubits can be arbitrarily rotated with exquisite precision, and they can be initialized and detected with very high fidelity [20]. The extreme isolation of the qubits in ultra-high vacuum environments and the insensitivity of the states to field noise grants them extremely long coherence times ($\sim$1 sec) many orders of magnitude longer than the typical gate times ($\sim$10-100 µs).

The thrust of the work presented in this thesis addresses the issue of scalability with respect to the universal set of quantum gates [21] on linear ion crystals. Since arbitrary single qubit gates as well as arbitrary two-qubit entangling gates can be performed on qubits in a chain of trapped ions, it should be possible to execute an arbitrary quantum algorithm with the system, limited only by the number of qubits available. Thus, trapped ion chain QIP has demonstrated virtually all of DiVencenzo's criteria. Now the task is to ensure the system is *scalable* to large numbers of qubits. A promising architecture for truly scalable QIP involves coupling relatively small local qubit registers with photonic interconnects [22] to form a distributed quantum network. This network would be capable of constructing arbitrarily large entangled states across potentially long distances using quantum repeaters based on heralded entanglement. In this grand vision, quantum gates are performed locally

on the qubit registers that will range in size from 10-100 qubits. Some of the key challenges of scaling our system this way are the individual addressing of arbitrary subsets of ions and controlling the growing complexity of motional mode interactions as the number of qubits increases. Traditional entangling quantum gates between ion qubits use laser pulses to couple the qubit states to the collective motion of the crystal, thereby generating a spin-spin interaction that can produce entanglement between selected qubits. The inherent limitations on the performance of gates using this method can be alleviated by applying optimally shaped pulses instead of pulses with constant amplitude. The experiments described in this thesis are the first demonstration of this pulse shaping technique, and they represent a significant advancement toward a scalable trapped ion quantum information processor.

The structure of the text consists of sections that generally build on concepts and information from previous sections, with a didactic tendency aimed at benefiting new members of the research group. Its goal is to both complement and supplement the other excellent theses from previous graduates of the group. Chapter 2 details the experimental apparatus of the experiments, including the ion trap, the optical systems and the relevant Yb atom properties. Chapter 3 explains how we perform single and multi-qubit gates by deriving the relevant interactions as clearly as possible. Chapter 4 introduces the theory of the pulse shaping scheme and our experimental demonstrations of it on qubits in chains of various length. Chapter 5 describes the extension of the technique to improving the fidelity of gate sequences, where we demonstrate tripartite entanglement using shuttling and individual qubit addressing. Chapter 6 describes some interesting possibilities for the next iteration

of the experiment, which promises to significantly improve the system's capabilities.

Chapter 2: Experimental system

The system required to perform these experiments involves many components covering a wide range of hardware and software. This chapter describes these components and what role they play in performing the experimental sequences and acquiring the data. The structure of this description will be driven by the physical requirements of the experiment itself, which should provide an intuitive and logical way to connect the tangible realities of the laboratory with the more complete description of the physics in subsequent chapters.

2.1 $^{171}Yb^{+}$ qubit

From the requirements for quantum computation listed in the introduction, it is clear that the fundamental element in the system is the qubit. The choice of which physical system will be used to manifest the qubit is a complex one, with many competing systems. Our qubit is represented by two hyperfine levels in the ground state of an atomic $^{171}Yb^{+}$ ion. The qubit states $|0\rangle$ and $|1\rangle$ are defined as the atomic levels $^{2}S_{1/2}|F=0, m_F=0\rangle$ and $^{2}S_{1/2}|F=1, m_F=0\rangle$ as illustrated in Figure 2.1. There are several reasons for choosing these states. One basic feature is that the spontaneous decay rate from these levels is virtually zero since the $|0\rangle$

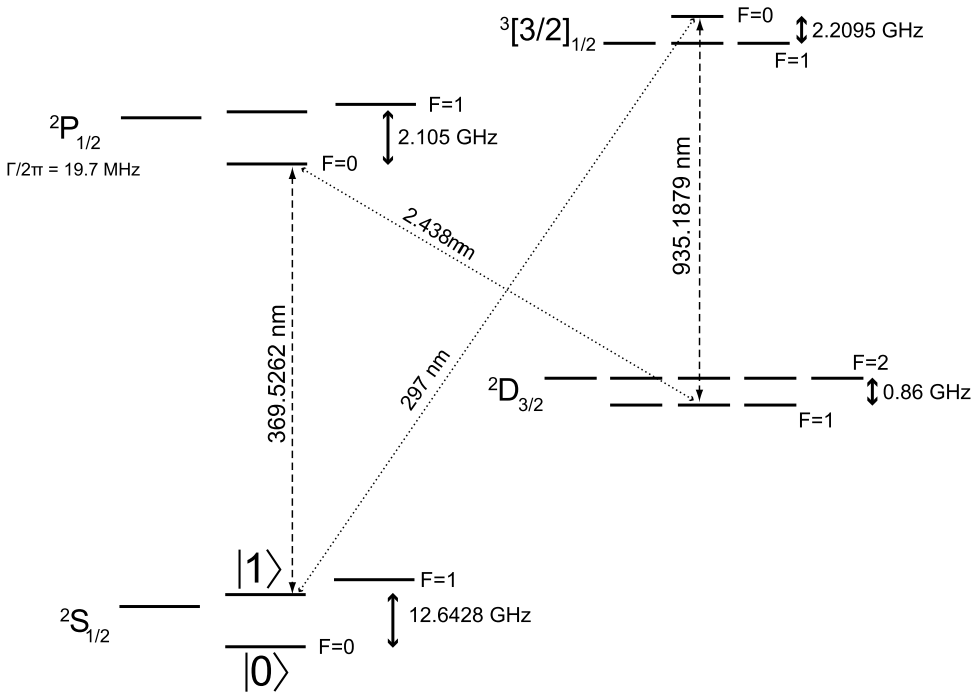

Figure 2.1: $^{171}Yb^+$ energy levels

state is the ground state and the only decay channel is magnetic dipole radiation from the $|1\rangle$ state. In addition to long qubit state lifetimes, in order to be a useful quantum memory a qubit must also maintain the relative coherent phase between these populations. Because the qubit states are separated by a finite energy difference ΔE, this phase accrues relative to the lab frame at a rate equal to the inverse of the energy gap:

$$|\psi\rangle = A|0\rangle + Be^{i(\phi_0+\Delta Et/\hbar)}|1\rangle \tag{2.1}$$

where A and B are real numbers and ϕ_0 is the initial qubit phase. In our case the frequency splitting $\nu_{qubit} = \Delta E/h = 12.642821$ GHz. Stable microwave synthesizers * that maintain phase coherence over time scales long compared to the coherent

*Agilent HP 8672

quantum operations are thus a necessity, and since multiple synthesizers are involved in the experiment they must be synchronized by a single, pristine frequency standard *. In general, qubit states defined by atomic levels suffer from dephasing due to fluctuations in their splitting, often driven by uncontrolled magnetic fields. The $m_F = 0$ levels are the least sensitive to these fluctuations, where the change in magnetic field induces only a second-order shift $\nu_{qubit} + \delta$, where $\delta = (310.8)B^2$ is in Hz and B is the magnetic field in gauss [23]. The consequently long qubit coherence time of these $^{171}Yb^+$ levels is largely why they are a competitive atomic clock system and hence are typically referred to as "clock" states [23, 24].

To be useful, the $^{171}Yb^+$ qubits must be tightly confined at one position, and they must be extremely well isolated from their surroundings. This harsh imprisonment is accomplished using an ultra-high vacuum (UHV) system and an rf "Paul" trap [25, 26].

2.2 Vacuum system

Achieving the necessary UHV level is not a trivial endeavor. At 10^{-11} torr, this is roughly equivalent to the pressure on the dark side of the moon [27]. Before describing the methods used to reach such low pressures, the vacuum requirement needs some justification. Under normal atmospheric conditions, the collision rate between free neutral particles in the air and trapped ions is simply too high. The task is to calculate how low the pressure needs to be in order to push the collision rate below an acceptable level. We can determine an order of magnitude estimate by

*Stanford Research Systems FS725 Rubidium Frequency Standard

assuming that the ion and a neutral particle form a two-body system that undergo a Langevin collision [28]. With the ion fixed at the origin, the Lagrangian of this simple system is given in radial coordinates by

$$L = \frac{1}{2}\mu\left(\dot{r}^2 + r^2\dot{\theta}^2\right) - U(r) \tag{2.2}$$

where $\mu \equiv \frac{m_1 m_2}{m_1+m_2}$ is the reduced mass and the interaction energy $U(r) = -\frac{\mathcal{P}Q^2}{8\pi\epsilon_0 r^4}$, where Q is the electric charge and $\mathcal{P}$ is the neutral particle polarizability. Since L is cyclic in θ, $\frac{d}{dt}\left(\frac{dL}{d\dot{\theta}}\right) = \frac{d}{dt}\left(\mu r^2\dot{\theta}^2\right) = 0$ means that $l \equiv \mu r^2\dot{\theta}^2$ is the constant angular momentum. The other Lagrange equation,

$$\frac{dL}{dr} - \frac{d}{dt}\left(\frac{dL}{d\dot{r}}\right) = 0 \tag{2.3}$$

yields the equation of motion

$$-\frac{dU}{dr} + \mu r\dot{\theta}^2 + \mu\ddot{r} = 0 \tag{2.4}$$

Substituting l into the middle term and integrating over r transforms the equation to

$$\mu\ddot{r} = -\frac{d}{dr}\left(U(r) + \frac{l^2}{2\mu r^2}\right) \equiv -\frac{d}{dr}U_{eff} \tag{2.5}$$

This effective radial potential U_{eff} provides a criterion for collision; namely, the maximum of the curve defines an impact parameter b that we can use to determine a collisional cross section $\sigma \equiv \pi b^2$. Setting the derivative of U_{eff} to zero and

solving for b yields the relationship $b^4 = \frac{4}{\mu v^2}\left(\frac{\mathcal{P}Q^2}{8\pi\epsilon_0}\right)$, where we take $l = mvb$ to be the magnitude of the angular momentum of the incident neutral at speed v. The collision rate can be estimated by multiplying the Langevin collision constant $k \equiv \sigma v = \pi b^2 v$ by the particle density $n = \frac{P}{k_B T}$:

$$\gamma = nk = \frac{PQ}{k_B T}\sqrt{\frac{\mathcal{P}\pi}{2\mu\epsilon_0}} \tag{2.6}$$

Using the predominant background gas H_2, where mass $m_{H_2} \sim 10^{-27}$ kg and polarizability $\mathcal{P}_{H_2} \sim 10^{-32}$ m^3, the collision rate is on the order of once per hour if the pressure is $\sim 10^{-11}$ torr.

The vacuum system design is driven by the need to reach UHV and to provide the necessary optical access for the experiment. Figure 2.2 depicts the components. The stainless steel vacuum hardware is connected by ConFlat flanges using OFHC copper gaskets. These components are typically cleaned with acetone then methanol and baked separately before chamber assembly. The bakeable valve connects the external pumps used in the initial stages of pumping and during the chamber bake. This process involves several steps. The entire assembled chamber is placed in an oven with the viewports covered tightly in metal foil to facilitate thermal equilibration in order to avoid cracking them. A high capacity ion pump and a turbo pump are connected to the bakeable valve by a long bellows that passes through the oven wall. The external turbo pump brings the pressure down to $\sim 10^{-7}$ torr at room temperature. At this point, the titanium sublimation pump, the ion gauge, and the atomic ovens are degassed. Degassing involves passing current through the

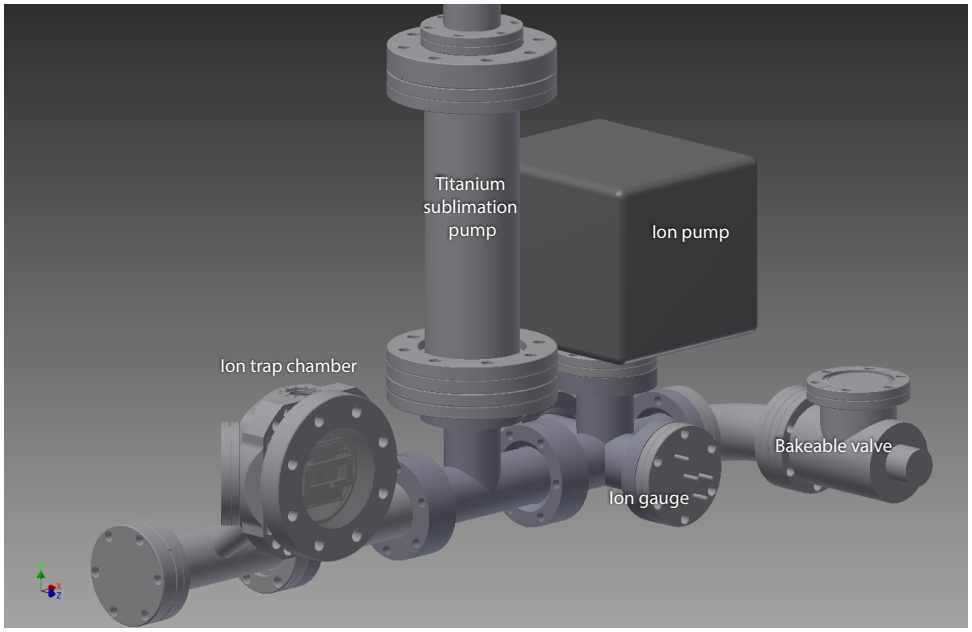

Figure 2.2: Drawing of the vacuum chamber.
The Ti:sublimation pump and bakeable valve are used during the initial pumping process. The ion pump and ion gauge operate continuously to maintain and monitor UHV.

elements to heat them enough to eject adsorbed material. The baking process is performed next to vaporize the water in the system and enhance the evacuation of contained gases. The temperature is increased slowly ($\sim$0.2°C/min, to maintain thermal equilibrium throughout the chamber) up to $\sim$160°C. Care must be taken to check the maximum temperature rating for all system materials. For example, UHV-compatible adhesives, feedthrough materials, capacitors and other circuit elements often have relatively low temperature limits. The chamber is maintained at high temperature usually for a few weeks, during which time the turbo pump can be valved off and the large external ion pump engaged. The internal ion pump is also engaged during this phase. When the chamber has maintained a steady drop in pressure and has reached $\sim 10^{-9}$ torr, the bakeable valve is closed (hand-tight) and

the temperature is slowly decreased back to room temperature. A torque wrench is used to ensure a proper seal of the bakeable valve. The titanium sublimation pump can then be used to plaster residual gases to the walls to push below the $\sim 10^{-10}$ torr range. Our chamber also includes small non-evaporable getter (NEG) pumping material positioned near the ion trap. The NEG materials we use are in the form of small pellets as well as malleable strips that passively pump mostly by adsorption. These pieces are activated during the bake, meaning that the high temperature drives an absorption of previously pumped material deeper into the bulk to make room for more particles on the surface, maximizing the pumping speed. The pumping rate is actually comparable to the effective pumping rate of the ion pump given the limited vacuum conductance between the main trapping zone and the ion pump.

2.3 Ion trap

2.3.1 Photoionization

Once a suitable vacuum environment is created, the next task is to produce $^{171}Yb^{+}$ qubits and localize them for use. We use a two-photon photoionization procedure to strip an electron from a neutral ^{171}Yb atom, allowing it to see the trapping potential and be captured. The description of this process will lead naturally to an introduction to the laser systems and the ion trap itself.

Tiny shards of ytterbium are packed into a ceramic tube, which is resistively heated by flowing current (1.4 A) through a tungsten coil wrapped around it. The

single open end of the tube is aimed to ensure high atomic flux through the trapping zone. In this region two UV beams intersect. The first is a resonant beam at 399nm to excite population of the neutral atoms on the ${}^1S_0 \leftrightarrow {}^1P_1$ transition. Population in the ${}^1P_1$ state can be excited to the continuum by photons of wavelength shorter than 394 nm. Since we already have 369 nm light available for Doppler cooling, optical pumping and state preparation (see Section 2.4), we use this color to complete the ionization process.

2.3.2 Ion trap concepts

The newly ionized atom, or ion, is now strongly influenced by electrical forces. It is not obvious how to trap a charged particle using electric fields alone. One might imagine constructing a "box" of opposing fields by surrounding the ion with electrodes, all at positive voltages to push the ion toward the center. Unfortunately, this construction is incompatible with Maxwell's equation $\nabla \cdot \vec{E} = 0$, which says the divergence of the electric field must vanish at all points in space in the absence of charge. Essentially, any set of electric fields converging on a point in space will ultimately find a way to "squeeze out", taking the ion with them. This fact is called Earnshaw's theorem [29]. The trick is to use *dynamic* fields [26]. To see how this might work, imagine that we apply a sinusoidal voltage to two symmetrically positioned electrodes. At the point precisely between these electrodes, the fields cancel out and an ion feels no force. If the ion moves radially outward, it begins to feel an increasing instantaneous force as the field magnitude increases. During the

first half of the oscillation period, the ion might be pushed away from the center of the trap. It will travel a certain distance outward before the field switches sign and pushes it back *closer* to the center than it started. This restoring effect is a consequence of the field inhomogeneity and is what gives rise to the so-called ponderomotive force that creates the confining pseudopotential in our trap. An important consequence of this kind of motion is that it is characterized by fast oscillations on top of slower drifts. The rapid motion is termed "micromotion" while the slower motion is referred to as the secular motion. Using this simple picture it is also easy to conceptualize the stability parameters of such a trap. Clearly, if the frequency of the oscillating field is too low, the ion will be ejected from the trap before the field can turn around to push it back. If it is too high, the field will switch back and forth so quickly that the ion will not have a chance to react, rendering the field useless. The range of frequencies producing a stable trap therefore depends on a ratio involving the force (ion charge and applied voltage), the resistance to that force (mass of the ion), and the level of field inhomogeneity (characteristic distance from the trap center to the electrodes).

2.3.3 Linear trap

While it is possible to confine an ion with only two electrodes as in the simple picture above, the resulting pseudopotential has a quadrupole character with only a single point in space where there is zero field. To hold a chain of ions, however, we need a linear region in space where all the ions can rest at points of zero field.

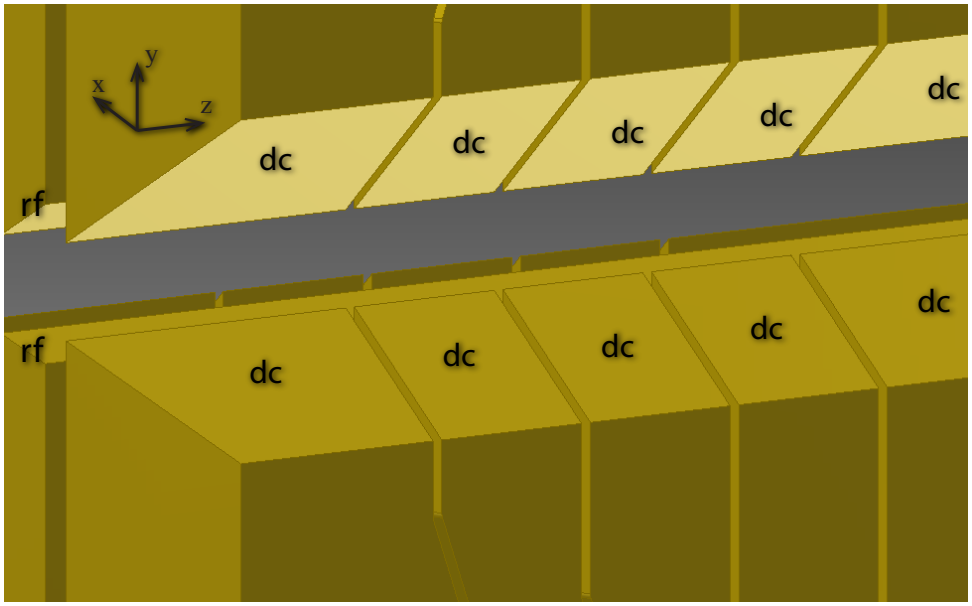

Figure 2.3: Drawing of the linear ion trap electrodes.

Traps of this geometry are appropriately called linear traps [30], and ours [31] is illustrated in Figure 2.3. The trap has a three layered geometry. The middle layer holds the radio frequency (rf) electrodes. By extending the rf electrodes along the axial direction as depicted, there are negligible axial components to the rf field lines near the center of the trap structure, and so the symmetry yields an "rf null line" along the axis. The transverse position of this rf null line is determined by the relative strength of the opposing rf voltages; thus, for equal voltages along the extent, the resulting null line is very linear and geometrically centered between the electrodes. The outer two layers of the trap are comprised of many independent electrodes that apply static (dc) voltages. The most important function of these dc electrodes is to provide the axial confinement of the ion chain by setting the voltages on the end electrodes higher than the voltages on the middle electrodes. Increasing this disparity strengthens the confinement and squeezes the ions together.

Recalling Earnshaw's theorem, the cost of increasing these voltages is a weakening of the transverse confinement resulting from the dc field lines "squeezing out" in that direction. The dc electrodes provide more than just axial confinement; they also allow trimming stray fields for micromotion minimization and rotating the principal axes of the trap. To understand these functions and how they are realized experimentally, a more detailed analysis of the trap potential is needed.

2.3.4 Trapping theory

An equation for a simple static quadrupole potential has the form

$$V(x, y, z) = \alpha x^2 + \beta y^2 + \gamma z^2 \tag{2.7}$$

For Laplace's equation to hold, $\nabla^2 V \equiv \left(\frac{\partial^2}{\partial X^2} + \frac{\partial^2}{\partial Y^2} + \frac{\partial^2}{\partial Z^2}\right) V = 0$, which means $\alpha + \beta + \gamma = 0$ and hence the curvature of at least one direction of the potential must be negative. The mechanical analogy often used to visualize how dynamic fields can solve the anti-trapping component of this potential is a spinning saddle. If you try to hold a marble on top of a saddle, it will simply roll off one of the downward slopes. However, if you spin the saddle, then the upward slopes will continually meet the marble to push it back toward the center before it has time to roll off. The marble will remain on the saddle if it spins at the proper speed. While not a perfect analogy, the imagery is tangible and instructive. Returning to our linear trap, Eqn. 2.7 loosely describes the static part of the trap potential if we take the z component to be the axial confinement, where the magnitude of α and

β are relatively small. Throughout this thesis, the z direction will be defined as the ion chain axial direction, y is the vertical direction connecting the two rf electrodes, and the x direction is perpendicular to the three electrode planes. The xz plane is thus horizontal and parallel to our optical table. To confine the ion in the transverse xy direction, we apply an inhomogeneous oscillating field as described above. For simplicity, assume this field is radially symmetric, which is approximately true, so that the problem becomes one-dimensional. The force an ion of mass m will feel is

$$m\ddot{r} = F_r(t) = eE(r)\cos\Omega t \tag{2.8}$$

where Ω is the applied rf frequency and $E(r)$ is the field magnitude at position r. If the field is homogeneous, then $E(r) = E$ is a constant and simple integration yields the equation of motion

$$r(t) - r_0 = -\frac{eE}{m\Omega^2}\cos\Omega t \tag{2.9}$$

assuming the ion was initially at rest at position r_0. As expected, there is no confining potential here, only simple driven motion at the rf drive frequency. Now introduce a small inhomogeneity to the field, where the first derivative must be included in the calculation using a Taylor expansion:

$$E(r) \approx E(r_0) + \frac{\partial E(r_0)}{\partial r}(r - r_0). \tag{2.10}$$

Here, the derivative is evaluated at the position r_0. Substituting Eqn. 2.9 into Eqn. 2.10 and considering only small deviations from r_0, the resulting form for $E(r)$,

$$E(r) = E(r_0) - \frac{\partial E(r_0)}{\partial r}\left(\frac{eE(r_0)}{m\Omega^2}\cos\Omega t\right), \tag{2.11}$$

can be used to evaluate the time-averaged force on the ion:

$$\begin{aligned}\langle F_r(t)\rangle_t &= \left\langle e\left(E(r_0) - \frac{\partial E(r_0)}{\partial r}\frac{eE(r_0)}{m\Omega^2}\cos\Omega t\right)\cos\Omega t\right\rangle_t \\ &= \frac{e^2}{2m\Omega^2}\frac{\partial E(r_0)}{\partial r}E(r_0) \\ &= -e\frac{\partial}{\partial r}\left(\frac{e}{4m\Omega^2}E^2(r_0)\right)\end{aligned} \tag{2.12}$$

The time-averaged force thus defines a pseudopotential

$$\Psi_{rf} \equiv \frac{e}{4m\Omega^2}E^2(r_0) \tag{2.13}$$

via $\langle F_r(t)\rangle_t = -e\nabla\Psi_{rf}$, where Ψ_{rf} is in volts. The more rigorous derivation of the equations of motion involves properly specifying the overall electric potential as a superposition of both dc and rf voltages and casting Eqn. 2.8 in the form of Mathieu's equations, which have well-studied solutions. From an experimental perspective, the most important results of the full analysis are the following:

- The motion of the ions can be approximately decoupled into three independent spatial modes, i, each with an associated harmonic frequency ω_i.

- There is a well-defined stability region parameterized by controlled quantities

as discussed conceptually earlier. These transverse direction stability parameters are given by q_r and a_r,

$$\begin{aligned} q_r &= -\frac{4e\kappa V_0}{m\Omega^2 d_r^2} \\ a_r &= -\frac{8e\kappa U_0}{m\Omega^2 d_r^2} \end{aligned} \tag{2.14}$$

where V_0 and U_0 are the rf and dc voltage amplitudes *on the rf electrodes* for a trap with characteristic ion–electrode distance d_r. The parameter κ is a voltage efficiency factor that characterizes the deviation from the ideal hyperbolic electrode geometry due to the particular electrode structure of the actual ion trap.

- The harmonic secular motion is perturbed by an intrinsic micromotion as evident in the lowest order approximation

$$r_i(t) = r_i^{(0)} \cos\omega_i t \left[1 - \frac{q_i}{2}\cos\Omega t\right] \tag{2.15}$$

where q_i is the stability parameter for the direction i. The presence of a stray static field E_i along direction i contributes an offset to the ion position as well as a driven motion called "excess micromotion" at the rf drive frequency that cannot be laser cooled. The ion position becomes

$$r_i(t) = r_i^{(0)} \cos\omega_i t \left[1 - \frac{q_i}{2}\cos\Omega t\right] + \frac{eE_i}{m\omega_i^2} + \frac{\sqrt{2}eE_i}{m\omega_i^2\Omega}\cos\Omega t \tag{2.16}$$

The suppression of these terms is discussed in Sec. 2.3.9.

2.3.5 Trap simulation

In practice, we design the trap parameters according to the experimental requirements by first modeling and numerically simulating the trapping potential using Charged Particle Optics (CPO), a software package which uses a boundary element method to solve Maxwell's equations in a volume of space. After accurately modeling the electrode geometry in a CAD application like AutoDesk Inventor, we convert the model files to the CPO electrode specification format using a conversion tool. The conversion process discretizes the geometry into triangular elements that CPO views as the "electrodes". Each of these triangles is specified with a number of subdivisions depending on how precise the simulation needs to be. The most straightforward approach is to convert each physical electrode as a separate CPO file, alter the relevant parameters like the "electrode label", and then manually combine the files into a single CPO file of the entire trap geometry. The next task is to apply 1 V to a single electrode with the rest at ground and run the simulation to calculate a grid of electric potential values as a function of position in space. This discrete matrix is finally interpolated to create a "basis function" for that electrode. Performing this process for each independent electrode accumulates a complete set of simulated basis functions. By the superposition principle for electric fields, an arbitrary static trap potential can be simulated by simply multiplying the applied voltage on each electrode by its basis function and summing over all electrodes. The complete trap-

ping potential, of course, includes the pseudopotential. The pseudopotential basis function is calculated in a similar fashion, but in this case both rf electrodes are set to 1 V and the simulated value is the square of the electric field magnitude. The pseudopotential is then directly calculated according to Eqn. 2.13 and added to the static potential to yield the complete trapping potential. Once the trapping potential simulation is complete, we can calculate all the relevant trap characteristics to ensure that the trap design is adequate.

2.3.6 Helical resonator

At this point we have to consider the available applied voltage ranges in order to determine the limits on the secular frequencies, rotation of principal axes, and trap depth. At room temperature, particles have on the order of 25 meV of energy, so trap depths on the order of 10 eV are desirable to ensure long trap lifetimes. These depths typically require rf voltages on the order of 200 V at frequencies around 30 MHz. Generating these high voltages at rf frequencies is not a trivial task. To accomplish this, we design and manually assemble a helical resonator to amplify the input rf voltage and deliver the filtered signal to the trap electrodes. The helical resonator is a compacted form of a traditional quarter-wave coaxial resonator, consisting of a grounded conducting tube surrounding an inner conducting coil that is grounded to the tube on one end. A conceptual sketch of the geometry is shown in Figure 2.3.6. Power from the amplified output of an rf frequency generator * is delivered via inductive coupling; that is, alternating current driven in a small loop

*FPGA controlled Direct Digital Synthesizer (DDS) output

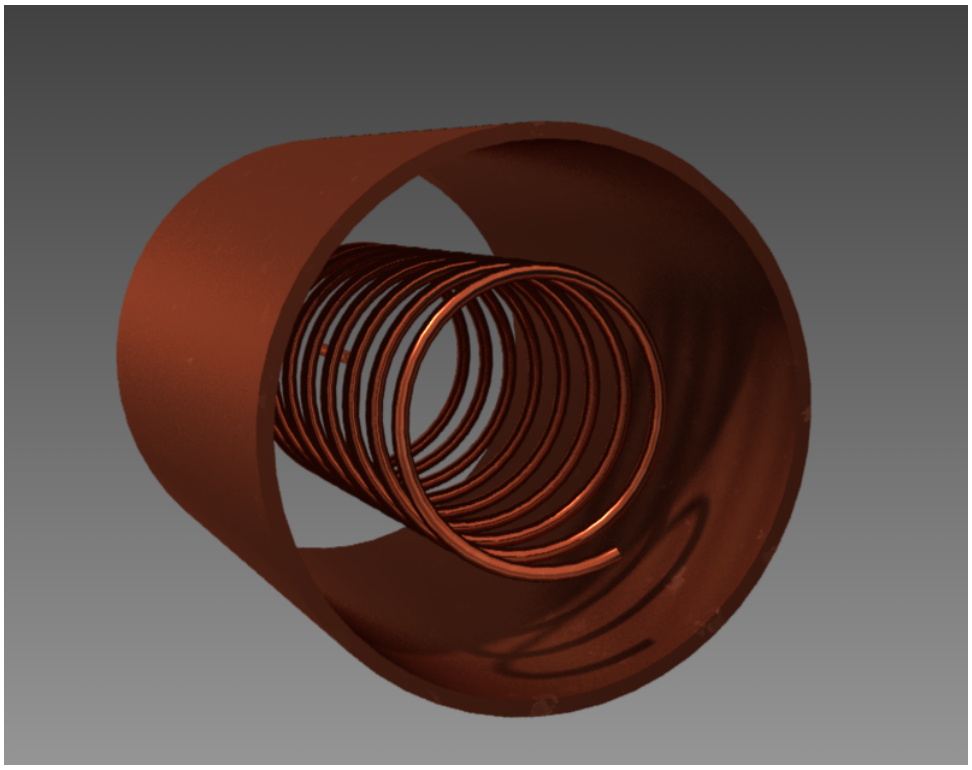

Figure 2.4: Sketch of the helical resonator geometry.
The endcaps and rf coupling coil are not shown.

generates a magnetic field that in turn drives alternating current in the resonator coil. The geometry of the resonator is carefully designed [32, 33] such that the electromagnetic energy in the resonator builds up at the resonant frequency, ν_0, causing an amplification of the voltage on the end of the coil connected to the trap rf electrodes. The resonator is characterized by a quality factor Q that quantifies how well it filters out unwanted frequencies and how efficiently it amplifies the input voltage. This quality factor $Q = \nu_0/\Delta\nu$, where $\Delta\nu$ is the frequency range between the -3 dB cutoff frequencies. Hence, the resonator also serves as an excellent bandpass filter. The Q value used in practice refers to the quality factor of the "loaded", critically coupled resonator. Because in practice we do not measure the Q using a ring-down method, but instead measure the reflected rf power as a function of input frequency, the resonator is always loaded by the source. The unloaded Q is twice the value of the measured Q, assuming the resonator is critically coupled. The amplification is related to the input power P by

$$V_{rf} = \xi\sqrt{PQZ_0} \tag{2.17}$$

where ξ is a factor (usually of order unity) specific to the individual resonator and $Z_0 = \sqrt{\frac{\mu_0}{\epsilon_0}} \approx 377$ ohms is the impedance of free space. Part of ξ comes solely from the geometry of the can. For example, in the case of the ideal, analytically solvable straight coaxial quarter wave resonator, ξ is equal to $\frac{2}{\pi}\sqrt{\ln(b/a)}$, where b/a is the ratio of the outer to inner conductor radii [34]. Normal b/a ratios lie between 10 and 40, corresponding to $1.0 < \xi < 1.2$. Actual values of ξ are slightly different due to

the coiled nature of the helical geometry in addition to the fact that the impedance is modified by the true permittivity ϵ and permeability μ that characterize the resistance of the medium to electric and magnetic fields. Realistic imperfections and additions to the resonator cavity, such as oxidation on the copper or Teflon mounting pieces used to mechanically stabilize the conducting coil, introduce a "loss tangent". The loss tangent is a way to characterize the amount of electromagnetic energy lost to dissipation in the medium. This loss is quantified by the imaginary part of the permittivity/permeability, such that the ratio of the imaginary to real components is geometrically a tangent in the complex plane. For a typical Q of around 200, we require close to 1 W of rf power to apply 300 V to the trap electrodes.

The relationship between the input rf power and the secular frequencies, hereafter simply called the "trap frequencies", can be determined experimentally with the help of the numerical trap simulation. For a three-layer linear trap, the trap frequencies are related to voltages on the electrodes in a more complicated way than the hyperbolic idealization. Simplified yet useful expressions for the linear trap secular frequencies are given by [35]

$$\omega_z^2 = \frac{2eU_0\epsilon}{mz_0^2} \tag{2.18}$$

$$\omega_{x,y}^2 = \left(\frac{\kappa_0 eV_0}{\sqrt{2}m\Omega r_0^2}\right)^2 \pm \frac{\kappa_1 eU_{rf}}{mr_1^2} - \frac{eU_0\epsilon}{mz_0^2} \tag{2.19}$$

where U_{rf} is the dc voltage on the rf electrodes. This is the voltage that breaks the symmetry to allow for control of the principal axes, which are explained in the next section. In the four-rod linear trap on which these equations are based, $\kappa_0 = \kappa_1$ and

$r_0 = r_1$ because the middle dc control geometry is the rf electrode geometry. In our three-layer trap, this control is enabled by separate dc electrodes sandwiching the rf electrodes instead of from dc bias on the rf electrodes (Fig. 2.3). Consequently, the voltage efficiency factor κ_1 and distance r_1 are different. Regardless of the actual values of these dc terms, the quadrature sum of the trap frequencies provides an expression proportional only to the effective rf voltage $(\kappa_0 V_0)^2$:

$$\omega_x^2 + \omega_y^2 + \frac{1}{2}\omega_z^2 = \left(\frac{e\kappa_0 V_0}{\sqrt{2}m\Omega r_0^2}\right)^2. \tag{2.20}$$

Technically the precise distance r_0 is also unknown, but can be consumed by a related factor we will call $\kappa_r \equiv \kappa_0/r_0^2$. Measuring the trap frequencies as a function of known input rf power will therefore obey the equation

$$\omega_x^2 + \omega_y^2 + \frac{1}{2}\omega_z^2 = \left(\frac{e\kappa_r \xi\sqrt{PQZ_0}}{\sqrt{2}m\Omega}\right)^2 \tag{2.21}$$

The trap simulations in CPO can provide an estimate of $\kappa_r V_0$ by adjusting the "effective rf voltage" in the simulation until the measured frequencies are obtained. If we define $V_{CPO} \equiv \kappa_r V_0$ and combine the CPO value with that obtained from Eq. 2.21, we get

$$k_r \xi = \frac{V_{CPO}}{\sqrt{PQZ_0}} \tag{2.22}$$

Once measured, these parameters allow the estimation of what rf power should be needed to achieve desired trap frequencies.

2.3.7 Principal axes

The range of the expected trap frequencies ω_i is calculated by fitting the simulated potential near the rf null to a parabola and taking the quadratic coefficient. The particular directions along which to make these fits are decided by the principal axes of the trap. Essentially, these are the perpendicular directions along which the potential has maximal and minimal curvatures. One of the three principal axes is obvious; it is along the axial direction. The remaining two principal axes in the transverse plane are not so obvious, but they can be ascertained using the Hessian matrix [36],

$$H(\phi(x_0, y_0)) = \begin{pmatrix} \frac{\partial^2\phi(x_0,y_0)}{\partial x^2} & \frac{\partial^2\phi(x_0,y_0)}{\partial x \partial y} \\ \frac{\partial^2\phi(x_0,y_0)}{\partial y \partial x} & \frac{\partial^2\phi(x_0,y_0)}{\partial y^2} \end{pmatrix} \tag{2.23}$$

where $\phi(x, y)$ is the total transverse trapping potential. The eigenvalues of the Hessian matrix determine the directions of greatest and least curvature about the point (x_0, y_0), which is taken to be the trap center when finding the principal axes. Figure 2.3.7 shows a simulation of the transverse trapping potential with the calculated principal axes. Two sets of principal axes are displayed, corresponding to points separated by about 100 µm along the ion chain axis. This shows that in a realistic geometry, there can be a "twisting" of the principal axes along the crystal that could be a problem for very long chains. The orientation of principal axes is critical for cooling the ion, as we will discuss shortly, as well as for alignment of beams that coherently manipulate the qubits (see Section 2.5.3). Precise control of the principal axes orientation is a necessity.

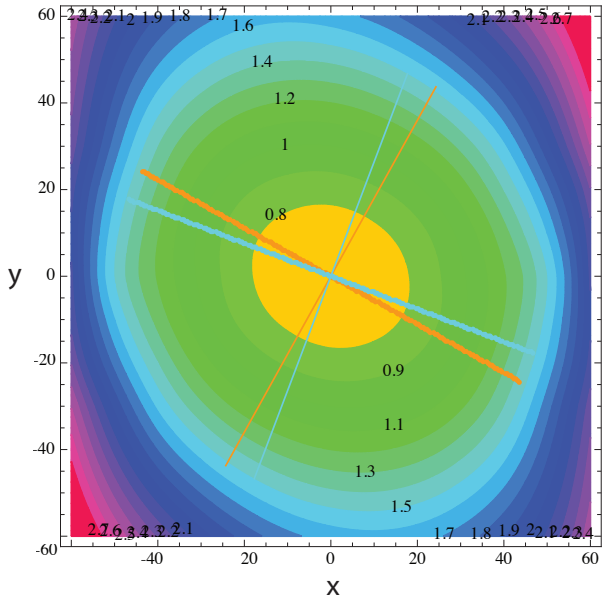

Figure 2.5: CPO simulation of transverse potential with principal axes. Contour plot of trap depth as a function of transverse position. The two sets of calculated principal axes correspond to points separated by about 100 µm along the ion chain axis. In practice, the axes are aligned to the x and y axes.

This brings us back to the functions of the dc electrodes. Apart from generating axial confinement for the trap, the dc electrodes are also used to rotate the principal axes of the trap. Simulations provide a good estimate for how far they can be rotated given the available static voltage range. The details of our dc voltage source are elaborated in Section 5.1 about our shuttling procedure. Due to the three layered geometry of our trap, we are able to deterministically rotate the principal axes in the transverse plane using the outer layer electrodes alone [34]. For other trap geometries, it might be necessary to independently bias the rf electrodes with separate dc voltages in order to enable this control. A prominent example is the "blade" trap design with only four blades [37, 38]. In order to apply independent bias voltages to the rf electrodes, the helical resonator can must contain two coils

in a "bifilar" arrangement, both of which terminate not on the grounded resonator can itself but instead on SMA bulkheads for the dc voltage inputs.

2.3.8 Coupled dc control

It is apparent that there are multiple independent trap parameters that need to be simultaneously controlled by the same set of dc electrodes. The efficient way to accomplish this is by constructing a transformation matrix T that couples the electrodes together in a practical way [39]:

$$\begin{pmatrix} e1 \\ e2 \\ e3 \\ e4 \\ \vdots \end{pmatrix} = T \cdot \begin{pmatrix} \text{endcap average} \\ \text{central average} \\ \text{axes rotation} \\ \text{axial displacement} \\ \vdots \end{pmatrix} \tag{2.24}$$

The natural way to construct this matrix is to build its inverse using linearly independent combinations of electrode voltages. Figure 2.6 labels the front plane of dc electrodes in blue and the back plane in red parentheses. In the following description, electrodes will be denoted by "eN", where N is the labeled electrode number. Four of the electrodes are electrically grounded and marked "G". To control the strength of the axial confinement, we need to control the average of the voltages on the endcaps ($e1 + e2 + e3 + e4$) and the average of the voltages on the central electrodes ($e5 + e6 + e7 + e8$). To control the principal axes rotation, we couple the

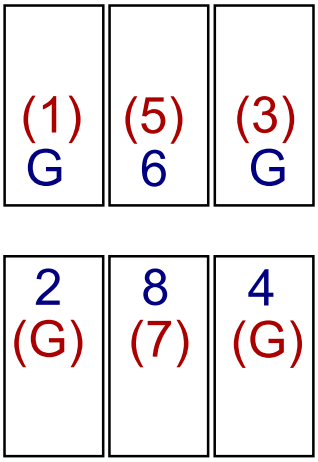

Figure 2.6: Coupled DC voltage control.
Front plane (blue) and back plane (red, in parentheses) dc electrode labels.

central electrodes in a different way ($e5 - e6 - e7 + e8$). To push the ions along the axial direction, the difference in the endcap averages suffices ($e1 + e2 - e3 - e4$). So far the inverse transformation matrix, T^{-1}, is

$$T^{-1} = \begin{pmatrix} 1 & 1 & 1 & 1 & 0 & 0 & 0 & 0 \\ 0 & 0 & 0 & 0 & 1 & 1 & 1 & 1 \\ 0 & 0 & 0 & 0 & 1 & -1 & -1 & 1 \\ 1 & 1 & -1 & -1 & 0 & 0 & 0 & 0 \\ \vdots & \vdots & \vdots & \vdots & \vdots & \vdots & \vdots & \vdots \end{pmatrix} \tag{2.25}$$

The rest of the matrix is completed in a similar way, providing the necessary controls to apply static offsets in all three directions to cancel stray fields, configure the principal axes orientation, and set the axial trap frequency. In practice, the logical controls are adjusted via a National Instruments LabView interface, while the transformation matrix is applied in real-time by the software to adjust the applied

dc voltages (Sec. 5.1).

There is another important characteristic of our trap potential that deserves explanation, and that is the criterion for linearity. The anisotropy $\mathcal{A}$ of our trap potential is given by the ratio between the transverse and axial frequencies, $\mathcal{A} \equiv (\omega_r/\omega_z)^2$. There is a relationship between this anisotropy and the maximum number of ions, N, that can be trapped in a linear configuration before they buckle into a zig-zag arrangement; it is given by $\sqrt{\mathcal{A}} > 0.77N/\sqrt{\log N}$, which is a good approximation for $N > 5$ [13,40,41]. For a five ion chain, the criterion stipulates that $\mathcal{A} > 9$, which we clearly satisfy with an $\mathcal{A} \approx 60$. This imposes yet another constraint to consider when we design our ion spacing and transverse motional mode splittings. These issues will be discussed further in Section 3.2.1.

2.3.9 Micromotion compensation

Micromotion compensation is the procedure that detects excess micromotion and minimizes it by compensating for a stray static field that is pushing the ions away from the rf null. This static offset is the remaining function of the dc voltage control, as there will always be an unintended finite stray electric field present in an ion trap. In a well-designed trap, this stray field will remain relatively constant so that it can be negated for long periods of time without adjusting the voltage set. The reason it is so important to actually cancel this field, instead of just calibrating for the resultant shift in the ion chain position, is that any position in space off the rf null subjects the ion to "excess" micromotion. Recalling Eqn. 2.16, there is an

intrinsic micromotion that is unavoidable. It can be minimized by engineering q_r within the bounds of the stability region and the desired trap frequencies, but it will exist nonetheless. Fortunately, laser cooling reduces this intrinsic micromotion amplitude because it is proportional to the secular motion. In contrast, excess micromotion amplitude is proportional to the stray field amplitude and is driven by the trap rf. This motion cannot be cooled directly and in some situations this can be a significant source of motional mode heating [42].

In the reference frame of an ion subject to micromotion, the cooling beam frequency is modulated at the driving rf frequency Ω, which causes a modulation of the ion fluorescence according to Eqn. 2.28, where the shift $\mathbf{k} \cdot \mathbf{v}(t)$ is proportional to $\Omega \sin(\Omega t)$ (suppressing the phase term) [42]. For half of the rf period, the ion is moving toward the light and it is Doppler shifted blue; for the second half, the opposite is true. Hence, the ion brightness is correlated with the rf phase. By repeatedly measuring the time interval T between the beginning of an rf cycle and the detection of a scattered photon using a time-to-digital converter (TDC), we accumulate a histogram of counts as a function of T. Figure 2.7 shows an example of two such histograms, acquired for an ion positioned on either side of the rf null. The TDC start pulse is a phase-locked frequency reference TTL from the trap rf source, and the stop pulse comes directly from the photo-multiplier tube (PMT) when a photon is detected. The values of T that correspond to the turning points of the micromotion will have the median number of counts because the beam is not Doppler shifted and is thus detuned 10 MHz (that is, half width at half maximum of the absorption profile where Doppler cooling is optimal; see Sec. 2.4.1). Likewise,

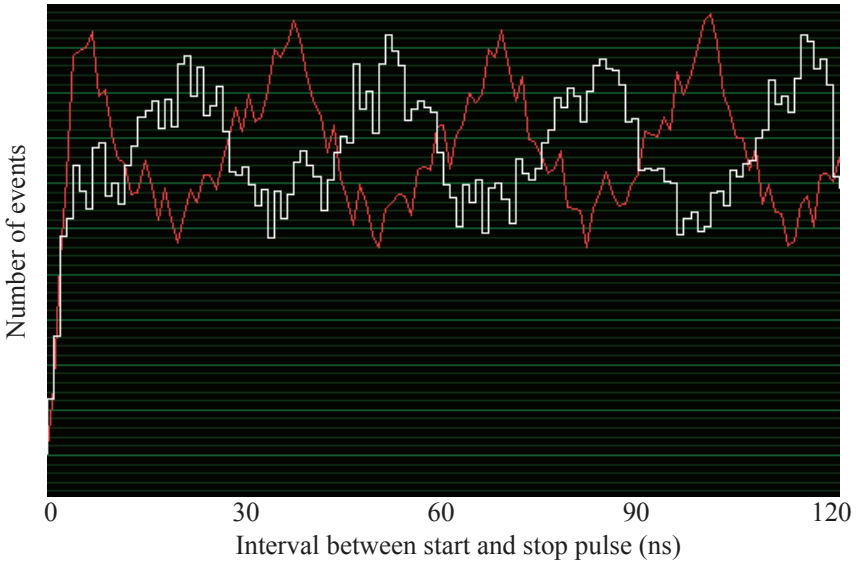

Figure 2.7: Micromotion compensation.
Two histograms of TDC data are plotted for an ion displaced from the rf null in opposite directions, yielding opposite phase relationships between the rf drive and the ion motion. The start pulse is retriggered every four rf periods, every $\sim 4 \times 30$ ns.

the T associated with the rf phase at which the ion is moving towards the beam will show the highest counts, and vice versa. In the limit of small micromotion, the magnitude of the sinusoidal profile of this histogram is directly proportional to the micromotion amplitude [42]. For convenience, we retrigger every four start pulses. This acquires a histogram whose sinusoidal profile oscillates several times, making the periodic signal easier to detect visually. The process of minimization involves pushing the ion along orthogonal directions using the coupled electrode voltage control illustrated by Eqn. 2.25 to find a position that minimizes the amplitude of the histogram profile.

Three linearly independent beams are generally necessary to detect micromotion in all three spatial directions. In practice, fewer beams can suffice based on the

rf field line geometry. In a linear trap like ours, there is negligible rf field amplitude in the axial direction because the field lines extend radially from the chain in the transverse direction, so only two beams in the xy plane are needed. Optical access through the trap restricts our cooling beam to instead lie almost parallel ($\sim 5^\circ$) to the xz plane at approximately 45° to the x axis, giving us sensitivity to micromotion along that axis but not along the vertical y direction. Our principal axes are rotated such that the transverse modes of motion are virtually parallel to the x and y directions. Since we couple negligibly to the vertical modes during the entangling gates, it is less critical to minimize micromotion along that dimension beyond the coarse adjustment. The coarse adjustment is the process of positioning the ion based on its image acquired by the intensified charge-coupled device (CCD) camera*. We lower the rf voltage (weakening the confinement), allowing any stray static field to push the ion further away from the rf null. We adjust the dc voltages to compensate until the ion position no longer changes as a function of confinement strength. This method is coarse because it is limited by the resolution of the imaging system, typically limiting precision to $\sim$500 nm. After coarse positioning, the optimal x position is discovered by moving the ion back and forth along that axis and measuring the rf phase correlation histogram with the TDC. At the optimal position, the histogram amplitude is minimal; additionally, the phase of the signal flips 180° because that is precisely what the rf phase does at the rf null. To achieve the highest sensitivity, the cooling beam is detuned 10 MHz with optical power below saturation to maximize the modulation of the fluorescence for a given micromotion amplitude.

*Princeton PI-MAX3

Although high resolution TDCs can be purchased commercially, they are generally far more sophisticated and expensive than is necessary for this measurement. Our rf drive frequency has a period of about 30 ns, necessitating a time interval resolution of no more than a few nanoseconds to achieve a decent sinusoidal fit. We constructed a TDC using an FPGA [43] over-clocked from its base clock frequency of 50 MHz to an effective 200 MHz. A resolution on the order of 1 ns is achieved by implementing dual counters. The coarse clock for the time intervals is implemented by simply counting clock cycles (5 ns increments). The fine time measurement requires the use of a "carry chain" to measure durations shorter than a clock cycle. Essentially, a register of bits is initialized to the value 1, and when 1 is added to this register at the beginning of a clock cycle, the bits flip to 0 sequentially as the arithmetic is performed. The stop pulse terminates this sequence prematurely, such that the number of bits flipped indicates the time elapsed. The unique details of the physical FPGA circuitry cause the carry chain to progress non-uniformly. Since this non-uniformity is constant, we can compensate for it in the software using a calibration empirically determined by applying uncorrelated start and stop pulses to the device. Deviations from zero in the resultant signal amplitude are suppressed by appropriate weighting factors for the associated time interval values.

2.4 Qubit initialization and state detection

So far we have examined the vacuum environment, the trap potential and the ion loading procedure. In all of the experiments, there is a sequence of optical pulses

that initialize the qubits before the coherent operations, and there is an optical pulse afterward to perform state detection.

2.4.1 Doppler cooling

The first step after loading the ions is to slow them down them using optical Doppler cooling. The atomic flux from the heated oven has a thermal distribution of velocities averaging hundreds of meters per second, corresponding to kinetic energies on the order of the trap depth. At these initial energies, the ions execute large orbits in the trap, where their collisions with one another make them susceptible to rf heating. For the quantum gates to work properly, we need the ions to start near their ground state of motion, where the quantized energy levels of the harmonic trap have an average occupation number $\bar{n} \sim 0$. At room temperature, $\bar{n} \sim 10^6$, where $\bar{n} \sim k_B T/\hbar\omega_i$. Doppler cooling allows us to cool the ions from these high phonon levels to $\bar{n} \sim 5$, a value that depends on the trap frequency and the linewidth of the optical transition. Conceptually, Doppler cooling works by preferentially imparting momentum to the ion *against* its direction of motion, hence slowing it down. By red detuning the incident Doppler cooling beam at wavelength λ_L from a resonant atomic transition, the ion absorbs more photons when moving toward the light than when it moves any other direction via the Doppler effect. Since the spontaneous emission process causes isotropic radiation of photons, the average recoil due to that process is zero, thereby reducing the ion momentum on average by h/λ_L per scattering event and dissipating the kinetic energy in the form of slightly higher

frequency light. An interesting feature of our trapping potentials is that a single beam is sufficient to cool the ions, as long as there is a component of the beam wave vector along each of the three principal axes corresponding to three non-degenerate trap frequencies [44].

The strong ${}^2S_{1/2} \leftrightarrow {}^2P_{1/2}$ transition at 369 nm in the ${}^{171}\mathrm{Yb}^+$ ion is the workhorse of our incoherent qubit operations. Specifically, we tune the 369 nm "carrier" beam to the ${}^2S_{1/2}|F=1\rangle \leftrightarrow {}^2P_{1/2}|F=0\rangle$ transition (Fig. 2.8). It is the primary transition we use for Doppler cooling as well as optical pumping and state detection as discussed below. Its linewidth, $\Gamma/2\pi = 20$ MHz, allows a Doppler cooling limit of $k_B T = \hbar\Gamma/2 \sim \bar{n}_i \hbar\omega_i$. For a trap frequency $\omega_r/2\pi \approx 3$ MHz, we expect to cool down to $\bar{n} \sim 4$. To cool further, we must use Raman sideband cooling [45]. Optimal cooling occurs at a detuning where the slope of the absorption line shape is maximal. This can be understood by considering the Doppler shift itself. The slower the ion goes, the less the cooling beam frequency is shifted in its reference frame. Since the cooling mechanism depends on the difference between scattering rates at the shifted and unshifted frequencies, maximizing the line shape slope will maximize this difference for a given velocity. This is consequently the reason that the Doppler cooling limit can only be reached when the light intensity on the ion is below saturation intensity, given by

$$I_{sat} = \frac{\pi h c \Gamma}{3\lambda^3 R_{br}} \tag{2.26}$$

where $R_{br} = 99.5\%$ is the branching ratio back to the ${}^2S_{1/2}$ state. The linewidth

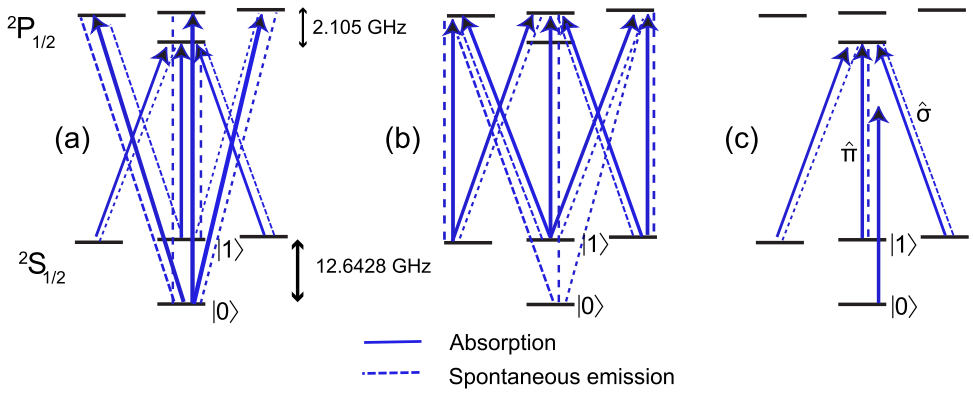

Figure 2.8: $^{171}Yb^+$ cooling, optical pumping, and detection transitions at 369 nm. (a) Cooling. (b) Optical pumping. (c) Detection.

of an optical transition is power broadened according to $\Gamma = \Gamma_0\sqrt{1 + I/I_{sat}}$, where Γ_0 is the natural linewidth and I is the applied intensity. Lower intensities will therefore produce linewidths approaching the natural linewidth, maximizing the cooling rate [46].

Since the branching ratio above is not unity, the excited $^2P_{1/2}$ state will decay to the $^2D_{3/2}$ state roughly once every 200 scattering events, where it will remain for the 53 ms lifetime of that energy level. To prevent this population trapping, we continuously apply a 935.2 nm repumper beam to the ions. This excites the population to the $^2[3/2]_{1/2}$ state [47], from which there is a 98.2% probability of decay to the ground state within that state's 38 ns lifetime. This method provides a highly efficient way to return population back to the Doppler cooling transition.

The hyperfine structure of the $^{171}Yb^+$ ion demands that both the 369 nm cooling beam and the 935 nm repumper have polarization components along both the $\hat{\pi}$ and $\hat{\sigma}$ directions defined by our quantization axis to avoid optically pumping to the $^2S_{1/2}|F = 1, m_F = \pm 1\rangle$ Zeeman levels (see Figures 2.1 and 2.8(a)). Additionally,

we must apply sidebands to both beams. We apply a 14.7 GHz sideband to the 369 nm beam using the second-order sideband from a 7 GHz resonant electro-optic modulator (EOM) * in order to excite population that decays to the $|0\rangle$ state via the ${}^2S_{1/2}|F=0\rangle \leftrightarrow {}^2P_{1/2}|F=1\rangle$ transition. The 3.1 GHz sidebands necessary for the repumper are directly generated by a fiber-EOM †. The quantization axis is determined by an applied magnetic field of 5.5 gauss in the vertical direction. We use three linearly independent magnetic coils to control the magnitude and direction of the magnetic field at the trap. Direction control is important not only for defining the polarization directions for Doppler cooling but also for the coherent Raman transitions described in Section 2.5.3. The magnitude of the field is a compromise between the need to destabilize coherent dark states quickly by increasing the Zeeman splitting [48] and the need to maximize the scattering rate by limiting the detuning from the ${}^2S_{1/2}|F=1, m_F=\pm 1\rangle$ Zeeman levels.

2.4.2 Qubit initialization

The Doppler cooling cycle of the experiments leaves the ion in a statistical mixture of ${}^2S_{1/2}$ ground states. To properly initialize the qubit to the pure $|0\rangle$ state, we use an optical pumping procedure using optical fields almost identical to the Doppler cooling beam (see Figure 2.8(b)). The only difference is that the applied sideband is 2.1 GHz from the carrier to drive population from the ${}^2S_{1/2}|F=1\rangle$ manifold to the ${}^2P_{1/2}|F=1\rangle$ manifold. The high branching ratios from this state

*New Focus 4851 resonant EOM
†EOSpace

to the target ${}^2S_{1/2}|F=0\rangle$ state ensure that only a handful of scattering events are required to transfer virtually 100% of the population to the $|0\rangle$ state. The efficiency of initializing the $^{171}Yb^+$ qubit is greatly enhanced by the fact that the optical pumping frequencies are over 12 GHz off-resonant with the nearest transition from the $|0\rangle$ state, because the ${}^2S_{1/2}|F=0\rangle \leftrightarrow {}^2P_{1/2}|F=0\rangle$ transition is forbidden by selection rules. We optically pump ∼99% of the population to $|0\rangle$ in less than 10 µs. Once initialized to this pure state, coherent operations such as Raman sideband cooling, single qubit rotations, and entangling gates can commence. These will be described in the next chapter.

2.4.3 State detection

Qubit state detection is a critical step in every experiment. Regardless of the coherent operation performed, we detect the qubit states the same way, using fields similar to the cooling and optical pumping beams. Figure 2.8(c) shows the frequencies involved. The detection beam has no sidebands and is resonant with the ${}^2S_{1/2}|F=1\rangle \leftrightarrow {}^2P_{1/2}|F=0\rangle$ transition as in the Doppler cooling and optical pumping cycles. Because selection rules prevent the excited state from decaying to the $|0\rangle$ state, if the qubit is in the $|1\rangle$ state, it will scatter many photons before eventually leaking to the $|0\rangle$ state via off-resonant coupling to the ${}^2P_{1/2}|F=1\rangle$ manifold [49]. Conversely, if the qubit is in the $|0\rangle$ state, it will scatter no photons because the nearest transition is over 14 GHz away. The relationship between the qubit state and its brightness during detection inspires the terms “bright” and “dark” for the

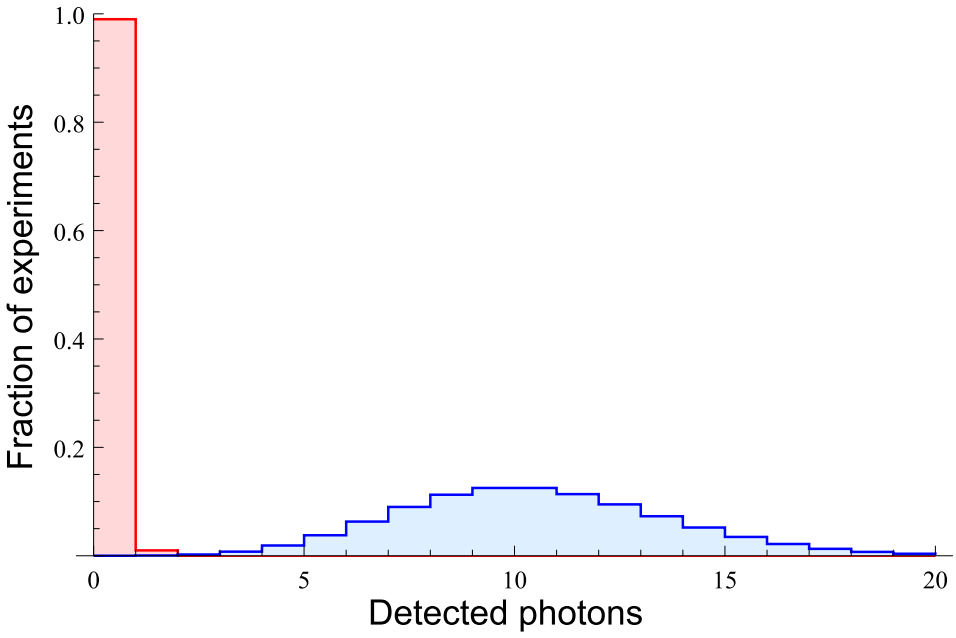

Figure 2.9: Theoretical state detection histogram.
The histogram plots detected photons over many experiments for the $|0\rangle$ state (red, average = 0.01) and the $|1\rangle$ state (blue, average = 10).

$|1\rangle$ and $|0\rangle$ states. This stark contrast in fluorescence depending on the qubit state allows high fidelity state detection for relatively short detection times. We collect about 10 photons on average for a detection time of about 600 µs. During this time, we apply the detection beam continuously while collecting the fluorescence using a PMT. To a good approximation, the probability of a photon emission is independent of when the previous photon was emitted, and so the distribution of measured photons over many detection cycles obeys Poissonian statistics. Figure 2.9 shows a theoretical illustration of the histograms of detected photons over many experiments for the two qubit states. The lack of significant overlap between the distributions makes "single shot" state determination a relatively accurate method. In a single experiment, the state of the qubit is measured to be bright if the number

of photons is above an optimized discriminator value of one and dark if it is below this threshold. Theoretically, the error in this method is below 2% using typical collection efficiencies of 0.001 (1 out of 1000 photons) [49].

Errors in state detection and the associated detection fidelity are influenced by a wide variety of factors. There are negligible errors associated with off-resonant coupling to the $^3[3/2]_{1/2}|F=1\rangle$ manifold during the relatively infrequent depopulation of the $^2D_{3/2}$ levels by the 935 nm beam. The dominant error stems from the off-resonant coupling to the $^2P_{1/2}|F=1\rangle$ manifold mentioned earlier, which "redistributes" some bright state counts to the lower bins of the bright state histogram by truncating the fluorescence of an initially bright ion [49,50]. This off-resonant pumping is directly proportional to the saturation parameter $s \equiv I/I_{sat}$ and is minimized by reducing the detection beam intensity.

In the experiments described in this thesis, the bright state histograms deviate significantly from this theoretical ideal. Due to causes unknown, our bright state appears to experience excess optical pumping to the dark state during the detection cycle, even at low intensities. The bright state histogram displays a "shelf" of counts in the first few bins much higher than theory predicts, decreasing our state discrimination fidelity to $\sim$93%, where the optimal threshold value is two photons. Fortunately, very few of our measurements require single shot detection. Most of the data presented here determines state populations in the more classical sense of the phrase, by fitting functions to the complete detection histogram. In other words, for experiments where single shot detection is not required, it is more accurate to fit the acquired histogram to basis functions experimentally measured after deliberate state

preparation. For example, consider the case when light from two ions is collected during detection. The two qubits can be in one of three possible states, $|j\rangle$, where $j = \{0, 1, 2\}$ denotes the number of qubits in the bright state. The measured histogram will be composed of a linear superposition of these distinct distributions $D_j(n)$,

$$D(n) = P_0 D_0(n) + P_1 D_1(n) + P_2 D_2(n) \tag{2.27}$$

where $D(n)$ is the fraction of M experiments where n photons are collected (hence, $\sum_n D(n) = M$) and P_j is the fraction of population in the state $|j\rangle$. More specifically, P_0 corresponds to $\rho_{|00\rangle\langle 00|}$, P_1 corresponds to $\rho_{|01\rangle\langle 01|} + \rho_{|10\rangle\langle 10|}$, and P_2 corresponds to $\rho_{|11\rangle\langle 11|}$, where $\rho_{|lm\rangle\langle lm|}$ are the diagonal elements of the two-qubit density matrix. The basis states themselves are obtained by deliberately preparing each $|j\rangle$ state using optical pumping and qubit rotations, typically using microwaves as described in Section 3.1. Subsequent experimental populations P_j are then calculated by fitting the measured $D(n)$ to the $D_j(n)$ using standard numerical fitting techniques.

The detector we use to count photons from the ions' fluorescence is a 32-channel PMT array *, combining the advantage of individual qubit state detection with high quantum efficiency (>30%) and a low dark count rate (∼10 Hz). The channels have 800 µm wide and 1000 µm tall active regions, partitioned by a 200 µm inactive area. We image the ions onto the channels as evenly as possible, given that the ion spacing is not uniform. Since the optical spillover from one ion's

*Hammamatsu-7260-200

fluorescence to adjacent channels is large, we magnify the ion chain to image the ions onto every other channel to achieve an optical crosstalk of less than 2%. There is a small ∼2% intrinsic crosstalk between adjacent channels, meaning that a photon impinging on one channel can also register on the adjacent channel due solely to the electronics, but this is negligible for non-adjacent channels. The PMT array raw output is amplified and digitized for TTL output by a custom pre-amplifier board. The TTL signals are ultimately relayed to the experimental control sequencer via a field-programmable gate array (FPGA) that acts as a multiplexer, allowing our experimental control software to combine arbitrary sets of channel data and send the result to arbitrary output channels. This makes it easy in a programmatic way to selectively measure, for example, the two-qubit populations $|j\rangle$ of different pairs of ions in a chain.

2.5 Optical systems

This section details the generation and delivery of the laser beams described above. For reference, the complete optical layout for the experiments is illustrated in Figure 2.10

2.5.1 369 nm light

Our 369.5 nm (811.2888100 THz) light is generated by frequency doubling the 739 nm output of a Toptica TA 100, an external cavity diode laser that uses a tapered amplifier to output a total power of ∼250 mW. About 200 mW of this light

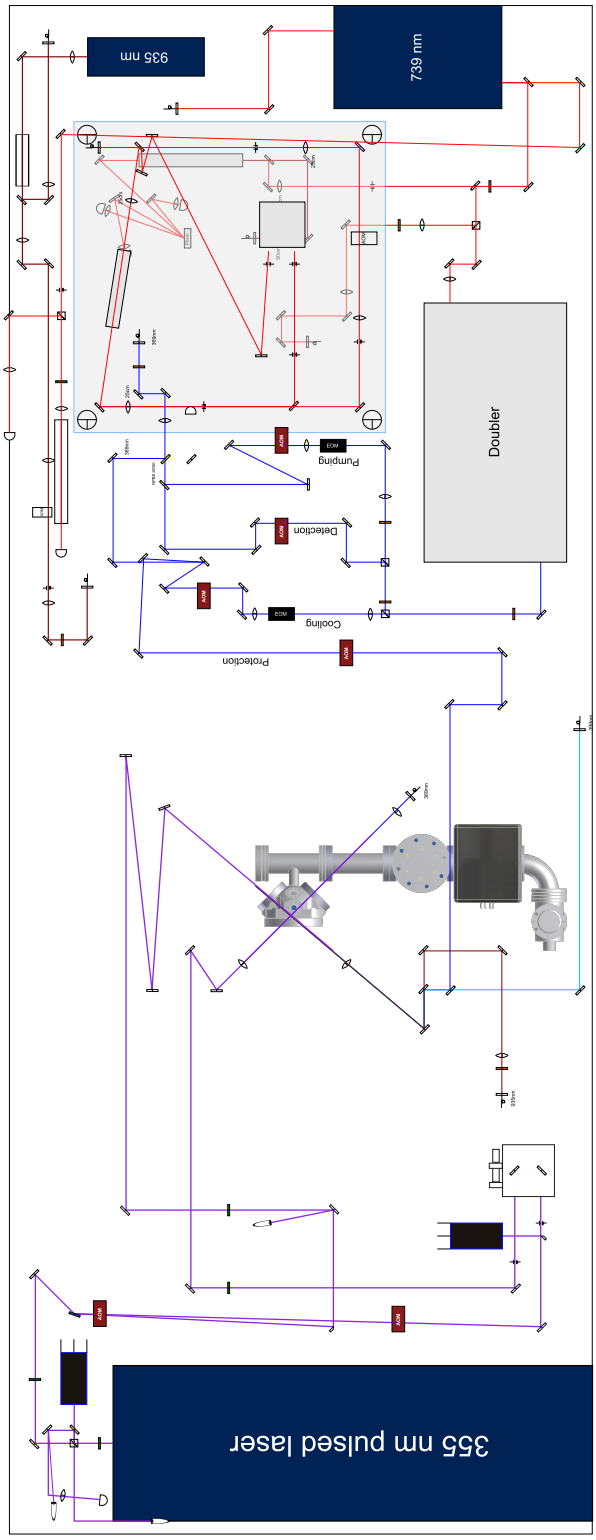

Figure 2.10: Complete optical layout.

pumps the doubler cavity in a Spectra-Physics WaveTrain frequency doubler. The doubler outputs a clean Gaussian TEM_{00} collimated beam with 2 mW at 369 nm. This output is distributed into three separate beams using polarizing beam cubes and $\lambda/2$ waveplates. Refer to Figure 2.11 for the optics associated with the generation and delivery of the 369 nm light. The cooling and pumping beams pass through their EOMs before the acousto-optic modulators (AOMs), which switch the beams on and off throughout the experiment as well as provide frequency offsets between the beams. The detection and pumping beam AOMs are driven at 300 MHz while the cooling beam AOM is driven at 290 MHz *. The three beams are recombined using two non-polarizing beam splitters. Although this method is power inefficient, it allows for independent control of the beam polarizations. The colinear beams are coupled into a fiber whose output coupler is mounted on a translation stage aimed directly at the trap. The output divergence is shaped by a high numerical aperture MicroLaser fiber collimator and a cylindrical lens, creating a roughly 10 µm× 100 µm spot size at the ion crystal to apply uniform intensity across the chain.

Both the frequency and the intensity of the 369 nm beam must be stabilized. The 20 MHz linewidth is relatively narrow, and at the lower intensities used for cooling and detection, the scattering rate γ_s will vary significantly if the laser frequency drifts more than $\sim$1 MHz. According to the scattering rate equation for an

*IntraAction ASM-3002B8

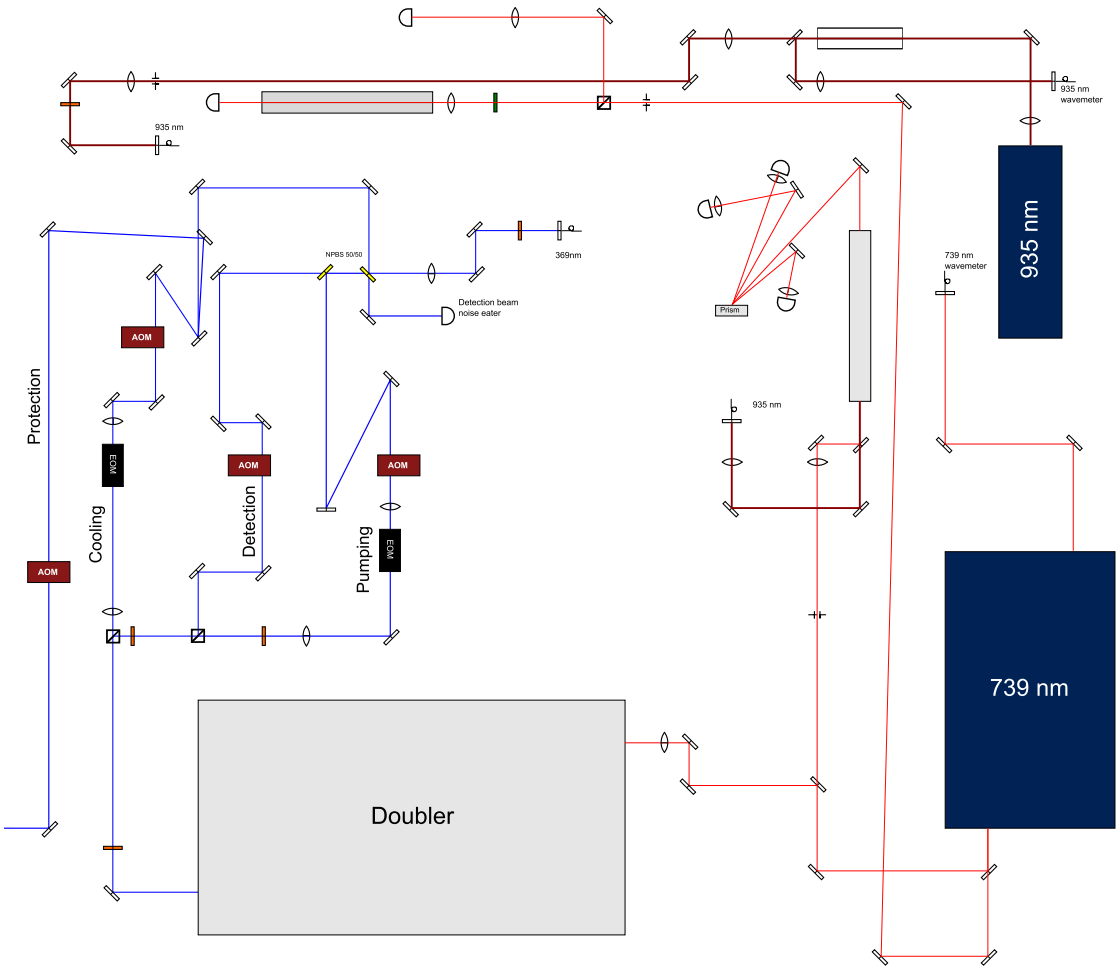

Figure 2.11: 369 nm and 935 nm light generation and delivery.

ion moving at velocity $\mathbf{v}(t)$ in a wave with vector $\mathbf{k}$,

$$\gamma_s = \frac{s\ \Gamma/2}{1 + s + \left(\frac{\Delta - \mathbf{k}\cdot\mathbf{v}(t)}{\Gamma/2}\right)^2}, \tag{2.28}$$

so a detuning $\Delta = 5$ MHz will decrease the ion brightness by over 10%. Likewise, a 10% fluctuation in the intensity will change the brightness ∼5%. The stabilization of the frequency involves multiple locking mechanisms. For passive stability, we lock the frequency of the 739 nm light to the length of a mechanically stable Fabry-Pérot optical cavity using the Pound-Drever-Hall (PDH) technique [51]. The ∼50 µW for the lock is picked off from the laser output through the first mirror at the output. The ∼30 MHz sidebands on the 739 nm light are produced by directly modulating the master diode current via a bias-T. The PDH error signal is split into high and low frequency components using a low-pass filter. The high frequency signal is input to a proportional-integral-derivative controller (PID) that controls the diode current via a field-effect transistor. The low frequency component is input to a PID that controls the master diode cavity grating angle via a piezo-electric transducer (PZT). The PDH cavity body is machined Invar, a nickel-iron alloy notable for its uniquely low coefficient of thermal expansion, typically ∼1 ppm/°C. The resonance condition for the cavity demands that its optical path length equal an integer multiple of half wavelengths:

$$L = m\ \lambda/2 \tag{2.29}$$

For $\lambda = 739.05$ nm and a PDH cavity length of 15 cm, $m \simeq 41600$. A 0.1°C temper-

ature drift will result in a length change of 15 cm$\times$(1 ppm/°C)$\times$0.1°C $\simeq$ 1 nm. The resonance wavelength is then shifted by 1 nm/41600, corresponding to a frequency shift on the order of 100 MHz. Since the lab temperature can fluctuate by this amount on the timescale of minutes, we require an additional lock to an absolute frequency source. We use one of the myriad transitions in an iodine (I_2) vapor for this purpose. An iodine vapor cell is heated to over 500°C in order to access a strong transition that is 13.39 GHz blue of the 739 nm wavelength corresponding to the $^2S_{1/2} \leftrightarrow {}^2P_{1/2}$ transition [52]. A portion of the 739 nm light is coupled through a broadband fiber-EOM *, which we use to apply a 13.31 GHz sideband. This light is then used for the Doppler-free absorption spectroscopy of the iodine lines. It is split into counter-propagating pump and probe beams that overlap in the vapor cell. The probe beam intensity is measured by a Nirvana auto-balanced photoreceiver that suppresses common mode intensity fluctuations. To increase the signal to noise ratio to an adequate level, we must use lock-in amplification to ultimately produce the error signal. The probe beam is the first-order deflection of an 80 MHz AOM that is amplitude modulated at 22 kHz. The lock-in amplifier then takes the photoreceiver output and the 22 kHz frequency reference as inputs. Finally, the output of the lock-in amplifier is input to a PID that controls the length of the PDH cavity via its PZT voltage. When the iodine lock is engaged, the laser frequency is stable to $\sim$1 MHz over hours. It is more stable than the HighFinesse WSU wavemeter used to measure all of our laser frequencies, which can drift tens of MHz over the course of the day. Hence, we periodically calibrate the wavemeter to the locked 739 nm

*EOSpace

frequency. The iodine lock itself is very slow, on the order of 1 s due to the long integration time required for the lock-in amplifier, but the PDH lock has a much higher bandwidth (> 1 kHz) for fast noise. Ultimately, our 369 nm frequency stays within about ± 500 kHz of resonance, which is sufficient to maintain a stable fluorescence rate and consistent Doppler cooling.

The detection beam intensity must also be stabilized. We accomplish this using a "noise eater" circuit [53]. The rf signal that drives the detection beam AOM passes through a voltage-controlled attenuator (VCA). The detection beam leakage through the non-polarizing beam splitter is measured using a photodiode that generates a signal directly proportional to the detection beam intensity. This signal amplitude is digitized and compared to a set point by an FPGA in the noise eater circuit. The difference generates an error signal that is minimized by modulating the detection beam AOM rf signal via the VCA voltage. The relatively long distance between the detector and the optical fiber input coupler makes the output beam susceptible to power fluctuations caused by air-driven beam steering and the sensitivity of fiber mode matching. To mitigate this problem, we covered the detection beam as much as possible along that path. Since the lock cannot feed back to suppress these fast fluctuations, its primary purpose is to stabilize the intensity against slow power drifts. Because the measured beam intensity is by necessity on the output side of the AOM, the feedback must be activated only during the detection cycle of the experiment when the detection beam is on. This toggle is controlled by the experimental sequencer (see Section 2.6). During the majority of the time when the beam is off, the noise eater circuit simply holds its current VCA voltage.

2.5.2 935 nm light

The repumper at 935 nm is produced by a Toptica DL100 external cavity diode laser very similar to the 739 nm laser, except there is no tapered amplifier stage. The majority of the beam power is coupled into a fiber-EOM that produces the 3.1 GHz sidebands. The output is overlapped with the photoionization beam and ∼5 mW is delivered to the trapping zone. A small portion of the power before the fiber-EOM is diverted to the wavemeter, which is used not only for frequency monitoring but also for locking the laser. The abundance of power in the beam broadens the transition linewidth so much that a more precise lock is unnecessary. The wavemeter simply compares the measured value to a set point and a software PID controls an analog voltage directly applied to the diffraction grating PZT of the diode cavity. The feedback is very slow and the frequency typically fluctuates ±10 MHz, but this variation has no deleterious effects.

2.5.3 355 nm light

The quantum gates and coherent operations are driven by the beat note between one or two pairs of Raman beams. The details of the atom-light interaction are explained in the next chapter, but this section will describe the optical characteristics of the Raman beams and how we control the beat note to maintain coherence with the qubit.

The Raman beams are generated from the output of a 355 nm Spectra-Physics Vanguard mode-locked laser. The UV light is produced by a neodymium-doped

vanadate crystal (Nd:YVO_4) that combines 1064 nm pump light with its separately doubled 532 nm light to yield a 355 nm beam by sum frequency mixing. The output average beam power is nominally 4 W. The beam consists of a train of ∼12 ps wide pulses at a repetition rate of 80.5978 MHz. Our interactions with the light are slow enough that the spectrum of the light is a frequency comb, where the comb teeth are separated by the repetition rate with linewidths inversely proportional to the interaction time (that is, inversely proportional to the number of pulses observed). The overall bandwidth of the frequency comb is proportional to the inverse of the pulse width, providing us with enough bandwidth to span the qubit splitting.

There are several significant advantages to using this 355 nm light for stimulated Raman transitions in our $^{171}Yb^{+}$ qubit system. The first advantage is the available optical power. These Vanguard laser systems are industrial devices used in the manufacture of semiconductors, where the high instantaneous intensity is a critical requirement. This renders the systems more affordable and well-engineered. Additionally, the uniform comb spacing and the phase relationship between the comb teeth allows beat notes between multiple combs to add coherently, effectively doubling the power efficiency [54,55]. The higher optical power enables stronger coupling strengths for faster gates. Another advantage specific to our Raman transitions in $^{171}Yb^{+}$ involves the suppression of errors associated with unwanted spontaneous emission and differential AC Stark shifts. At 355 nm, the nearest atomic transition from the ground state is to the $^2P_{1/2}$ state 33 THz away. Since the off-resonant spontaneous emission rate is proportional to the ratio of the Rabi frequency to the detuning, the spontaneous emission rate can be suppressed by detuning as far as

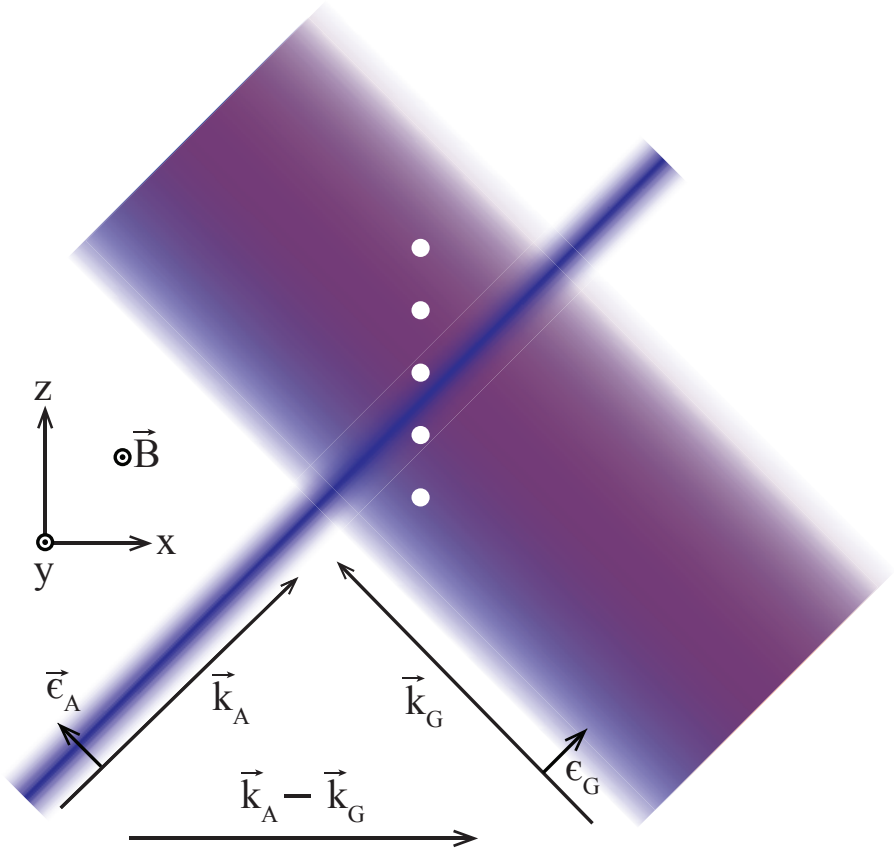

Figure 2.12: Raman beam geometry.
The two beams intersect at 90° to each other and 45° to the ion crystal axis, imparting momentum in the transverse direction. The polarizations are linear and mutually orthogonal to each other and the magnetic field out of the page.

possible while increasing the power to maintain the desired Rabi rate Ω. At 33 THz, the spontaneous scattering rate is negligible at $\sim 10^{-6}\ \Omega$. With increased power, another concern is the differential AC Stark shift of the qubit levels [37] that can in principle lead to decoherence as the laser power experiences small fluctuations. Serendipitously, 355 nm is almost the ideal wavelength for minimizing the differential shift, which is only $\sim 10^{-4}\ \Omega$. The near cancellation is due to competing shifts from contributions from both the $^2P_{1/2}$ and $^2P_{3/2}$ levels, since the first is red detuned and the other is blue detuned from 355 nm.

Figure 2.10 shows the optical layout of our 355 nm beams. The Vanguard output passes through two inline AOMs to make more efficient use of the available power. The first Raman beam (R_A) is generated by the first negative order of an 80 MHz AOM (AOM_A). The undeflected portion passes through the second AOM (AOM_G), driven at ∼250 MHz, whose first positive order is the second Raman beam (R_G). Figure 2.12 illustrates the beam geometry at the ions. The addressing beam, R_A, passes through an objective that focuses it tightly (∼3 µm waist) at the ion chain. The global beam, R_G, first travels through a delay stage before intersecting R_A at the ions. The global beam is focused by cylindrical lenses to have a tight (10 µm waist) vertical focus and a wide (∼100 µm) horizontal waist to illuminate all the ions as equally as possible. AOM_G is driven by the arbitrary waveform (AWG) generator described in the next section. AOM_A is driven by an HP8640 frequency generator and is responsible for maintaining the precise beat note between the Raman beams necessary for coherent control of the qubits.

The delay stage is critical for temporal overlap of the pulses. Even though we operate in the frequency comb regime where many pulses interact with the ions over the duration of the gate, the stimulated Raman transition is a two-photon process. Two beams must be coincident to provide the atom with a photon to absorb from one optical field and then coherently emit into the other. At 12 ps wide, the pulses are only 3 mm long in space, with pulses separated along the beam path by 3.7 m. Therefore the Raman beam optical path lengths must be identical to within a few centimeters so that the displacement of a delay stage is sufficient to overlap the pulses. In practice this coarse alignment is performed by scattering the beams off

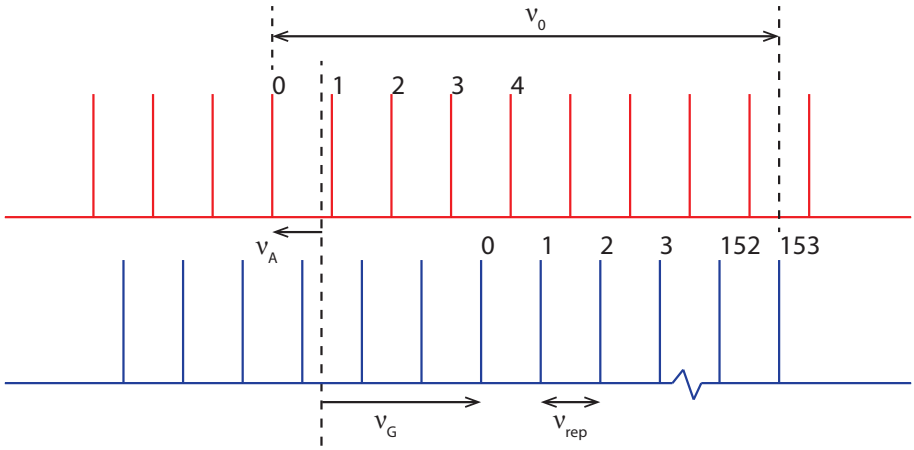

Figure 2.13: Tuning the beat note between 355 nm frequency combs. The AOM frequencies ν_A and ν_G are adjusted to bring the beat notes between pairs of comb teeth into resonance ν_0 with atomic transitions, which are within a range ± 5 MHz of the qubit frequency. The comb teeth are separated by the pulsed laser repetition rate ν_{rep}.

an electrode and using a high-resolution TDC to compare the pulse arrival times.

We precisely tune the Raman beat note by controlling the frequency of AOM$_G$. Given a repetition rate ν_r and AOM frequencies ν_A and ν_G, the condition for resonant beat notes is given by $\nu_0 = m\nu_r - |\nu_A - \nu_G|$, where ν_0 is the qubit splitting and the sign of $\nu_{A,G}$ denotes the positive or negative diffraction orders. Figure 2.13 illustrates the beat note between the two frequency combs. For the entangling gate described in the next chapter, AOM$_G$ is actually driven with two frequencies simultaneously, red and blue of ν_0, such that there are three frequency combs involved.

Since the qubit frequency spans 157 comb teeth at our repetition rate, a small fluctuation in the Vanguard cavity length causes the frequency comb to expand like an accordion, magnifying a small shift in ν_r. For example, a 1 µm change in the laser cavity length (or a $\sim 10^{-7}$ change in the repetition rate) would shift the beat note over 5 kHz, which is a non-negligible shift in the detuning of our gates. Instead

of feeding back to an active element in the Vanguard, we lock the beat note using a feed forward approach to continuously adjust the frequency of AOM_A [56, 57]. We pick off the excess 532 nm light from the laser and direct it to a high frequency photodiode that picks up the ∼13 GHz comb line signal. This passes through a bandpass filter and a few amplifiers before mixing with local oscillator signal from a microwave synthesizer *. The local oscillator is phase coherent with the qubit and is set to a frequency that makes the output of the mixer, ν_{ref}, within the bandwidth of AOM_A. Using a simple phase locked loop circuit, the instantaneous drive frequency ν_A is mixed with ν_{ref} to generate an almost DC signal (removing the sum frequency with an appropriate filter). This signal is the error signal fed into a PID, the output of which is input to the frequency modulation control of the analog rf generator driving AOM_A. This technique allows AOM_A to continually compensate for repetition rate fluctuations that would otherwise detune the beat note.

2.6 Experimental control system

The experimental control system consists of a general purpose computer running custom software and an FPGA operating as both a sequencer and a data acquisition device. The control software is almost completely written in LabView, which directly interfaces with the experimental apparatus via USB, GPIB, and RS-232 protocols, depending on the device. Direct computer control is only possible when the operations can be executed slower than several milliseconds due to the

*HP8672A 2-18 GHz frequency synthesizer

typical latency of communication. The time scales of our actual experiments are several orders of magnitude faster than can be controlled by the computer directly, which is why we use an FPGA for the sequencer. The purpose of the sequencer is to execute a sequence of events repeatedly with fine timing precision and to acquire and relay the resultant data. Once we specify a particular experimental sequence, including how many times it should repeat, it is uploaded to the sequencer and triggered. The sequencer executes the sequence by controlling devices via precisely timed output TTL pulses. Some of the TTL signals toggle rf switches while others act as trigger pulses. To toggle the application of laser beams, the rf signals driving the associated AOMs are switched on and off by TTL-controlled rf switches prior to their respective amplifiers. These rf switches typically provide a signal attenuation on the order of 60 dB. Our experiments also require the synchronized output of two digital waveforms. The first waveform is generated by an AWG *. This waveform drives the AOM of the global Raman beam and so controls the coherent evolution of the quantum state. The second waveform is generated by a high speed digital-to-analog converter (DAC) †. The DAC supplies the dc electrode voltages both in a static configuration and when they are smoothly varied between multiple configurations in order to shuttle the ions. The synchronization of the operations controlled and triggered by the sequencer requires that the FPGA, AWG and DAC clocks are stable to within 1 µs over the course of a single experiment, which lasts ∼10 ms.

*Chase Scientific Company DA12000-12-4M-PCI Arbitrary Waveform Generator
†National Instruments PXI-6713

Chapter 3: Quantum gates

A general quantum algorithm consists of both single qubit quantum gates and multi-qubit quantum gates. This chapter describes the theory behind these two types of gates and how we implement them in the lab.

3.1 Single qubit gates

Single qubit gates are often called qubit "rotations" due to the concept of the Bloch sphere. This picture can be a useful way to visualize qubits, so it is worth introducing. A classical bit can exist in either of two discrete states, 0 or 1, with associated real-valued probabilities a and b, where $a + b = 1$. The density matrix specifying the state of this bit is given by

$$\rho = \begin{pmatrix} a & 0 \\ 0 & b \end{pmatrix} = \begin{pmatrix} a & 0 \\ 0 & (1-a) \end{pmatrix}. \tag{3.1}$$

Since $b = 1 - a$ must be true to conserve probability, a single real number is all that is required to unambiguously specify the state. One can define an "angle" θ such that $a = \cos^2\theta$ (and therefore $b = \sin^2\theta$), where θ ranges from 0 to $\pi/2$. A quantum bit, however, can exist in a superposition of the two states. If this state is known

with certainty, it is in a pure state, which can be written

$$|\psi\rangle = \alpha|0\rangle + \beta|1\rangle. \tag{3.2}$$

Now, the values of α and β are complex, and can be written in the form $\alpha = Ae^{i\phi_\alpha}$ and $\beta = Be^{i\phi_\beta}$. The conservation of probability demands $1 = |\alpha|^2 + |\beta|^2 = A^2 + B^2$. Similar to the classical bit case, $A = \cos\theta$ (and therefore $B = \sin\theta$). The phases remain free parameters, but because an overall quantum state phase is not physically observable, it suffices to define the relative phase $\phi \equiv \phi_\beta - \phi_\alpha$ such that the pure qubit state can be written

$$|\psi\rangle = \cos(\theta/2)|0\rangle + e^{i\phi}\sin(\theta/2)|1\rangle. \tag{3.3}$$

Hence, two parameters are necessary to fully specify the pure qubit state, and because the ranges of θ and ϕ are 0 to π and 0 to 2π, respectively, the qubit state can be pictured as a point on a sphere of unit radius as illustrated by Fig. 3.1.

We use either optical fields or microwaves to implement qubit rotations in the lab. The rotations driven by optical fields are discussed in Sec. 3.2.2, as they are necessary for multi-qubit gates or when individual rotations of qubits in an ion chain are needed. They are also more complicated physically, so here it is instructive to explain how microwaves are used to manipulate the qubits without getting lost in those details yet. The $^{171}Yb^+$ qubit states act very much like an ideal two-level system when driven by a monochromatic microwave field because there is very little

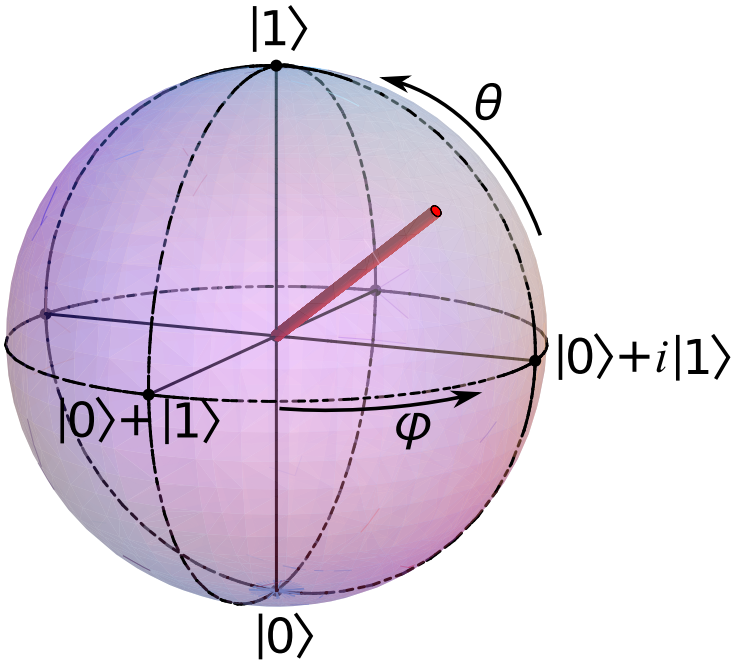

Figure 3.1: Bloch sphere

coupling to the other energy levels, which allows a simple model Hamiltonian to yield a useful evolution operator for our single qubit gates.

To derive the single qubit rotation operator, we start with the unperturbed Hamiltonian of a single qubit,

$$\hat{H}_0 = \frac{\hbar\omega_0}{2}\hat{\sigma}_z \tag{3.4}$$

where $\hat{\sigma}_z = |0\rangle\langle 0| + |1\rangle\langle 1|$ is the Pauli-Z operator and ω_0 is the qubit splitting. We perturb the qubit by a microwave field $\mathbf{B}(t)$ of frequency ω,

$$\mathbf{B}(t) = \frac{1}{2}\vec{B}_0 e^{i(\omega t+\phi)} + \frac{1}{2}\vec{B}_0 e^{-i(\omega t+\phi)} \tag{3.5}$$

which contributes the Hamiltonian term

$$\hat{H}_I = -\hat{\mu} \cdot \mathbf{B}(t). \tag{3.6}$$

The magnetic moment operator $\hat{\mu}$ can be written in terms of the atomic raising and lowering operators using its matrix elements in the qubit state basis:

$$\begin{aligned}
\vec{\mu} &\equiv \langle 1|\hat{\mu}|0\rangle \\
\hat{\mu} &= \vec{\mu}|1\rangle\langle 0| + \vec{\mu}^*|0\rangle\langle 1| \\
&= \vec{\mu}\hat{\sigma}_+ + \vec{\mu}^*\hat{\sigma}_-
\end{aligned}$$

The interaction Hamiltonian becomes

$$\begin{aligned}
\hat{H}_I &= -\frac{1}{2}\left(\vec{\mu}\sigma_+ + \vec{\mu}^*\sigma_-\right) \cdot \left(\vec{B_0}e^{i(\omega t+\phi)} + \vec{B_0}e^{-i(\omega t+\phi)}\right) \\
&= -\frac{\hbar}{2}\left(\Omega e^{-i(\omega t+\phi)} + \Omega e^{i(\omega t+\phi)}\right)\sigma_+ - \frac{\hbar}{2}\left(\Omega^* e^{-i(\omega t+\phi)} + \Omega^* e^{i(\omega t+\phi)}\right)\sigma_-
\end{aligned}$$

where $\Omega \equiv \vec{\mu} \cdot \vec{B_0}/\hbar$. The general qubit state is given by

$$|\Psi(t)\rangle = c_0(t)|0\rangle + c_1(t)|1\rangle \tag{3.7}$$

and can be expressed in the basis of the unperturbed Hamiltonian's eigenstates according to

$$|\Psi\rangle = \sum_n c_n|\psi_n\rangle \tag{3.8}$$

Before solving the Schödinger equation to obtain the state evolution, it should be cast into a more useful form:

$$
\begin{aligned}
i\hbar\frac{\partial}{\partial t}|\Psi\rangle &= \hat{H}|\Psi\rangle \\
i\hbar\frac{\partial}{\partial t}\sum_n c_n|\psi_n\rangle &= \hat{H}\sum_n c_n|\psi_n\rangle \\
i\hbar\sum_n \dot{c}_n|\psi_n\rangle &= \sum_n c_n\hat{H}_0|\psi_n\rangle + \sum_n c_n\hat{H}_I|\psi_n\rangle \\
\langle\psi_m|\left(i\hbar\sum_n \dot{c}_n|\psi_n\rangle\right) &= \langle\psi_m|\left(\sum_n c_n\hat{H}_0|\psi_n\rangle + \sum_n c_n\hat{H}_I|\psi_n\rangle\right) \\
i\hbar\dot{c}_m &= c_m E_m + \sum_n c_n\langle\psi_m|\hat{H}_I|\psi_n\rangle \qquad (3.9)
\end{aligned}
$$

This is a set of coupled differential equations whose solutions $c_n(t)$ describe the quantum state for all time via Eqn (3.8). For the two-level qubit, the equations are simply

$$
\begin{aligned}
i\hbar\dot{c}_0 &= c_0E_0 + c_0\langle 0|\hat{H}_I|0\rangle + c_1\langle 0|\hat{H}_I|1\rangle \\
i\hbar\dot{c}_1 &= c_1E_1 + c_0\langle 1|\hat{H}_I|0\rangle + c_1\langle 1|\hat{H}_I|1\rangle
\end{aligned}
$$

Evaluating the matrix elements with $E_0 = 0$ and $E_1 = \hbar\omega_0$, they become

$$
\begin{aligned}
i\dot{c}_0 &= -c_1\frac{\Omega^*}{2}\left(e^{i(\omega t+\phi)} + e^{-i(\omega t+\phi)}\right) \\
i\dot{c}_1 &= c_1\omega_0 - c_0\frac{\Omega}{2}\left(e^{i(\omega t+\phi)} + e^{-i(\omega t+\phi)}\right)
\end{aligned}
$$

Transforming to the frame rotating at the qubit frequency ω_0 by using the change

of variables $\tilde{c}_0 = c_0$ and $\tilde{c}_1 = c_1 e^{i\omega_0 t}$ produces

$$i\dot{\tilde{c}}_0 = \frac{\Omega^*}{2}\tilde{c}_1\left(e^{i((\omega-\omega_0)t+\phi)} + e^{-i((\omega+\omega_0)t+\phi)}\right)$$
$$i\dot{\tilde{c}}_1 = \tilde{c}_1\omega_0 + \frac{\Omega}{2}\tilde{c}_0\left(e^{i((\omega+\omega_0)t+\phi)} + e^{-i((\omega-\omega_0)t+\phi)}\right)$$

At this point, the rotating wave approximation can be taken by discarding the terms that are oscillating rapidly relative to the other terms, since such terms will quickly integrate to zero when solving the Schödinger equation. The terms to drop are $(\omega + \omega_0)$ terms, since $\delta \equiv (\omega - \omega_0) \ll (\omega + \omega_0)$ [58]. The equations finally become

$$i\dot{\tilde{c}}_0 = \frac{\Omega^*}{2}\tilde{c}_1 e^{i(\delta t+\phi)}$$
$$i\dot{\tilde{c}}_1 = \frac{\Omega}{2}\tilde{c}_0 e^{-i(\delta t+\phi)}$$

The solutions for the state amplitudes exhibit so-called Rabi oscillation during the application of a nearly resonant beam. The Rabi frequency $\Omega' = \sqrt{\Omega^2 + \delta^2}$ is a function of field intensity and detuning, and the amplitude of the oscillation scales as $1/\Omega'$.

To construct the single qubit gate operator $\hat{R}(\theta, \phi)$, we apply it to the two basis states to calculate the operator's two rows, using the state amplitude solutions. For example, for the $|0\rangle$ state, the initial conditions $c_0(0) = 1$, $c_1(t) = 0$ yield

$$c_0(t) = \frac{i\Omega}{\Omega'}e^{i(\delta t/2+\phi)}\sin\left(\frac{\Omega' t}{2}\right)$$
$$c_1(t) = e^{-i\delta t/2}\left[\cos\left(\frac{\Omega' t}{2}\right) + \frac{i\delta}{\Omega'}\sin\left(\frac{\Omega' t}{2}\right)\right].$$

The operation $\hat{R}(\theta,\phi)|0\rangle$ should result in Eqn. 3.3. Solving similarly for the row associated with $|1\rangle$ completes the operator,

$$\hat{R}(\theta,\phi) = \begin{pmatrix} e^{i\delta t/2}\left[\cos\left(\frac{\theta}{2}\right) - \frac{i\delta}{\Omega'}\sin\left(\frac{\theta}{2}\right)\right] & \frac{i\Omega^*}{\Omega'}e^{-i(\delta t/2+\phi)}\sin\left(\frac{\theta}{2}\right) \\ \frac{i\Omega}{\Omega'}e^{i(\delta t/2+\phi)}\sin\left(\frac{\theta}{2}\right) & e^{-i\delta t/2}\left[\cos\left(\frac{\theta}{2}\right) + \frac{i\delta}{\Omega'}\sin\left(\frac{\theta}{2}\right)\right] \end{pmatrix} \tag{3.10}$$

where the rotation angle $\theta = \Omega' t$ and the basis state vectors are defined as

$$|0\rangle \equiv \begin{pmatrix} 1 \\ 0 \end{pmatrix}, |1\rangle \equiv \begin{pmatrix} 0 \\ 1 \end{pmatrix} \tag{3.11}$$

Applied pulses that rotate the qubit 180° (90°) are called "π pulses" ("$\pi/2$ pulses"), regardless of what phase rotation ϕ is induced. These basic pulses are used extensively in the experiments described later, where the notation $\hat{R}(\theta,\phi)$ typically refers to resonant or nearly resonant pulses ($\delta = 0$).

As mentioned earlier in Sec. 2.1, the qubit phase rapidly advances with respect to the lab frame (Eqn. 2.1). The coherent operations on the qubits rely on the phase coherence between the qubits and the synthesizers generating the fields that drive the their rotations. Additionally, the intrinsic qubit dephasing time must be much longer than the coherent operation time. Experimentally, these coherences are inextricable and are measured together by performing a simple Ramsey measurement. To measure the coherence time when using microwaves to globally rotate the qubits, we evolve the state of a qubit initialized to the $|0\rangle$ state as follows: $|\psi(t)\rangle = \hat{R}(\pi/2,0)\hat{\mathcal{I}}(t)\hat{R}(\pi/2,0)|0\rangle$, where $\hat{\mathcal{I}}(t)$ is the identity operator applied for

time t, meaning that the qubit freely evolves during that time. The microwave source is an HP8672A microwave synthesizer in conjunction with a PTS-310 rf synthesizer, which boosts the frequency resolution to ∼1 Hz. Both synthesizers are phase locked to an SRS FS725 rubidium frequency standard. A +35 dB amplifier increases the signal to ∼1 W, which passes through a circulator to a truncated waveguide ending in a horn aimed at the ions. Because the horn output is not perfectly mode-matched to free space, the third port of the circulator terminates in a 5 W dump so that the reflected signal does not feed back to the amplifier. Plotting the $|1\rangle$ state population $P_1 = |\langle 1|\psi(t)\rangle|^2$ as a function of the free evolution time t produces exponentially decaying Ramsey fringes, whose period is equal to the the inverse of the microwave detuning (∼40 Hz). The coherence time is quantified by the decay constant extracted from a numerical fit to the Ramsey data, as illustrated in Fig. 3.2.

3.2 Multi-qubit entangling gates

Quantum computation requires more than just single qubit gates. Quantum gates that entangle multiple qubits are also necessary. Entangling gates on trapped ions are much more complicated than simple qubit rotations for two related reasons. Fundamentally, if qubits are to become usefully entangled, they must interact in some precisely controlled way. By design $^{171}Yb^{+}$ qubits are well isolated from each other and their environment so that they can be pristine quantum memories. Instead of coupling to each other directly, the qubits interact via a quantum bus.

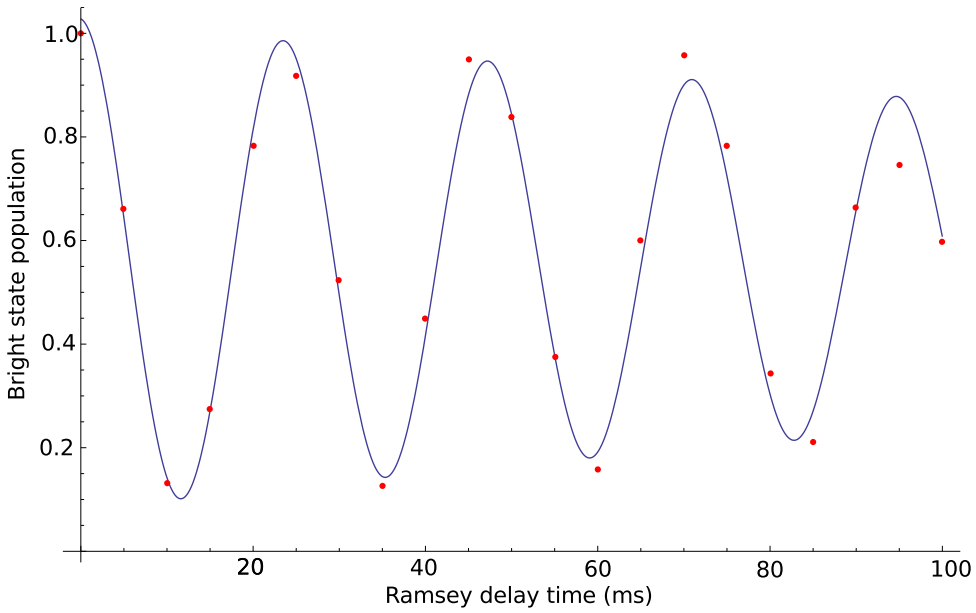

Figure 3.2: Coherence time measurement example.
Ramsey delay scan data. Nearly resonant microwave $\pi/2$ pulses are applied to a qubit initialized to the $|0\rangle$ state. The delay between the pulses is scanned while measuring the $|1\rangle$ state population. The numerical fit indicates a 250 ms coherence time.

In analogy to a classical computer bus, which is a communication system between connected components yet distinct from them, a linear chain of trapped ions uses their quantized collective motion to deterministically couple the qubits. To explain how this works, we must first understand how the ions participate in the normal modes of motion of the crystal. Then the central concept of spin-dependent forces will be introduced in order to describe the entangling interaction that actually constitutes the multi-qubit gate. In the process we will derive the stimulated Raman transitions that create the spin-dependent forces.

3.2.1 Normal modes of motion

The stable configuration of a linear ion crystal and the modes in which the ions vibrate are determined by the strong Coulomb repulsion between the ions balanced against the confining external potential. The criterion for maintaining a linear configuration for a given number of ions discussed in Sec. 2.3.8 is a clear example of the interplay of these opposing forces. Assuming the trap frequency ratio is sufficient to maintain a linear crystal, we can sketch a derivation of the normal modes of motion using a Lagrangian formulation from first principles, following the derivations in [59] and [60]. In contrast to previous related work, the gate pulse shaping described in the next chapter deliberately couples the qubits to multiple modes of motion, and so a relatively detailed description of the mode structure is necessary.

Before the normal mode frequencies and amplitudes can be calculated, the equilibrium positions of the ions must be determined. Consider a chain of N ions of mass M and charge e confined by an axial trap characterized by frequency ω. The total potential energy V of the system is the sum of this external trapping potential and the Coulomb repulsion between each ion pair,

$$V = \sum_{m=1}^{N} \frac{1}{2} M\omega^2 z_m(t)^2 + \sum_{\substack{n,m=1 \\ m\neq n}}^{N} \frac{e^2}{8\pi\epsilon_0} \frac{1}{|z_n(t) - z_m(t)|} \tag{3.12}$$

where $z_m(t)$ are the ion positions along the axial direction. When crystallized, the ions vibrate about their equilibrium positions $z_m^{(0)}$ by small displacements $q_m(t)$ such

that $z_m(t) \approx z_m^{(0)} + q_m(t)$. For clarity, let us dimensionalize the position coordinates by a parameter $l^3 \equiv \frac{e^2}{4\pi\epsilon_0 M\omega^2}$ such that $u_m \equiv z_m^{(0)}/l$ are the static equilibrium positions. These positions are where the forces balance, meaning that the derivative of the potential is zero:

$$0 = \left.\frac{\partial V}{\partial z}\right|_{z=z_m^{(0)}} \tag{3.13}$$

This generates a set of N coupled equations for the values u_m,

$$u_m - \sum_{n=1}^{m-1} \frac{1}{(u_m - u_n)^2} + \sum_{n=m+1}^{N} \frac{1}{(u_m - u_n)^2} = 0, \tag{3.14}$$

that can be solved numerically.

Now that we have the equilibrium positions, the next task is to find the normal mode frequencies and the associated vectors that describe how each individual ion participates in the modes. To keep the math simple, we will consider only axial motion first. This is possible because only trivial modifications to the resulting equations are needed to solve for the transverse modes that we use in the experiments. Assuming that the displacements are small enough to neglect terms of order q_m^3 and higher, the Lagrangian for the motion can be written as

$$L = \frac{M}{2}\sum_{m=1}^{N} \dot{q}_m^2 - \frac{1}{2}\sum_{n,m=1}^{N} q_n q_m \left.\frac{\partial^2 V}{\partial z_n \partial z_m}\right|_{q_m, q_n = 0} \tag{3.15}$$

where the second derivative is evaluated at the equilibrium positions u_m and u_n. The partial derivatives actually contain all the information we need for now. Solving

them and defining a matrix A_{nm}, where

$$A_{nm} = \begin{cases} 1 + 2\sum_{\substack{p=1 \\ p\neq m}}^{N} \frac{1}{|u_m - u_p|^3} & \text{if } n = m \\ -\frac{2}{|u_m - u_n|^3} & \text{if } n \neq m \end{cases} \tag{3.16}$$

the Lagrangian can be rewritten as

$$L = \frac{M}{2}\sum_{m=1}^{N} \dot{q}_m^2 - \omega^2 \sum_{n,m=1}^{N} A_{nm} q_n q_m. \tag{3.17}$$

Obtaining the Lagrangian that includes the transverse motion follows a similar derivation, but the math is more complicated. Conveniently, the analogous matrix K_{nm} associated with the transverse modes turns out to have a simple relationship with the axial matrix A_{nm} given by

$$K_{nm} = \left(\mathcal{A} + \frac{1}{2}\right)\delta_{nm} - \frac{1}{2}A_{nm} \tag{3.18}$$

where K_{nm} is defined similarly by the partial derivatives of the potential V along the transverse directions and $\mathcal{A}$ quantifies the trap anisotropy as defined in Sec. 2.3.8. The eigenvalues $(\omega_{t,k}/\omega_z)^2$ and eigenvectors $b_{k,m}$ of the equation

$$\sum_{n=1}^{N} K_{mn} b_{k,n} = \left(\frac{\omega_{t,k}}{\omega_z}\right)^2 b_{k,m} \tag{3.19}$$

provide the transverse normal mode frequencies $\omega_{t,k}$ and coupling parameters, respectively, where $k = \{1, 2, \cdots, N\}$ and $\omega_t \equiv \omega_{t,1}$. The axial normal mode frequen-

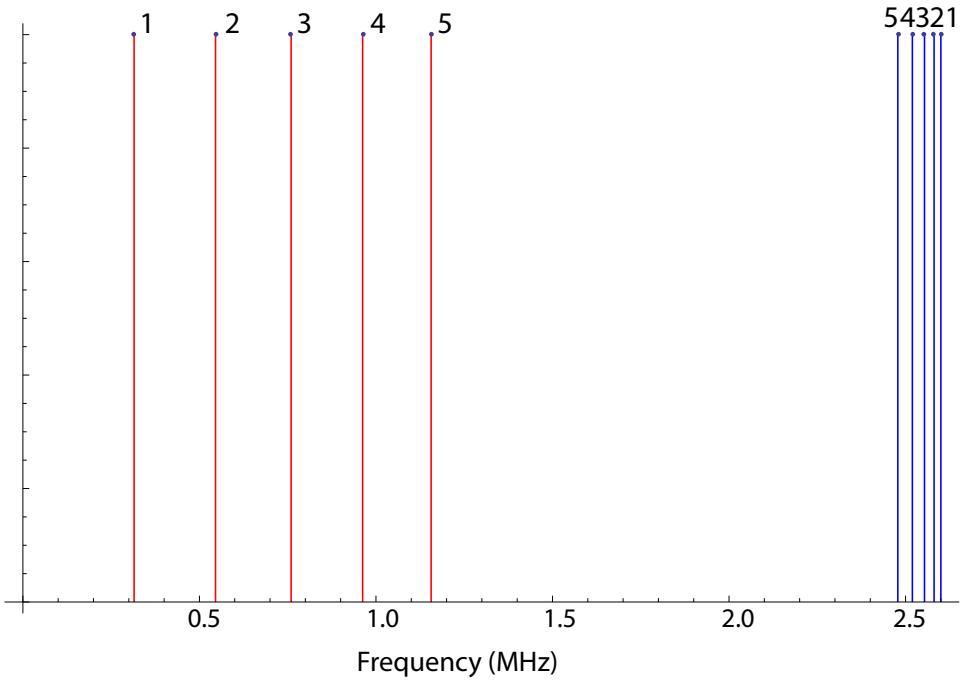

Figure 3.3: Motional mode spectrum.
Axial (red) and transverse (blue) mode frequencies for a five ion chain.

cies $\omega_{z,k}$ are related to the transverse mode frequencies in a very simply way as well, given by

$$2\left(\omega_t^2 - \omega_{t,k}^2\right) = \omega_{z,k}^2 - \omega_z^2 \tag{3.20}$$

where $\omega_z \equiv \omega_{z,1}$. This relationship shows an interesting difference between the transverse and axial modes, illustrated in Fig. 3.3, which is that the higher transverse modes have lower frequencies than the center of mass (CM) mode. Intuitively this makes sense because any relative ion motion transverse to the chain axis increases the distance between them, reducing their potential energy. Conversely for relative ion motion along the axis, there are always ions that are pushed closer together than when they move in the CM mode, increasing their potential energy.

The coupling parameters $b_{k,m}$, given by the eigenvectors of K_{mn}, describe how ion m couples to, or participates in, the k^{th} mode of motion. Figure 3.4 illustrates these parameters by plotting the values for each mode as a function of ion index for a five ion chain. The sign of each amplitude denotes the relative velocity of the ions as they vibrate about their equilibrium positions; hence, in the CM mode, all ions oscillate with the same phase and amplitude about the rf null, whereas in the tilt mode the end ions oscillate exactly out of phase while the center ion is stationary. These differences are important for understanding the entangling gates driven by segmented laser pulses in Ch. 4. Before that, however, we need to see how spin-dependent forces are used to generate the entangling interaction between the qubits.

3.2.2 Two qubit entangling interaction

The fundamental prerequisite for coupling an ion's qubit state (or its "spin") to its motion is applying a force to the ion. In the derivation of the single qubit gate operator in Sec. 3.1, the spatial part of the microwave field was ignored for didactic reasons. On a practical level this was justified because the wavelength (2.37 cm) is so much larger than the ion spacing ($\sim$5 µm) that there is no significant phase difference across the chain to consider. More importantly, as will become evident in the following derivation, the momentum imparted by microwave photons is simply too small to provide sufficient spin-motion coupling. Consequently we must use optical fields to drive Raman transitions to apply enough force to drive motion

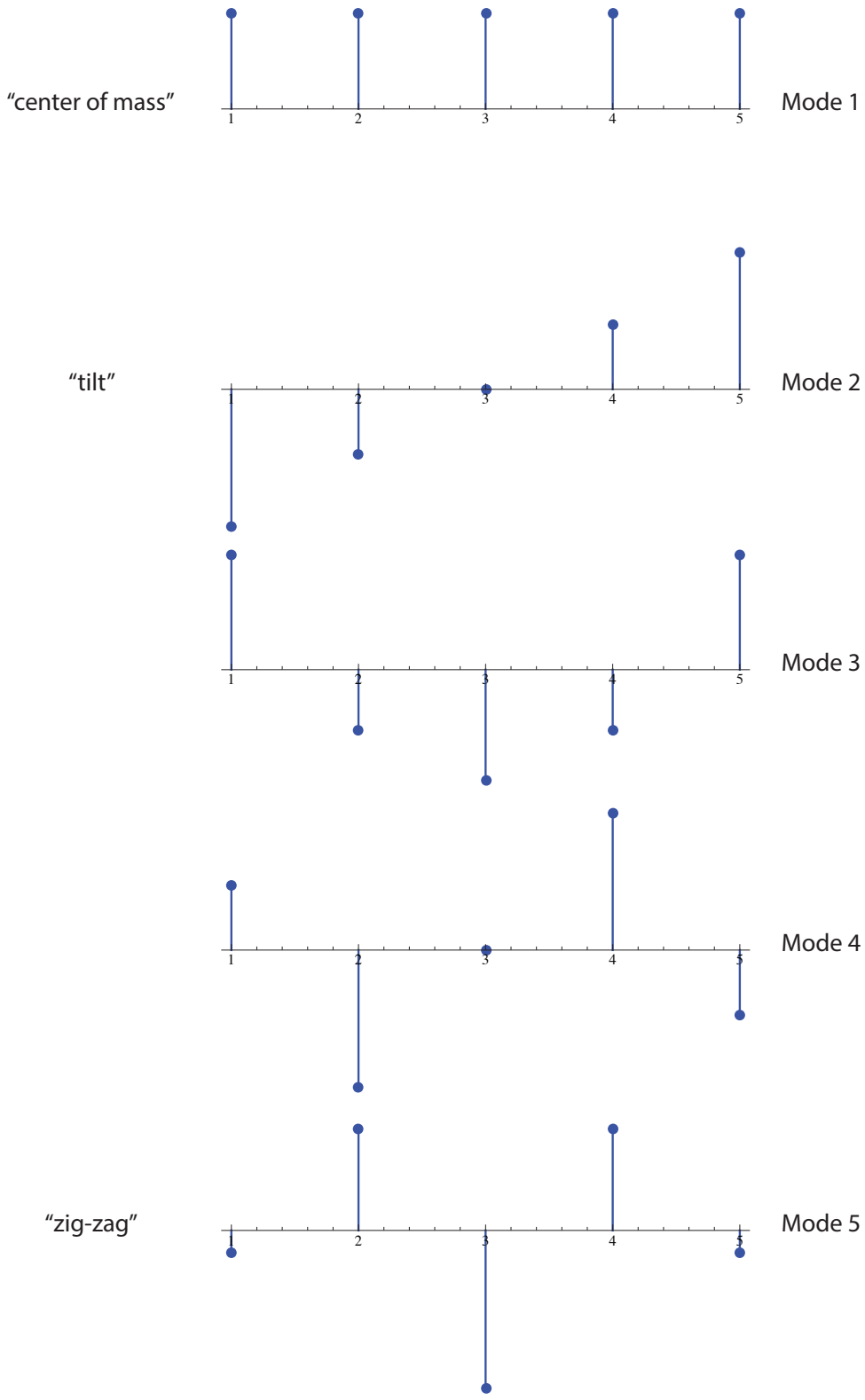

Figure 3.4: Normal mode parameters for a five ion chain.

while coherently manipulating the qubit states. The complete description of how we generate this interaction is incredibly complicated, partly because we use coherently contributing beat notes between frequency combs generated from the pulse train of a mode-locked laser instead of simple continuous wave beams [38,54,55], and partly because the real atomic levels involved are not just the three simplistic levels used below. These and other details will be discussed later in the context of how they impact the experiment. They are not, however, necessary for understanding the physics of the entangling interaction or how shaping the gate pulses improves the gates.

Here, we will consider a simple system of three atomic levels coupled by two continuous wave laser fields

$$\mathbf{E}(\mathbf{r},t) = \sum_{j=0}^{1} \frac{E_j}{2} \left(e^{i(\mathbf{k}_j \cdot \mathbf{r} - \omega_j t - \phi_j)} + e^{-i(\mathbf{k}_j \cdot \mathbf{r} - \omega_j t - \phi_j)} \right) \hat{\epsilon}_j \tag{3.21}$$

as illustrated in Fig. 3.5. The two beams have a beat note approximately equal to the qubit frequency, $\omega_0 - \omega_1 = \omega_{01} + \delta$, which will couple the qubit states $|0\rangle$ and $|1\rangle$. They are both detuned from an auxiliary excited state $|2\rangle$ by an amount $\Delta \equiv \omega_{02} - \omega_0$. For clarity, we will consider only a single ion and delay the introduction of the motional part of the interaction by neglecting the spatial part of the optical fields by dropping the $\mathbf{k} \cdot \mathbf{r}$ terms. Also temporarily neglecting the motion of the

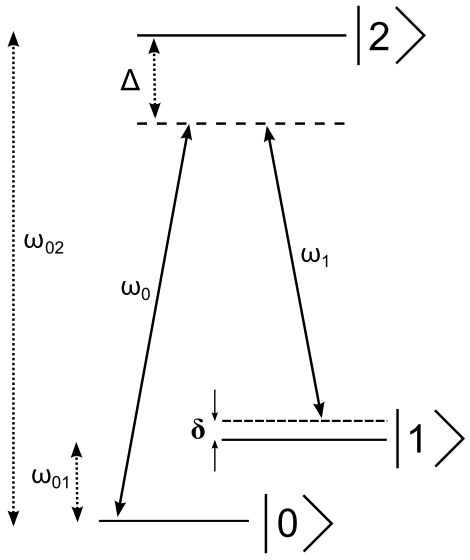

Figure 3.5: Atom-laser interaction model for Raman transitions.
An auxiliary third level $|2\rangle$ is virtually excited by two laser beams to coherently drive population between the qubit states.

ion, the unperturbed Hamiltonian is simply

$$H_0 = \omega_{01}|1\rangle\langle 1| + \omega_{02}|2\rangle\langle 2| = \begin{pmatrix} 0 & 0 & 0 \\ 0 & \omega_{01} & 0 \\ 0 & 0 & \omega_{02} \end{pmatrix}$$

where for convenience we set $\hbar = 1$ and $|0\rangle$ defines the zero energy point. Define the dipole moment operator matrix elements $\mu_{20} \equiv \langle 2|\hat{\mu}|0\rangle$, $\mu_{21} \equiv \langle 2|\hat{\mu}|1\rangle$, so that the dipole moment operator can be expressed as

$$\hat{\mu} = \mu_{20}|2\rangle\langle 0| + \mu_{02}|0\rangle\langle 2| + \mu_{21}|2\rangle\langle 1| + \mu_{12}|1\rangle\langle 2| = \begin{pmatrix} 0 & 0 & \mu_{02} \\ 0 & 0 & \mu_{12} \\ \mu_{20} & \mu_{21} & 0 \end{pmatrix}$$

The interaction part of the Hamiltonian is given by

$$H_I = -\hat{\mu} \cdot \mathbf{E} = \begin{pmatrix} 0 & 0 & \mu_{02} \cdot \mathbf{E} \\ 0 & 0 & \mu_{12} \cdot \mathbf{E} \\ \mu_{20} \cdot \mathbf{E} & \mu_{21} \cdot \mathbf{E} & 0 \end{pmatrix}$$

bringing the full spin part of the Hamiltonian to

$$H = H_0 + H_I = \begin{pmatrix} 0 & 0 & \mu_{02} \cdot \mathbf{E} \\ 0 & \omega_{01} & \mu_{12} \cdot \mathbf{E} \\ \mu_{20} \cdot \mathbf{E} & \mu_{21} \cdot \mathbf{E} & \omega_{02} \end{pmatrix}.$$

The Hamiltonian can be transformed to one in a rotating frame, H_{RF}, via unitary operator U according to

$$H_{RF} = U^{\dagger} H U - i U^{\dagger} \frac{\partial}{\partial t} U.$$

If U is given by

$$U = \begin{pmatrix} 1 & 0 & 0 \\ 0 & e^{-i\omega_{01}t} & 0 \\ 0 & 0 & e^{-i\omega_{0}t} \end{pmatrix},$$

$$U^\dagger H U = \begin{pmatrix} 1 & 0 & 0 \\ 0 & e^{i\omega_{01}t} & 0 \\ 0 & 0 & e^{i\omega_0 t} \end{pmatrix} \begin{pmatrix} 0 & 0 & \mu_{02}\cdot\mathbf{E} \\ 0 & \omega_{01} & \mu_{12}\cdot\mathbf{E} \\ \mu_{20}\cdot\mathbf{E} & \mu_{21}\cdot\mathbf{E} & \omega_{02} \end{pmatrix} \begin{pmatrix} 1 & 0 & 0 \\ 0 & e^{-i\omega_{01}t} & 0 \\ 0 & 0 & e^{-i\omega_0 t} \end{pmatrix}$$

$$= \begin{pmatrix} 0 & 0 & e^{-i\omega_0 t}\mu_{02}\cdot\mathbf{E} \\ 0 & \omega_{01} & e^{-i(\omega_0-\omega_{01})t}\mu_{12}\cdot\mathbf{E} \\ e^{i\omega_0 t}\mu_{20}\cdot\mathbf{E} & e^{i(\omega_0-\omega_{01})t}\mu_{21}\cdot\mathbf{E} & \omega_{02} \end{pmatrix} \text{ and}$$

$$-iU^\dagger \frac{\partial}{\partial t} U = \begin{pmatrix} 0 & 0 & 0 \\ 0 & \omega_{01} & 0 \\ 0 & 0 & \omega_0 \end{pmatrix}$$

so the Hamiltonian in the rotated frame is

$$H_{RF} = \begin{pmatrix} 0 & 0 & e^{-i\omega_0 t}\mu_{02}\cdot\mathbf{E} \\ 0 & \omega_{01} & e^{-i(\omega_0-\omega_{01})t}\mu_{12}\cdot\mathbf{E} \\ e^{i\omega_0 t}\mu_{20}\cdot\mathbf{E} & e^{i(\omega_0-\omega_{01})t}\mu_{21}\cdot\mathbf{E} & \omega_{02} \end{pmatrix} - \begin{pmatrix} 0 & 0 & 0 \\ 0 & \omega_{01} & 0 \\ 0 & 0 & \omega_0 \end{pmatrix}$$

$$= \begin{pmatrix} 0 & 0 & e^{-i\omega_0 t}\mu_{02}\cdot\mathbf{E} \\ 0 & 0 & e^{-i(\omega_0-\omega_{01})t}\mu_{12}\cdot\mathbf{E} \\ e^{i\omega_0 t}\mu_{20}\cdot\mathbf{E} & e^{i(\omega_0-\omega_{01})t}\mu_{21}\cdot\mathbf{E} & \omega_{02}-\omega_0 \end{pmatrix}$$

Evaluate elements $H_{RF}^{(0,2)}$ and $H_{RF}^{(1,2)}$,

$$e^{-i\omega_0 t}\mu_{02}\cdot\mathbf{E} = g_{02,0}\left(1+e^{-i2\omega_0 t}\right) + g_{02,1}\left(e^{i(\omega_1-\omega_0)t} + e^{-i(\omega_1+\omega_0)t}\right)$$

$$e^{-i(\omega_0-\omega_{01})t}\mu_{12}\cdot\mathbf{E} = g_{12,0}\left(e^{i\omega_{01}t} + e^{-i(2\omega_0-\omega_{01})t}\right) + g_{12,1}\left(e^{i((\omega_1-\omega_0)+\omega_{01})t} + e^{-i((\omega_1+\omega_0)-\omega_{01})t}\right),$$

where the coupling parameters $g_{ij,k}$ will be explicitly defined after a few more steps. Apply the rotating wave approximation by discarding terms oscillating at frequencies $\omega_0 + \omega_1$ and $2\omega_0$ so that H_{RF} becomes $\mathcal{H}_I$, where

$$\mathcal{H}_I \equiv \begin{pmatrix} 0 & 0 & g_{02,0} + g_{02,1}e^{i(\omega_1-\omega_0)t} \\ 0 & 0 & 2g_{12,0}e^{i\omega_{01}t} + g_{12,1}e^{i(\omega_1-\omega_0+\omega_{01})t} \\ c.c. & c.c. & \Delta \end{pmatrix}.$$

Identify the detunings $\omega_1 - \omega_0 = \omega_{01} + \delta$ so that $\mathcal{H}_I$ becomes

$$\mathcal{H}_I = \begin{pmatrix} 0 & 0 & g_{02,0} + g_{02,1}e^{i\omega_{01}t}e^{i\delta t} \\ 0 & 0 & g_{12,0}e^{i\omega_{01}t} + g_{12,1}e^{-i\delta t} \\ c.c. & c.c. & \Delta \end{pmatrix}$$

$$= \Delta|2\rangle\langle 2| + \left[\left(g_{02,0} + g_{02,1}e^{i\omega_{01}t}e^{i\delta t}\right)|0\rangle\langle 2| + h.c.\right] + \left[\left(g_{12,0}e^{i\omega_{01}t} + g_{12,1}e^{-i\delta t}\right)|1\rangle\langle 2| + h.c.\right]$$

The far-off-resonant couplings $g_{02,1}$ and $g_{12,0}$ can be discarded, allowing us to simplify the notation by defining the remaining complex Rabi parameters:

$$g_{02,0} = \frac{E_0}{2\hbar}\langle 0|\hat{\mu}\cdot\vec{\epsilon}_0|2\rangle e^{-i\phi_0} \equiv g_0 e^{-i\phi_0}$$
$$g_{12,1} = \frac{E_1}{2\hbar}\langle 1|\hat{\mu}\cdot\vec{\epsilon}_1|2\rangle e^{-i\phi_1} \equiv g_1 e^{-i\phi_1}.$$

If we transform to a frame rotating at the qubit frequency using $|0\rangle \to |0\rangle$, $|1\rangle \to e^{2i\delta t}|1\rangle$,

and $|2\rangle \rightarrow e^{i\delta t}|2\rangle$ the interaction Hamiltonian becomes

$$\mathcal{H}_I = \Delta|2\rangle\langle 2| + g_0\left[e^{-i(\delta t+\phi_0)}|0\rangle\langle 2| + h.c.\right] + g_1\left[e^{-i\phi_1}|1\rangle\langle 2| + h.c.\right]$$

The auxiliary state $|2\rangle$ can be adiabatically eliminated in the limit where negligible population accumulates there. The Schrödinger equation is

$$\begin{pmatrix} \dot{c}_0 \\ \dot{c}_1 \\ \dot{c}_2 \end{pmatrix} = \begin{pmatrix} 0 & 0 & g_0 e^{-i(\delta t+\phi_0)} \\ 0 & 0 & g_1 e^{-i\phi_1} \\ g_0 e^{i(\delta t+\phi_0)} & g_1 e^{i\phi_1} & \Delta \end{pmatrix} \begin{pmatrix} c_0 \\ c_1 \\ c_2 \end{pmatrix}$$

By transforming with $c_2 \rightarrow e^{i\Delta t}c_2$ and approximating $\dot{c}_2 \simeq 0$ it becomes

$$\begin{pmatrix} \dot{c}_0 \\ \dot{c}_1 \\ 0 \end{pmatrix} = \begin{pmatrix} 0 & 0 & g_0 e^{-i(\phi_0+(\delta-\Delta)t)} \\ 0 & 0 & g_1 e^{-i(\phi_1-\Delta t)} \\ g_0 e^{i(\phi_0+(+\delta)t)} & g_1 e^{i\phi_1} & \Delta e^{i\Delta t} \end{pmatrix} \begin{pmatrix} c_0 \\ c_1 \\ c_2 \end{pmatrix}$$

By solving for c_2 and substituting into the equations for c_0, c_1 to eliminate the auxilliary state from the problem, it becomes

$$\begin{pmatrix} \dot{c}_0 \\ \dot{c}_1 \end{pmatrix} = \begin{pmatrix} -\frac{g_0^2}{\Delta} & -\frac{g_0 g_1}{\Delta} e^{-i(\delta t+\Delta\phi)} \\ -\frac{g_1 g_0}{\Delta} e^{i(\delta t+\Delta\phi)} & -\frac{g_1^2}{\Delta} \end{pmatrix} \begin{pmatrix} c_0 \\ c_1 \end{pmatrix}$$

where $\Delta\phi \equiv \phi_1 - \phi_0$. Hence, the interaction Hamiltonian becomes

$$\mathcal{H}_I = \frac{\hbar\Omega}{2}\left(e^{-i(\delta t+\Delta\phi)}|1\rangle\langle 0| + h.c.\right) + \frac{\hbar\chi_0}{2}|0\rangle\langle 0| + \frac{\hbar\chi_1}{2}|1\rangle\langle 1|$$

where the "base Rabi frequency" coupling the qubit states is given by $\Omega \equiv g_1 g_0/2\Delta$ and $\chi_j \equiv g_j^2/2\Delta$ is the light shift (or AC Stark shift) on state $|j\rangle$. (The light shifts actually have contributions from both Raman beams, but we have already assumed that $g_{02,1}$ and $g_{12,0}$ are small.) Finally, by defining $\chi_\pm \equiv (\chi_1 \pm \chi_0)/2$, $\mathcal{H}_I$ can be recast in spin operator form

$$\mathcal{H}_I = \frac{\hbar\Omega}{2}\left(\hat{\sigma}_+ e^{-i(\delta t-\Delta\phi)} + \hat{\sigma}_- e^{i(\delta t-\Delta\phi)}\right) + \frac{\hbar\chi_-}{2}\hat{\sigma}_z$$

where the common light shift term proportional to $(\chi_1 + \chi_0)$ is discarded because it does not influence the spin system dynamics. Transform to a frame rotating at the new shifted resonance frequency $\omega'_{01} \equiv \omega_{01} + \chi_-$ and define $\mu \equiv \omega_0 - \omega_1 - \omega'_{01}$:

$$\mathcal{H}_I = \frac{\hbar\Omega}{2}\left(\hat{\sigma}_+ e^{-i(\mu t-\Delta\phi)} + \hat{\sigma}_- e^{i(\mu t-\Delta\phi)}\right) \tag{3.22}$$

This Hamiltonian has the same form as that derived for the microwave field interaction; hence, the Raman transitions can be used to perform qubit rotations exactly as in Eqn. 3.10.

To discover how the Raman transition also couples the spin to the motion, we will now reinsert the spatial part of the optical fields. For the same reason the relevant global phase became the difference phase between the Raman beams, $\Delta\phi$,

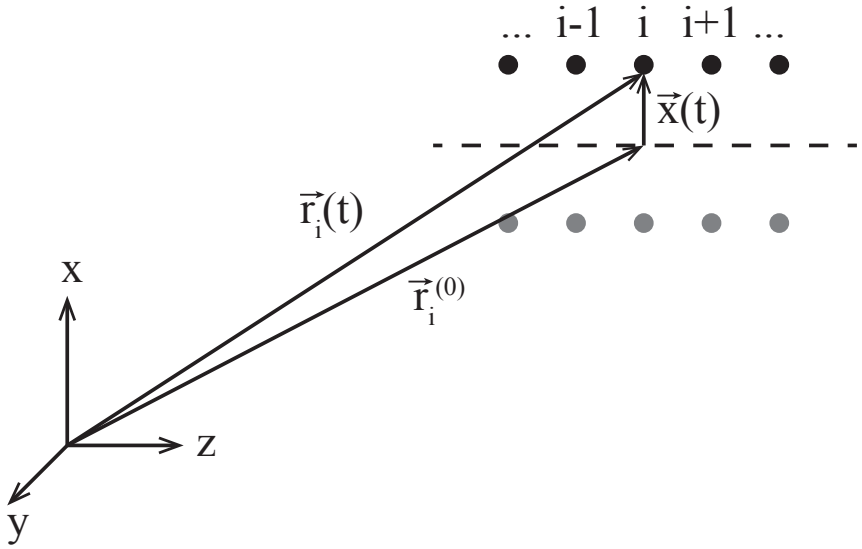

Figure 3.6: Coordinate system for the position $\vec{r}_i(t)$ of ion i.
The ion position $\vec{x}_i(t)$ oscillates about an equilibrium position denoted by the dashed line. This time-dependent position operator can be expressed in terms of the collective motional mode raising and lowering operators.

the relevant spatial term in the exponentials becomes $\Delta\mathbf{k}\cdot\mathbf{r}_i$ for ion i. The ion position $\mathbf{r}_i(t) = \mathbf{r}_i^{(0)} + \mathbf{x}_i(t)$, as shown in Fig. 3.6, so $\Delta\mathbf{k}\cdot\mathbf{r}_i = \Delta k r_i^{(0)} + \Delta\mathbf{k}\cdot\mathbf{x}_i(t)$, where $\Delta k r_i^{(0)}$ simply contributes an additional phase specific to ion i. In the regime where micromotion sidebands are not driven and the trap q_r parameter is small (Eq. 2.14), the operator $\mathbf{x}_i(t)$ can be written in terms of the raising and lowering operators of the normal modes of motion as

$$\mathbf{x}_j(t) = \sum_{k=1}^{N} b_{k,j} x_{0,k} \left(\hat{a}_k e^{-i\omega_k t} + \hat{a}_k^\dagger e^{i\omega_k t}\right)$$

where $b_{k,j}$ is the normal mode coupling parameter from Sec. 3.2.1 and $x_{0,k} \equiv \sqrt{\hbar/2m\omega_k}$. This expression tacitly derives from a transformation to the frame of the motional frequencies where the unperturbed Hamiltonian now includes the motional

terms:

$$H_0 = \sum_{j=1}^{N} \frac{\hbar\omega_{01}}{2}\hat{\sigma}_z^{(j)} + \sum_{k=1}^{N} \hbar\omega_k \hat{a}_k^\dagger \hat{a}_k$$

The dot product thus becomes

$$\Delta\mathbf{k}\cdot\mathbf{x}_j(t) = \sum_{k=1}^{N} \eta_{k,j}\left(\hat{a}_k e^{-i\omega_k t} + \hat{a}_k^\dagger e^{i\omega_k t}\right)$$

where $\eta_{k,j} \equiv \Delta k_x b_{k,j}\sqrt{\frac{\hbar}{2m\omega_k}}$ is the coupling parameter between ion j and mode k in the interaction. Using these equations to include the motional terms, the interaction Hamiltonian is

$$\begin{aligned}\mathcal{H}_I &= \sum_{j=1}^{N} \frac{\hbar\Omega_j}{2}\left(\hat{\sigma}_+^{(j)} e^{-i(\mu t - \Delta\phi + \Delta\mathbf{k}\cdot\mathbf{r}_j(t))} + \hat{\sigma}_-^{(j)} e^{i(\mu t - \Delta\phi + \Delta\mathbf{k}\cdot\mathbf{r}_j(t))}\right) \\ &= \sum_{j,k=1}^{N} \frac{\hbar\Omega_j}{2}\left(\hat{\sigma}_+^{(j)} e^{-i\eta_{k,j}(\hat{a}e^{-i\omega_k t} + \hat{a}^\dagger e^{i\omega_k t})} e^{-i(\mu t - \Delta\phi + \Delta k r_j^{(0)})} + h.c\right)\end{aligned} \tag{3.23}$$

Unless specifically noted otherwise, the summation symbols with multiple indices denote *multiple uncoupled* sums. The coupling parameter η characterizes the relative spread of the ion wave packet compared to the wavelength of the radiation as well as the strength of the spin-motion coupling. For a particular mode k, the common part of η is the Lamb-Dicke parameter $\eta_0 \equiv \Delta k_x\sqrt{\frac{\hbar}{2m\omega_k}}$. This parameter cannot be too small, or else there will be insufficient coupling. For counter-propagating waves, $\Delta k = 2k = 4\pi/\lambda$, so an ultraviolet laser wavelength of 355 nm has $\sim$70000 times the coupling strength of resonant microwaves. At the same time, η_0 cannot be too large. In the so-called Lamb-Dicke limit, $\eta^2(n+1) \ll 1$ for vibrational level n such

that the optical phase is nearly constant over the ion excursions. In this regime, the exponential term can be expanded to first order in η simplifying the expression to

$$\begin{aligned}\mathcal{H}_I &= \sum_{j,k=1}^{N} \frac{\hbar\Omega}{2}\left(\hat{\sigma}_+^{(j)}\left[1 - i\eta_{k,j}(\hat{a}e^{-i\omega_k t} + \hat{a}^\dagger e^{i\omega_k t})\right] e^{-i(\mu t+\phi_j)} + h.c\right) \\ &= \sum_{j,k=1}^{N} \frac{\hbar\Omega_j}{2}\hat{\sigma}_+^{(j)}\left[e^{-i(\mu t+\phi_j)} - i\eta_{k,j}\left(\hat{a}e^{-i((\omega_k+\mu)t+\phi_j)} + \hat{a}^\dagger e^{i((\omega_k-\mu)t-\phi_j)}\right)\right] + h.c\end{aligned} \tag{3.24}$$

where the optical phase term at each ion position is $\phi_j \equiv \Delta\phi + \Delta k r_j^{(0)}$. If μ is $0, -\omega_k$, or $+\omega_k$, the Raman beams will drive a carrier, red sideband, or blue sideband transition, respectively, for mode k. In each case, two of the exponential terms in $\mathcal{H}_I$ reduce to unity, and the other four terms can be discarded using another rotating wave approximation as long as the interaction time is long compared to the trap secular period ($2\pi/\omega_x$). This situation is called the resolved sideband limit. In this regime, the sideband transitions are explicitly calculated very similarly to the simple two-level system in Sec. 3.1, with the difference being that the coupled states include vibrational levels $|n\rangle$ of a particular mode. The relevant state vector becomes

$$|\psi\rangle = c_{0,n}|0,n\rangle + c_{1,n}|1,n\rangle \tag{3.25}$$

which changes the matrix element in the interaction Hamiltonian to $\langle 1,n'|\mathcal{H}_I|0,n\rangle$ that now includes a Debye-Waller factor [45],

$$D_{n',n} = \left|\langle n|e^{i\eta(\hat{a}+\hat{a}^\dagger)}|n'\rangle\right|.$$

This factor adjusts the original Rabi rate Ω between the qubit levels depending on which vibrational transition is also driven. The corresponding sideband coupling strength is given by $\Omega_{n',n} = D_{n',n}\Omega$. This is the rate at which the state coherently oscillates between $|0, n\rangle$ and $|1, n'\rangle$. In the Lamb-Dicke limit, the first red and blue sidebands have Rabi frequencies $\Omega_{n,n-1} = \eta\sqrt{n}\Omega$ and $\Omega_{n,n+1} = \eta\sqrt{n+1}\Omega$. The modified Rabi rates are taken into account when we Raman sideband cool, where the red sideband π pulse durations are lengthened with each successive cycle to achieve efficient population transfer [45].

Thus far it is clear how tuning the beat note between the Raman beams can either drive qubit rotations alone or flip the qubit while adding or removing a phonon of energy to a mode of the collective motion. The final piece of the entangling gate puzzle is the application of both a red and a blue sideband simultaneously. Returning to Eq. 3.23 for the Hamiltonian prior to the applying any approximations, apply two beams (called the "red and blue sidebands") instead of the single beam depicted in Fig. 3.5. The forms of the optical fields are similar to Eq. 3.21, but the red (blue) sideband has frequency $\omega_r = \omega_0 - \omega_{01} + \mu$ ($\omega_b = \omega_0 - \omega_{01} - \mu$) and phase difference ϕ_r (ϕ_b) with the non-copropagating Raman beam. In our experiment, the sideband beams are copropagating, so the signs of the Δk terms are the same. Letting $\beta_j \equiv \Delta\mathbf{k}\cdot\mathbf{x}_i(t)$ for convenience, the resulting Mølmer-Sørensen

type interaction [61, 62] is

$$\begin{aligned}
\mathcal{H}_{MS} &= \sum_{j=1}^{N} \frac{\hbar\Omega_j}{2} \left[\left(\hat{\sigma}_+^{(j)} e^{-i(\mu t - \phi_r + \Delta\mathbf{k}\cdot\mathbf{r}_j(t))} + h.c. \right) + \left(\hat{\sigma}_+^{(j)} e^{-i(-\mu t - \phi_b + \Delta\mathbf{k}\cdot\mathbf{r}_j(t))} + h.c. \right) \right] \\
&= \sum_{j=1}^{N} \frac{\hbar\Omega_j}{2} \left[\hat{\sigma}_+^{(j)} \left(e^{-i(\mu t - \phi_j^M - \phi_j^S + \beta_j)} + e^{i(\mu t + \phi_j^S - \phi_j^M - \beta_j)} \right) + h.c. \right] \\
&= \sum_{j=1}^{N} \frac{\hbar\Omega_j}{2} \left[\hat{\sigma}_+^{(j)} e^{i(\phi_j^S - \beta_j)} \left(e^{-i(\mu t - \phi_j^M)} + e^{i(\mu t - \phi_j^M)} \right) + h.c. \right] \\
&= \sum_{j=1}^{N} \frac{\hbar\Omega_j}{2} \cos\left(\mu t - \phi_j^M\right) \left[\hat{\sigma}_+^{(j)} e^{i(\phi_j^S - \beta_j)} + h.c. \right]
\end{aligned} \tag{3.26}$$

where $\phi_j^S \equiv (\phi_j^r + \phi_j^b)/2$ and $\phi_j^M \equiv (\phi_j^r - \phi_j^b)/2$ are the spin and motion combinations of the red and blue sideband optical phases that include the individual ion position phase terms $\Delta k r_j^{(0)}$. Returning to the Lamb-Dicke regime, the terms $e^{\pm i\beta_j} \approx (1 \pm i\beta_j)$, and the Hamiltonian becomes

$$\begin{aligned}
\mathcal{H}_{MS} =& \sum_{j=1}^{N} \hbar\Omega_j \cos\left(\mu t - \phi_j^M\right) \Big[\left(\hat{\sigma}_+^{(j)} e^{i\phi_j^S} + \hat{\sigma}_-^{(j)} e^{-i\phi_j^S} \right) \\
&+ \left(\hat{\sigma}_+^{(j)} e^{i(\phi_j^S + \pi/2)} + \hat{\sigma}_-^{(j)} e^{-i(\phi_j^S + \pi/2)} \right) \beta_j \Big] \\
=& \sum_{j=1}^{N} \hbar\Omega_j \cos\left(\mu t - \phi_j^M\right) \hat{\sigma}_{\phi_\perp}^{(j)} \\
&+ \sum_{j,k=1}^{N} \hbar\eta_{k,j}\Omega_j \cos\left(\mu t - \phi_j^M\right) \left(\hat{a} e^{-i\omega_k t} + \hat{a}^\dagger e^{i\omega_k t} \right) \hat{\sigma}_\phi^{(j)}
\end{aligned} \tag{3.27}$$

where the spin operator $\hat{\sigma}_\phi^{(j)} = \cos\phi_j^S \hat{\sigma}_x^{(j)} + \sin\phi_j^S \hat{\sigma}_y^{(j)}$ rotates the qubit j about an arbitrary axis in the Bloch sphere equatorial plane specified by ϕ_j^S, and $\hat{\sigma}_{\phi_\perp}^{(j)}$ rotates the same qubit about the perpendicular axis. This $\hat{\sigma}_{\phi_\perp}^{(j)}$ term drives carrier transitions so weakly that it is usually ignored safely. However, if Ω/μ were to grow too large,

the effects on the dynamics would cease to be negligible. In our experiments we can neglect the term, resulting in a final entangling interaction Hamiltonian

$$\mathcal{H}_{MS} = \sum_{j,k=1}^{N} \hbar\eta_{k,j}\Omega_j \cos\left(\mu t - \phi_j^M\right)\left(\hat{a}e^{-i\omega_k t} + \hat{a}^\dagger e^{i\omega_k t}\right)\hat{\sigma}_\phi^{(j)} \tag{3.28}$$

The evolution operator for the entangling interaction is obtained by applying Magnus' formula. Starting from time zero, the evolution operator is given by

$$U_g(\tau) = \exp\left[-\frac{i}{\hbar}\int_0^\tau dt\mathcal{H}_{\rm MS} - \frac{1}{2\hbar}\int_0^\tau dt_2\int_0^{t_2} dt_1\left[\mathcal{H}_{\rm MS}(t_2), \mathcal{H}_{\rm MS}(t_1)\right] + \cdots\right] \tag{3.29}$$

The first term is a single integral equal to

$$\begin{aligned}
-\frac{i}{\hbar}\int_0^\tau dt\mathcal{H}_{\rm MS} =& -i\sum_{j,k=1}^{N}\eta_{k,j}\Big[\hat{a}\int_0^\tau \Omega_j\cos\left(\mu t - \phi_j^M\right)e^{-i\omega_k t}dt \\
&+ \hat{a}^\dagger\int_0^\tau \Omega_j\cos\left(\mu t - \phi_j^M\right)e^{i\omega_k t}dt\Big]\hat{\sigma}_\phi^{(j)} \\
=& \sum_{j,k=1}^{N}\left(\alpha_{j,k}(\tau)\hat{a}^\dagger + \alpha_{j,k}^*(\tau)\hat{a}\right)\hat{\sigma}_\phi^{(j)}
\end{aligned}$$

where the expression for $\alpha_{j,k}(\tau)$ is defined as

$$\alpha_{j,k}(\tau) \equiv -\eta_{k,j}\int_0^\tau \Omega_j(t)\sin\left(\mu t - \phi_j^M\right)e^{i\omega_k t}dt \tag{3.30}$$

The next term in the expansion is

$$
\begin{aligned}
&-\frac{1}{2\hbar}\int_0^\tau dt_2 \int_0^{t_2} dt_1 \left[\mathcal{H}_{\mathrm{MS}}(t_2), \mathcal{H}_{\mathrm{MS}}(t_1)\right] \\
&= -\sum_{m,n,k=1}^{N} \frac{\eta_{k,m}\eta_{k,n}}{2}\int_0^\tau dt_2 \int_0^{t_2} dt_1 \Omega_m(t_2)\Omega_n(t_1)\cos\left(\mu t_2 + \phi_j^M\right)\cos\left(\mu t_1 + \phi_j^M\right)\times \\
&\qquad\qquad \left([\hat{a_k}, \hat{a_k}^\dagger]e^{i\omega_k(t_2-t_1)} - [\hat{a_k}^\dagger, \hat{a_k}]e^{-i\omega_k(t_2-t_1)}\right)\left(2\hat{\sigma}_\phi^{(m)}\hat{\sigma}_\phi^{(n)}\right) \\
&= -2i\sum_{m,n,k=1}^{N} \eta_{k,m}\eta_{k,n}\int_0^\tau dt_2 \int_0^{t_2} dt_1 \Omega_m(t_2)\Omega_n(t_1)\sin\omega_k(t_2-t_1)\times \\
&\qquad\qquad \cos\left(\mu t_2 + \phi_j^M\right)\cos\left(\mu t_1 + \phi_j^M\right)\hat{\sigma}_\phi^{(m)}\hat{\sigma}_\phi^{(n)}
\end{aligned}
$$

Combining these terms, the evolution operator is finally given by

$$
U_g(\tau) = \exp\left[\sum_{m,k=1}^{N}\left(\alpha_{m,k}(\tau)\hat{a}_k^\dagger - \alpha_{m,k}^*(\tau)\hat{a}_k\right)\hat{\sigma}_\phi^{(m)} + i\sum_{m,n=1}^{N}\chi_{m,n}(\tau)\hat{\sigma}_\phi^{(m)}\hat{\sigma}_\phi^{(n)}\right] \tag{3.31}
$$

where $\chi_{m,n}(t)$ is defined as

$$
\begin{aligned}
\chi_{m,n}(\tau) \equiv \sum_{k=1}^{N}\eta_{k,m}\eta_{k,n}\int_0^\tau\int_0^{t_2} dt_2 dt_1 \Big(&\Omega_m(t_2)\Omega_n(t_1)\sin\omega_k(t_2-t_1)\times \\
&\sin\left(\mu t_2 + \phi_j^M\right)\sin\left(\mu t_1 + \phi_j^M\right)\Big)
\end{aligned} \tag{3.32}
$$

where $\Delta\phi^M \equiv \phi_m^M - \phi_n^M$. (The negative cosine product was converted to a positive product of sines by expressing the -1 factor as $e^{-i\pi/2}e^{-i\pi/2}$, casting the cosines in exponential form, and using some algebra.)

It is instructive to consider the overall structure of this interaction. The evolution of the spin and motion state has a helpful geometric visualization that provides

some physical intuition for the entangling operation. It is also useful for the more complicated evolution when pulse shaping is added in the next chapter. The two terms in the exponential neatly partition the evolution into the spin-dependent trajectories in phase space (first term) and an accumulating geometric phase $\chi_{m,n}(t)$ between pairs of qubits that is proportional to the area enclosed by the associated trajectories (second term). The motional part of the first term has exactly the form of the displacement operator $\hat{\mathcal{D}}(\alpha) = \exp\left(\alpha(t)\hat{a}^\dagger - \alpha^*(t)\hat{a}\right)$. The action of $\hat{\mathcal{D}}(\alpha)$ on a coherent state of motion $|\beta\rangle_C$,

$$|\beta\rangle_C \equiv e^{-|\beta|^2/2} \sum_{n=0}^{\infty} \frac{\beta^n}{\sqrt{n!}} |n\rangle_F$$

where the coherent state is defined in terms of the Fock state basis $|n\rangle_F$, is given by

$$\hat{\mathcal{D}}(\alpha)|\beta\rangle_C = \hat{\mathcal{D}}(\alpha+\beta)e^{i\mathrm{Im}(\alpha\beta^*)}.$$

Starting from the motional ground state, where the coherent and Fock state bases intersect ($|0\rangle_C = |0\rangle_F$), the resulting coherent state $|\alpha\rangle_C = \hat{\mathcal{D}}(\alpha)|0\rangle_C$ follows a trajectory in phase space $\alpha(t) = (1/2x_0)\left(x(t) + ip(t)/m\omega\right)$, whose real and imaginary components specify the position and momentum coordinates of the ion wave packet. The actual expression for $\alpha(t)$ given by Eq. 3.30 denotes the carrier Rabi rate $\Omega_j(t)$ as a function of time. The conventional Mølmer-Sørensen interaction assumes that $\Omega_j(t) = \Omega_j$ is a constant. In Ch. 4 we will discover the limitations of this assumption and how allowing it to vary in time can significantly improve the entangling scheme.

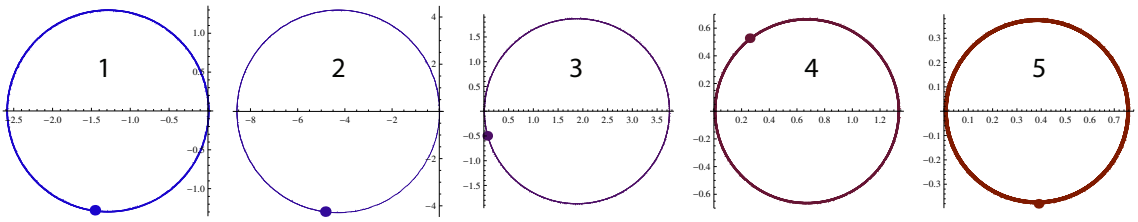

Figure 3.7: Phase space trajectories for the first ion in a chain of five (arb units). The CM frequency is 2.591 MHz and the detuning μ=2.564 MHz with an interaction time τ =200 µs. The dots represent the final position of the wave packet. Only one of the two trajectories associated with the $\hat{\sigma}_\phi$ eigenstates is plotted. The modes closer to μ execute larger orbits, so the fine structure of the path is only evident in the evolution of the fifth mode. In this example, the entangling interaction would not perform an acceptable gate because the trajectories do not return to the origin.

For the remainder of this chapter, however, we will restrict it to a constant value.

In this case, the integral can be immediately solved to give

$$\begin{aligned}\alpha_{k,j}(\tau) =& \frac{\eta_{k,j}\Omega_j}{\mu^2-\omega_k^2}\Big[e^{i\omega_k\tau}\left(\mu\cos\left(\mu\tau-\phi_j^M\right)-i\omega_k\sin\left(\mu\tau-\phi_j^M\right)\right)\\ &-\left(\mu\cos\phi_j^M+i\omega_k\sin\phi_j^M\right)\Big]\end{aligned} \tag{3.33}$$

Under this harmonic force of constant amplitude, the overall shape of the trajectory is circular, with a radius proportional to $\eta_{k,m}\Omega_m/\delta_k$. On top of the circles are smaller circular excursions. Figure 3.7 illustrates these trajectories for an ion participating in the five modes of a chain of five ions. When $\delta_k \ll \mu+\omega_k$, the trajectory reduces to a perfect circle (let $\phi_j^M \to 0$)

$$\alpha_{k,j}(\tau) \approx \frac{\eta_{k,j}\Omega_j}{2}\left(\frac{e^{-i\delta_k\tau}-1}{\delta_k}\right) \tag{3.34}$$

The spin-dependence of the force propelling the ions along these trajectories

comes from the presence of the $\hat{\sigma}_\phi$ operator. The eigenstates of this operator are $|\pm\rangle_\phi = \left(\pm ie^{-i\phi^S}|0\rangle_z + |1\rangle_z\right)/\sqrt{2}$ with eigenvalues ± 1; hence, if the qubit is in a superposition of these eigenstates, it will simultaneously execute two equal but opposite trajectories in phase space. The resulting entanglement between the qubit states and the collective motional modes is the underlying mechanism for the entanglement between the qubits themselves, which brings us to the second term in the evolution operator. The motional part of this term, $\chi_{m,n}(t)$, keeps track of the accumulating area encompassed by the phase space trajectories. This area is proportional to a "geometric phase" acquired by each qubit, which directly generates a spin-spin interaction via the $\hat{\sigma}_\phi^{(m)}\hat{\sigma}_\phi^{(n)}$ operator.

To perform a useful entangling gate, the evolution described so far must be controlled precisely to satisfy two criteria [61–64]:

- **The value of $\chi_{m,n}$ must be $\pi/4$.**
- **The qubits must disentangle from the motion by the end of the interaction.** Since we do not measure the motional state of the ions, that information is lost and is therefore a source of decoherence. More formally, the full state density matrix for the system includes both the qubit and motional states. We trace over the motional part of this density matrix to account for our ignorance, and by doing so, any extant spin-motion entanglement contributes to a statistical mixture of states that degrades the desired spin-spin entanglement.

Consider the simplest case of two ions. When both of these criteria are satisfied,

the resulting evolution operator becomes

$$U_g = \exp\left[i\frac{\pi}{4}\hat{\sigma}_x^{(1)}\hat{\sigma}_x^{(2)}\right]. \tag{3.35}$$

In the $\hat{\sigma}_z$ basis, the gate in matrix form is

$$U_g = \frac{1}{\sqrt{2}}\begin{pmatrix} 1 & 0 & 0 & -i \\ 0 & 1 & -i & 0 \\ 0 & -i & 1 & 0 \\ -i & 0 & 0 & 1 \end{pmatrix} \tag{3.36}$$

and applying it to two qubits initialized to the $|0\rangle$ state yields

$$\begin{aligned} \rho_{final} &= U_g \cdot \rho_{initial} \cdot U_g^\dagger \\ &= U_g \cdot \begin{pmatrix} 1 & 0 & 0 & 0 \\ 0 & 0 & 0 & 0 \\ 0 & 0 & 0 & 0 \\ 0 & 0 & 0 & 0 \end{pmatrix} \cdot U_g^\dagger = \frac{1}{2}\begin{pmatrix} 1 & 0 & 0 & i \\ 0 & 0 & 0 & 0 \\ 0 & 0 & 0 & 0 \\ -i & 0 & 0 & 1 \end{pmatrix} \\ |\psi\rangle_{final} &= \frac{1}{\sqrt{2}}\left(|00\rangle - i|11\rangle\right) \end{aligned}$$

This is a Bell state: a pure, maximally entangled state between the two qubits.

In the derivation of the evolution operator above, the phases of the red and blue sidebands were meticulously tracked. In most situations these phases can actually be set to zero by definition, but there are subtleties involved in doing so. At the

beginning of the coherent evolution of the system, all of the ϕ_j^r and ϕ_j^b phases can be defined as zero, even if the absolute values of the optical phases at each ion are different. This is possible because the initial value of the individual qubit phases are arbitrary and hence the $\hat{\sigma}_\phi$ can be set without loss of generality to $\hat{\sigma}_x$ for each qubit. However, a subsequent gate pulse could apply sidebands with different optical phases, for example, either deliberately via the AOM phase or incidentally by shuttling the ions to new positions relative to a focused beam that has a non-uniform phase profile. In this case, one cannot redefine the phases to zero because the qubit phase is already defined relative to the initial phase. The consequence is that the $\hat{\sigma}_x$ operators become unique $\hat{\sigma}_{\phi_j}$ operators for each ion. Fortunately, the ϕ_j^M would typically remain zero because the red and blue sideband phases should normally shift by the same amount, even if in general this is not true. If a perfect entangling gate is performed, the phase space trajectories will close, so for nulling that term in the evolution operator it does not matter on what particular eigenbasis the spin-dependent force operates. However, the ϕ_j^S that specify the new eigenbases for each qubit get mapped onto the resulting entangled states depending on the initial state according to

$$
\begin{aligned}
|00\rangle &\rightarrow \frac{1}{\sqrt{2}}\left(|00\rangle - ie^{-i(\phi_1^S+\phi_2^S)}|11\rangle\right) \\
|01\rangle &\rightarrow \frac{1}{\sqrt{2}}\left(|01\rangle - i|10\rangle\right) \\
|10\rangle &\rightarrow \frac{1}{\sqrt{2}}\left(|10\rangle - i|01\rangle\right) \\
|11\rangle &\rightarrow \frac{1}{\sqrt{2}}\left(|00\rangle - ie^{i(\phi_1^S+\phi_2^S)}|11\rangle\right)
\end{aligned}
$$

In the next chapter, we will discuss how to determine the optimal two-qubit entangling gate parameters and how we assess the performance of the gate by analyzing the entanglement of the resulting state. The need for better control over the quantum system will become apparent, and we will discover how shaping the gate pulse can improve the gate performance and ultimately enable scalability for the scheme.

Chapter 4: Gate pulse shaping

Using the spin-dependent force derived in the previous chapter to successfully generate a proper entangling gate (Eq. 3.35) demands precise control over the gate parameters. This chapter explains what those parameters are, how we determine their optimal value, and how we assess the performance of the gate. In certain regimes of gate time and detuning when there are only a few ions in the chain, a constant laser pulse amplitude is sufficient to perform an excellent gate. In order for linear chains of trapped ions to be a scalable platform for quantum computation, however, the number of qubits in the register must increase significantly and the fidelity of quantum gates performed must approach a fault-tolerant threshold [12, 13]. Even a simplistic view of a quantum algorithm is enough to demonstrate the necessity of this; if each entangling gate fidelity is $\mathcal{F}$, and n gates compose an algorithm for some computation, then the overall fidelity of the operation will be proportional to $\mathcal{F}^n$. For a seemingly good fidelity of 99%, an algorithm of just 20 gates would have an overall fidelity of $0.99^{20} = 82\%$, which is unacceptable. As we will see in the next section, the limits on the gate fidelity stem from the fact that the number of motional modes involved in the interaction increases with the number of ions. This means that more and more phase space trajectories must be controlled,

and this requires more control parameters than a constant amplitude pulse allows. This limitation can be overcome by rudimentary pulse shaping. Partitioning the gate pulse into multiple segments with independent amplitudes provides the extra "control knobs" to engineer the trajectories. Depending on the number of segments composing the pulse, the criteria for a perfect gate (Sec. 3.2.2) specify a standard control problem, where an optimization algorithm is used to calculate the pulse shape that will generate the highest fidelity gate.

4.1 Theory

Before launching into the formal definition of the control problem, it is helpful to again consider the simplest case of an ion chain with only two qubits. In this case there are two motional modes involved: the CM and the tilt mode, where the ions move together (CM) or oppositely (tilt). The traditional thing to do is to choose a detuning nearly resonant with one of these modes such that the other mode is barely driven. For this example, we couple predominantly to the tilt mode by choosing $\delta_2 \ll \delta_1$. From the two trajectory equations given by Eq. 3.34, $\alpha_{1,j}(\tau)$ will be much closer to the origin than $\alpha_{2,j}(\tau)$ regardless of the gate time because the radius is $\propto 1/\delta_k$. That means we only need to worry about timing the gate to close $\alpha_{2,j}(\tau)$. Solving $e^{-i\delta_2\tau} - 1 = 0$, we get the gate times $\tau = m(2\pi/\delta_2)$, where m is an integer. Now that the phase space trajectories are approximately at the origin, the other criterion to satisfy is that the accrued geometric phase is $\chi_{1,2} = \pi/4$. It is clear from Eq. 3.32 that the only remaining free parameter is the product of the constant

coupling strengths Ω_j, which are directly proportional to the Raman beam intensity, or pulse amplitude. Adjusting this value to set the radius of the $\alpha_{2,j}(\tau)$ trajectory appropriately, the geometric phase criterion is satisfied. The result is a gate that can approach perfection in the limit that $\delta_2 \to 0$ and $\tau \to \infty$ (in increments of $2\pi/\delta_2$).

The two ion example is also useful for illustrating how commensurability of mode frequencies plays a fundamental role in the gate performance, because this is the only case where μ can be chosen such that both phase spaces close perfectly for a constant pulse amplitude. Define parameters r_T and r_C that specify the detuning in terms of the ratio of δ_1 to δ_2 such that

$$\mu = \omega_1 + r_C \left(\frac{\omega_1 - \omega_2}{r_T - r_C} \right). \tag{4.1}$$

As long as δ_1/δ_2 is an integer (equivalently, r_C/r_T is an integer), then the gate time chosen based on δ_2 in our example will always return $\alpha_{1,j}(\tau)$ to the origin as well. By detuning far away from both modes, the gate can be made much faster at the expense of an increase in the required pulse amplitude.

If we now consider just one additional ion in the chain, it is impossible to find a gate time commensurate with all three frequencies. This is because the eigenvalues of the A_{mn} matrix from Sec. 3.2.1 are now $\mathcal{A}+1/2-\{1,3,29/5\}/2$, yielding irrational mode frequency ratios due to the square root in Eq. 3.20. As more ions are added to the chain, the number of transverse modes increase linearly while their spacing does not. This results in increasingly worse gates as there is more and more residual

spin-motion entanglement, assuming of course that the optimal values of detuning and gate time are employed.

At this point, we must identify the equations to satisfy in order to perform a perfect gate for any number of ions. Throughout the following derivations we will assume that only two out of a chain of N ions are simultaneously illuminated by the Raman beams with equal intensity, such that $\Omega(t) \equiv \Omega_m(t) = \Omega_n(t)$ for illuminated ions m and n and $\Omega(t) = 0$ for the rest. Clearly, for a chain of N ions there are N trajectories for each of the two ions with independent real and imaginary components (corresponding to x and p coordinates) that must each equal zero at the end of the gate. Since the Rabi rates are equal, there are $2N$ equations to satisfy from the phase space closure criterion:

$$\begin{aligned} \int_0^\tau \Omega(t) \sin(\mu t) \cos(\omega_k t) &= 0 \\ \int_0^\tau \Omega(t) \sin(\mu t) \sin(\omega_k t) &= 0 \end{aligned} \tag{4.2}$$

There is one additional equation from the geometric phase term

$$\sum_{k=1}^{N} \eta_{k,m}\eta_{k,n} \int_0^\tau \int_0^{t_2} dt_2 dt_1 \Omega_m(t_2)\Omega_n(t_1) \sin\omega_k(t_2 - t_1) \sin(\mu t_2) \sin(\mu t_1) = \pi/4 \tag{4.3}$$

If we partition the gate pulse into P flat segments such that

$$\Omega(t) = \begin{cases} \Omega_1 & 0 \leq t < \tau/P \\ \Omega_2 & \tau/P \leq t < 2\tau/P \\ \vdots & \vdots \\ \Omega_P & (P-1)\tau/P \leq t < \tau \end{cases} \tag{4.4}$$

then we introduce P independent control parameters. Since the system of equations is linear in this parameter, we are guaranteed to find a unique solution to the set if $P = 2N + 1$. In this case the phase space closure criterion becomes

$$\begin{aligned} \alpha_{k,m}(\tau) &= -\sum_{p=1}^{P} \Omega_p \eta_{k,m} \int_{(p-1)\tau/P}^{p\tau/P} \sin(\mu t) e^{i\omega_k t} dt \\ &= \sum_{p=1}^{P} \Omega_p C_{k,p}^{m} \end{aligned}$$

where the coefficient $C_{k,p}^{m}$ is a number pre-calculated from measured mode frequencies and desired gate parameters μ and τ. Similarly, the geometric phase is given by

$$\chi_{m,n}(\tau) = \sum_{p=1}^{P} \sum_{p'=1}^{P} \Omega_p \Omega_{p'} D_{p,p'}$$

where the pre-calculated coefficients $D_{p,p'}$ are given by

$$D_{p,p'} \equiv \sum_{k=1}^{N} \int_{(p-1)\tau/P}^{p\tau/P} dt_2 \int_{(p'-1)\tau/P}^{p'\tau/P} dt_1 \eta_{k,m}\eta_{k,n} \sin\omega_k(t_2 - t_1) \sin\mu t_2 \sin\mu t_1$$

If we represent the pulse shape $\Omega(t)$ as a column vector $\mathbf{\Omega}$, the gate criteria can be written concisely as

$$\begin{pmatrix} \mathbf{C}^m \\ \\ \mathbf{C}^n \end{pmatrix} \mathbf{\Omega} = \mathbf{0} \tag{4.5}$$

$$\mathbf{\Omega}^T \mathbf{D} \mathbf{\Omega} = \pi/4 \tag{4.6}$$

which represents a linear system of equations in $\mathbf{\Omega}$. Defining the $\mathbf{C}$ coefficients in this way, in terms of the two ion indices instead of the real and imaginary parts of the $\alpha(\tau)$ equations as described above, appears to be misleading; however, from a numerical perspective the two approaches are equally valid since the real and imaginary components will vanish the same. It is important to note here that since the trajectory equations are linear, if $\mathbf{\Omega_0}$ is a solution, then so is $f\mathbf{\Omega_0}$, where f is an arbitrary scale factor. This means that as long as $\mathbf{\Omega_0}^T \mathbf{D} \mathbf{\Omega_0} \neq 0$, then $\mathbf{\Omega_0}$ can be scaled as necessary to ensure that the geometric phase equals $\pi/4$.

One of the important features of this scheme is how the detuning and gate time become arbitrary parameters. In our two ion example above, the gate time and detuning were interdependent. Shaping the pulses removes this dependency. Before we can appreciate the significance of this by comparing the performance of a

constant pulse versus a segmented pulse, we must quantify the performance of the gate. In the experiments detailed below, this is done not by analyzing the gate *per se*, but instead by measuring the fidelity of preparing the target maximally entangled Bell state. The fidelity $\mathcal{F}$ of preparing a state is given by the overlap of the actual state with the ideal final state. Since the actual final state will in general be a mixed state, it must be represented by a density matrix ρ_f, such that

$$\mathcal{F} \equiv \langle \psi_{ideal} | \rho_f | \psi_{ideal} \rangle \tag{4.7}$$

where the ideal final state is $|\psi\rangle_{ideal} = \frac{1}{\sqrt{2}}\left(|00\rangle - ie^{-i\phi_g}|11\rangle\right)$ for some gate phase $\phi_g = \phi_1^S + \phi_2^S$. Since we do not measure the motion, the final state ρ_f is actually a reduced density matrix. A theoretical expression for the gate fidelity is obtained by applying the gate operator $U_g(\tau)$ to the initial state $\rho_i = |\psi_i\rangle\langle\psi_i| \otimes_k \rho_k$, where the initialized spin state $|\psi_i\rangle = |00\rangle_z = \frac{1}{2}(|0\rangle_x + |1\rangle_x)_m \otimes (|0\rangle_x + |1\rangle_x)_n$ for the two target ions m and n and the initial motional state is assumed to be in a thermal distribution characterized by the distribution's average phonon number, $\bar{n}_k$, such that

$$\rho_k = \sum_{n=0}^{\infty} \left(\frac{n_k}{1-\bar{n}_k}\right)^{n_k} e^{-n_k \hbar\omega_k / k_B T} |n_k\rangle\langle n_k|$$

where the average energy in phonon mode k is $k_B T = \bar{n}_k \hbar\omega_k$. The other $N-2$ ions are also initialized to spin down, but for now they are assumed to stay in that state throughout the interaction. The resulting state is the reduced density matrix $\rho_f = \mathrm{Tr}_{\mathrm{motion}}\left[U_g(\tau)\rho_i U_g^\dagger(\tau)\right]$, where the motional states have been traced over. The

fidelity expression is then [63]

$$\mathcal{F} = \frac{1}{8}\left[2 + i\left(e^{-2i|\chi_{m,n}|} - e^{2i|\chi_{m,n}|}\right)(\Gamma_m + \Gamma_n) + \Gamma_+ + \Gamma_-\right] \tag{4.8}$$

where

$$\Gamma_{m(n)} \equiv \exp\left[-\sum_{k=1}^{N} |\alpha_{m(n),k}(\tau)|^2 \beta_k/2\right],$$

$$\Gamma_{\pm} \equiv \exp\left[-\sum_{k=1}^{N} |\alpha_{m,k}(\tau) \pm \alpha_{n,k}(\tau)|^2 \beta_k/2\right],$$

and

$$\beta_k \equiv \coth\left[\frac{1}{2}\ln(1 + 1/\bar{n}_k)\right]. \tag{4.9}$$

4.2 Optimization calculation

When all of the required $2N + 1$ pulse segments are used, the fidelity is guaranteed to be unity when the optimal pulse shape $\Omega(t)$ is calculated for an arbitrary detuning and gate time. The problem becomes more interesting when fewer segments are used, because the problem then becomes an over-constrained one that calls for an optimization procedure*. Qualitatively this procedure can be defined by requiring that, whatever the pulse shape might be, the gate phase must be $\pi/4$. In other words, any infidelity in the final state should be a result of the residual spin-motion entanglement and not because we simply did the wrong type of gate. The quantity to be optimized is obviously the fidelity, because that is what ultimately

*The optimization formalism described here is based on private correspondence with Dr. Zhexuan Gong.

matters. Unfortunately, the expression for the fidelity is not quadratic in Ω as the geometric phase is, which means that a complex nonlinear optimization algorithm in general needs to be applied. In the solution space of interest – namely, pulse shapes that achieve high fidelity gates – we can approximate the infidelity $(1-\mathcal{F})$ by assuming it is small and expanding the exponential terms in $\alpha(\tau)$ to derive an expression that *is* quadratic in Ω. Since we will always be able to scale the optimal solution to achieve the proper geometric phase, even when the optimal fidelity is less than unity, the fidelity simplifies to

$$\mathcal{F} = \frac{1}{8}\left[2 + 2\left(\Gamma_m + \Gamma_n\right) + \Gamma_+ + \Gamma_-\right] \tag{4.10}$$

and, discarding terms of higher order than $|\alpha(\tau)|^2$, the infidelity is

$$\begin{aligned} 1-\mathcal{F} &\approx \frac{1}{4}\sum_{k=1}^{N}\beta_k\left(\alpha^*_{k,m}(\tau)\alpha_{k,m}(\tau) + \alpha^*_{k,n}(\tau)\alpha_{k,n}(\tau)\right) \\ &\equiv \sum_{p=1}^{P}\sum_{p'=1}^{P}\Omega_p\Omega_{p'}B_{p,p'} \\ &= \mathbf{\Omega}^T\mathbf{B}\mathbf{\Omega} \end{aligned}$$

To minimize this infidelity subject to the constraint that the geometric phase is $\pi/4$, we use the method of Lagrange multipliers to define a scalar quantity Λ as a function of Ω and the multiplier λ,

$$\Lambda(\Omega,\lambda) = \mathbf{\Omega}^T\mathbf{B}\mathbf{\Omega} - \lambda\left(\mathbf{\Omega}^T\mathbf{D}\mathbf{\Omega} - \pi/4\right) \tag{4.11}$$

where by design, the stationary points satisfy $\frac{\partial \Lambda}{\partial \Omega} = 0$ and $\frac{\partial \Lambda}{\partial \lambda} = 0$. The form of $\frac{\partial \Lambda}{\partial \Omega}$ is not so obvious in the tensor representation, but looking at a few terms of the derivative and rearranging terms shows that

$$\begin{aligned}
\frac{\partial}{\partial \Omega}\mathbf{\Omega}^T\mathbf{B}\mathbf{\Omega} = \sum_{p=1}^{P}\sum_{p'=1}^{P}\frac{\partial}{\partial \Omega}B_{p,p'}\Omega_p\Omega_{p'} =& (B_{1,1}\Omega_1 + B_{1,1}\Omega_1) + (B_{1,2}\Omega_2 + B_{1,2}\Omega_1) + \cdots \\
&+ (B_{2,1}\Omega_2 + B_{2,1}\Omega_1) + (B_{2,2}\Omega_2 + B_{2,2}\Omega_2) + \cdots \\
=& (B_{1,1}\Omega_1 + B_{1,1}\Omega_1) + (B_{1,2}\Omega_2 + B_{2,1}\Omega_2) + \cdots \\
&+ (B_{1,2}\Omega_1 + B_{2,1}\Omega_1) + (B_{2,2}\Omega_2 + B_{2,2}\Omega_2) + \cdots \\
=& \left(\mathbf{B} + \mathbf{B}^T\right)\mathbf{\Omega},
\end{aligned}$$

yielding the set of equations

$$\begin{aligned}
\frac{\partial \Lambda}{\partial \Omega} &= (\mathbf{B} + \mathbf{B}^T)\mathbf{\Omega} - \lambda(\mathbf{D} + \mathbf{D}^T)\mathbf{\Omega} = 0 \\
\frac{\partial \Lambda}{\partial \lambda} &= \mathbf{\Omega}^T\mathbf{D}\mathbf{\Omega} - \frac{\pi}{4} = 0
\end{aligned}$$

The first equation is equivalent to a generalized eigenvalue problem, $\mathbf{F}\vec{V} = \lambda\mathbf{G}\vec{V}$, whose solution consists of two matrices $\mathbf{V}$ and $\mathbf{L}$. The columns of $\mathbf{V}$ are the vector solutions $\vec{V}$ associated with the scalar eigenvalues λ in the corresponding column of the diagonal matrix $\mathbf{L}$. Identifying $\mathbf{F} = \mathbf{B}+\mathbf{B}^T$, $\mathbf{G} = \mathbf{D}+\mathbf{D}^T$, and $\vec{V} = \mathbf{\Omega}$, the global minimum fidelity is obtained by calculating the exact (not approximated) fidelity corresponding to each of the eigenvectors in the solution matrix $\mathbf{V}$ and selecting the one with the highest value.

A caveat to this optimization method is that the fidelities associated with the pulse shape solutions must be viewed as lower bounds on the actual theoretical fidelity for the specified gate, because the function being minimized is an approximation to the true infidelity. Thus, the solutions based on the approximate infidelity will not in general be truly optimal. Clearly, though, the exact fidelity associated with a given pulse shape is calculated independently of how that shape was determined; hence the calculated fidelity is at worst a lower bound. Furthermore, the approximation is automatically more accurate in the parameter space supporting high fidelity solutions, so for practical purposes this caveat is not important.

The obvious system with which to begin analyzing this segmented pulse scheme is the simplest case of a two ion chain. Now that we have an optimization algorithm to determine the optimal pulse amplitude for a constant pulse regardless of gate parameters, we can make a fair comparison. Figure 4.1 shows the theoretical fidelity versus the gate detuning μ (using the optimal pulse amplitude for each detuning). Using the trap frequencies $\omega_z = 2\pi \times 600$ kHz and $\omega_t = 2\pi \times 4.38$ MHz, the gate time is set to $2 \times 2\pi/((\omega_1 - \omega_2)/2) \approx 100$ µs. The plot shows three fidelity curves, for initial phonon excitations $\bar{n}_1 = \{0, 2, 10\}$. The corresponding plots for the five segment pulses are all unity for all detunings. This shows that when "full control" is applied, meaning $2N + 1$ segments are utilized, the gate is much less sensitive to the initial crystal temperature. The commensurate points at unit fidelity in the plot are not affected by the temperature, of course, but the bandwidth about which a high fidelity is possible shrinks as $\bar{n}$ increases.

An immediate concern with the pulse shaping scheme is how much optical

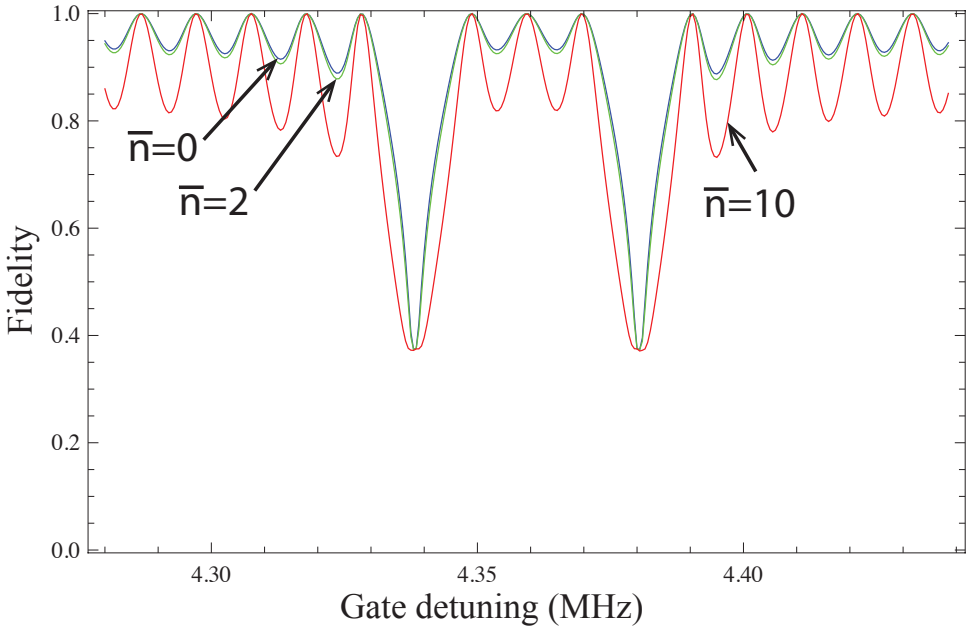

Figure 4.1: Theoretical two ion gate fidelity for a constant pulse.
The colors {blue, green, red} show the fidelity for different values of initial temperature $\bar{n} = \{0,\ 2,\ 10\}$.

power is required compared to the constant pulse gate. Figure 4.3 shows the required power in terms of the carrier Rabi frequency. The single value plotted for the five segment pulse solutions is the maximum amplitude of each pulse. There is not a significant difference in the required optical power. Figure 4.4 shows all five pulse amplitudes as a function of detuning. As evident in the figure, since the value of Ω_p is a real number, it can be negative. A negative amplitude indicates a π phase shift on the spin-dependent force, causing an abrupt reversal of the direction of the trajectory for each spin component of the ion wavepacket. The resulting trajectories have kinks in them producing "star" and "flower" patterns compared with the coiled patterns of the pulse shapes with uniform sign, as illustrated in Fig. 4.2. The restriction of Ω_p to the real numbers can also be visualized as preventing the phase space trajectories

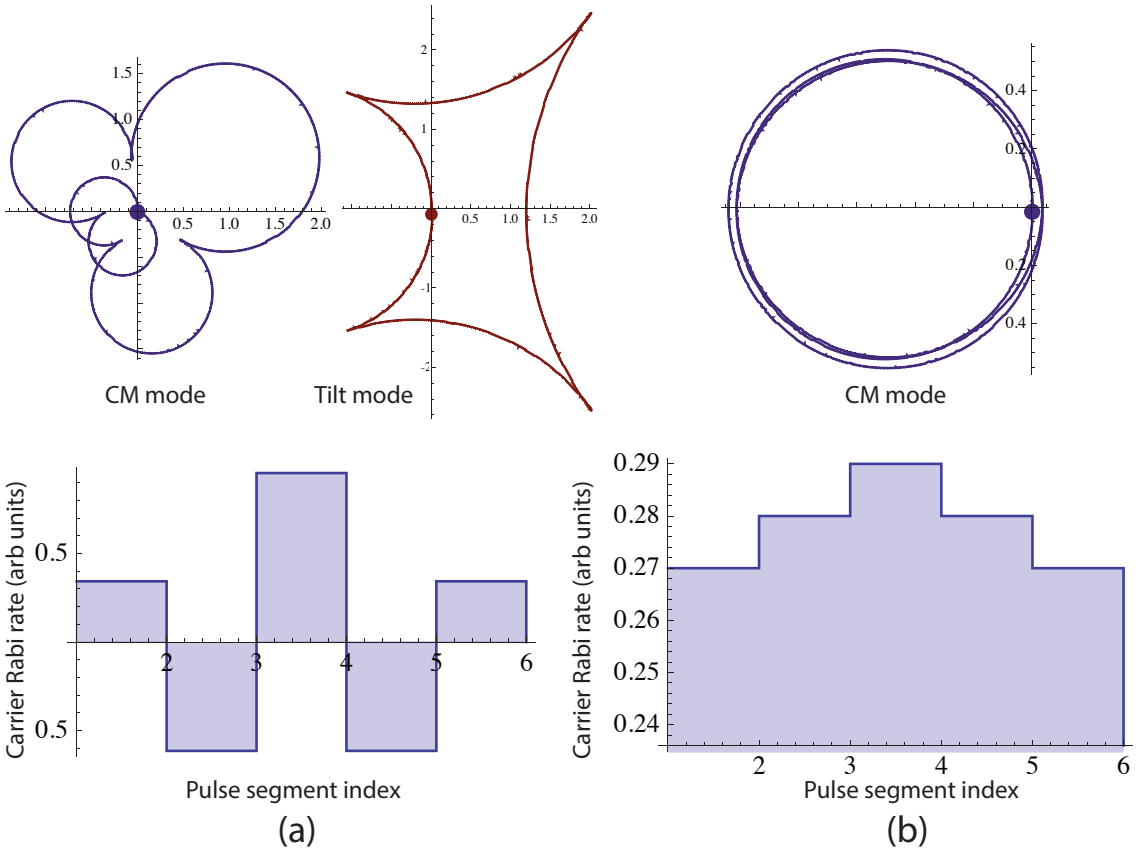

Figure 4.2: Phase space trajectory shapes
Example trajectories for pulse solutions with segments of (a) alternating sign and (b) uniform sign.

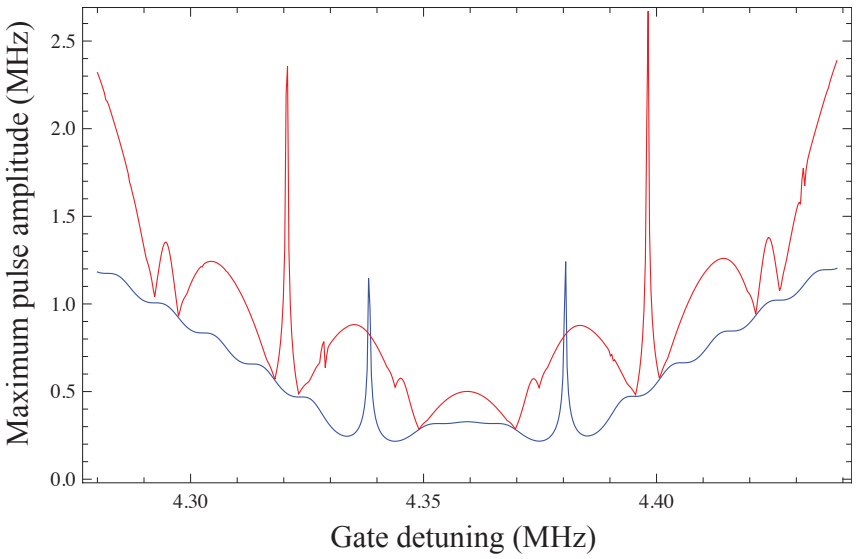

Figure 4.3: Two ion gate optical power comparison.
The constant pulse amplitudes are shown in blue and the maximum amplitude of the five segments is shown in red.

from bifurcating as they would if the eigenbasis upon which the spin-dependent force acted was suddenly changed. It is interesting that there is a great deal of symmetry to the shapes, which probably reflects the temporal symmetry of the interaction itself. In other words, since there are no dissipative processes in our model of the entangling interaction, the optimal trajectories should have the same form whether time flows forward or backward. Hence, for five segment pulses, two pairs of segment amplitudes should roughly overlap to cause the plot to seemingly show only three curves.

The theoretical expression for the fidelity is not particularly helpful when actually trying to measure the fidelity. Experimentally we measure the fidelity by measuring the populations of the state as well as the contrast of a parity curve, which we will define in the following derivation. A general two qubit density matrix

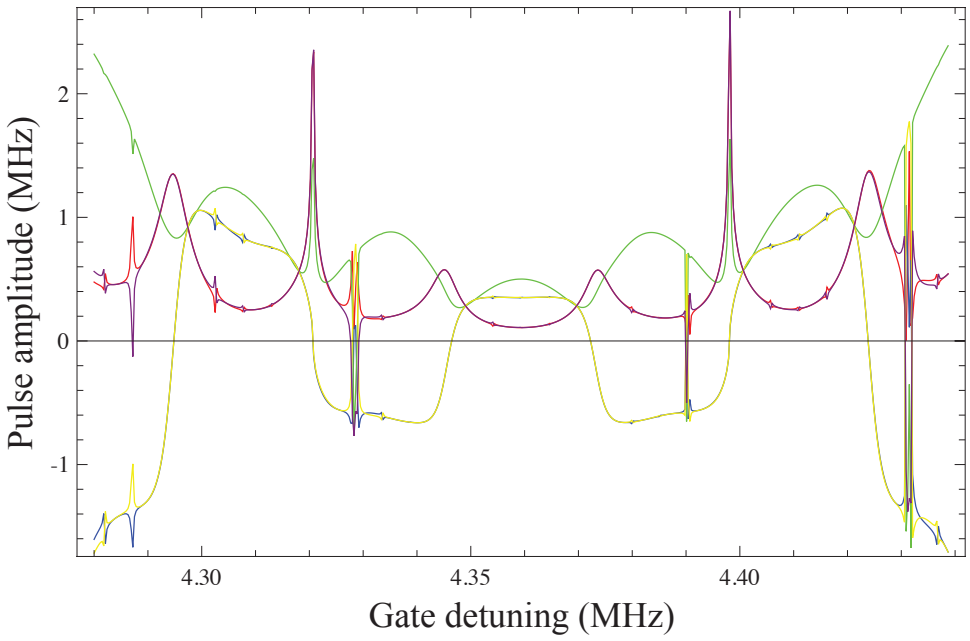

Figure 4.4: Pulse segment amplitudes.
Amplitudes are in terms of carrier Rabi rate for the optimal five segment solutions of the two ion entangling gate. Negative values indicate a π phase shift on the spin-dependent force.

ρ_{gen} is given by

$$\rho_{gen} = \begin{pmatrix} \rho_{00} & \rho_{01} & \rho_{02} & \rho_{03} \\ \rho_{01}^* & \rho_{11} & \rho_{12} & \rho_{13} \\ \rho_{02}^* & \rho_{12}^* & \rho_{22}^* & \rho_{23} \\ \rho_{03}^* & \rho_{13}^* & \rho_{23}^* & \rho_{33} \end{pmatrix} \tag{4.12}$$

where the subscripts are binary code abbreviations indicating the matrix elements $\rho_{00} \equiv \rho_{|00\rangle\langle 00|}$, $\rho_{01} \equiv \rho_{|00\rangle\langle 01|}$, $\rho_{23} \equiv \rho_{|10\rangle\langle 11|}$, etc. In a two qubit Hilbert space the rotation operator $\hat{R}(\theta, \phi)$ on the first qubit is represented by a 4×4 matrix given by the Kronecker product $\mathbf{R}_1(\theta, \phi) = \mathbf{R}(\theta, \phi) \otimes \mathbf{I}$ of the single qubit 2×2 matrices, where $\mathbf{I}$ is the identity operator. Likewise, $\mathbf{R}_2(\theta, \phi) = \mathbf{I} \otimes \mathbf{R}(\theta, \phi)$. A global $\pi/2$ rotation $\mathbf{R}_G(\pi/2, \phi) = \mathbf{R}_2(\pi/2, \phi) \cdot \mathbf{R}_1(\pi/2, \phi)$, often called the "analyzer pulse", on

the general state ρ_{gen} yields an output

$$\rho_f = \mathbf{R}_G(\pi/2, \phi) \cdot \rho_{gen} \cdot \mathbf{R}_G^\dagger(\pi/2, \phi)$$

The parity of the state ρ is defined as the sum of the even parity populations minus the sum of the odd parity populations, which for two qubits is

$$\Pi_2(\rho) \equiv (\rho_{00} + \rho_{33}) - (\rho_{11} + \rho_{22})$$

Using the convenient form $\rho_{xy} = A_{xy} e^{-i\phi_{xy}}$ for the "coherences" (off-diagonal density matrix elements), the parity of ρ_f becomes a function of the analyzer pulse phase ϕ with the form

$$\Pi_2(\rho_f, \phi) = A_{12} \cos\phi_{12} - A_{03} \cos(2\phi - \phi_{03}) \tag{4.13}$$

If $\rho_{gen} = \rho_{ideal}$, the parity curve resulting from a scan of the analyzer pulse phase ϕ will look like Fig. 4.5. The fidelity of the general state ρ_{gen} with respect to our ideal final state ρ_{ideal} is given by $\mathcal{F} = \mathrm{Tr}\left[\rho_{ideal} \cdot \rho_{gen} \cdot \rho_{ideal}^\dagger\right]$. Recalling the ideal state from Sec. 3.2.2, the fidelity expression simplifies to

$$\mathcal{F} = \frac{1}{2}\left(\rho_{00} + \rho_{33} + A_{03} \sin(\phi_g - \phi_{03})\right) \tag{4.14}$$

where the diagonal elements are real valued probabilities. The utility of the parity signal is now obvious. In conjunction with the populations of the $|00\rangle$ and $|11\rangle$ states, the amplitude of the parity curve (generated by scanning the identical phases of the

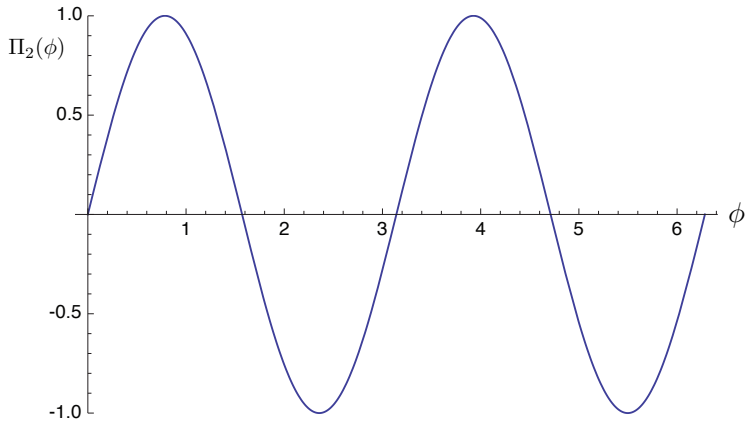

Figure 4.5: Ideal two qubit parity curve.
The parity function is plotted as a function of the analyzer pulse phase, scanned from 0 to 2π. The ideal coherence $\rho_{03} = \frac{1}{2}e^{i\pi/2}$.

global rotation) provides the quantities necessary to determine the state fidelity. This rigorous form of the fidelity expression includes the absolute value of the gate phase ϕ_g with respect to the phase of the coherence ρ_{03}. For the purposes of proving whether or not the final state is *entangled*, this phase is irrelevant, as all it does is shift the phase of the parity curve. Moreover, for the purpose of characterizing the gate performance in the experiments it is also unimportant. What is important is the parity curve contrast. We thus treat the phase offset as a free parameter, simplifying the fidelity to the form used in the experimental data below,

$$\mathcal{F} = \frac{1}{2}\left(\rho_{00} + \rho_{33} + A_{03}\right) \tag{4.15}$$

If $\mathcal{F} > 0.5$, the two qubits are verifiably entangled, meaning that their states are non-classically correlated [14]. If it drops to 0.25, the state has become a complete statistical mixture.

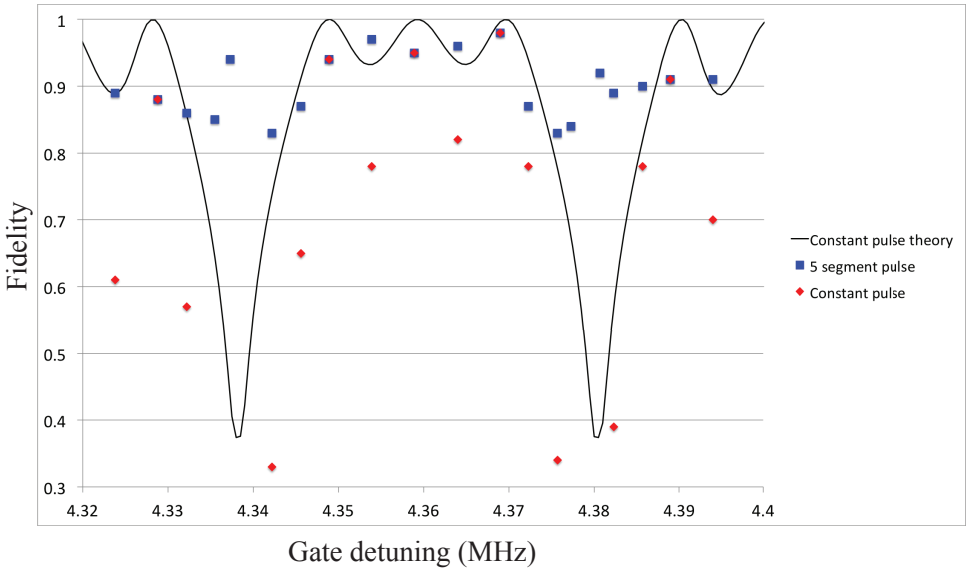

Figure 4.6: Two ion constant vs five segment pulse data.

4.3 Two ion data

We tested this pulse shaping scheme with a chain of two $^{171}Yb^{+}$ ions using the same trap frequencies as above. Figure 4.6 displays the results. The shapes of the constant pulse fidelity curve shows good qualitative agreement with the theory plot, with the five segment data showing dramatic improvement across the entire range of detunings as expected. Each data point in the plot is generated by the following procedure. First, the two ion crystal is Doppler cooled for a few milliseconds before being initialized to the $|0\rangle$ state by optical pumping for 10 µs. Then the coherent operations begin, starting by resolved sideband cooling both of the normal modes to near the ground state. Figure 4.7 shows the relative red sideband amplitudes before and after cooling. At this point the ions should be in a pure initial state of spin and motion $|\psi_i\rangle = |00\rangle \otimes_k |0\rangle_k$, where $k = \{1, 2\}$. The initialization is followed

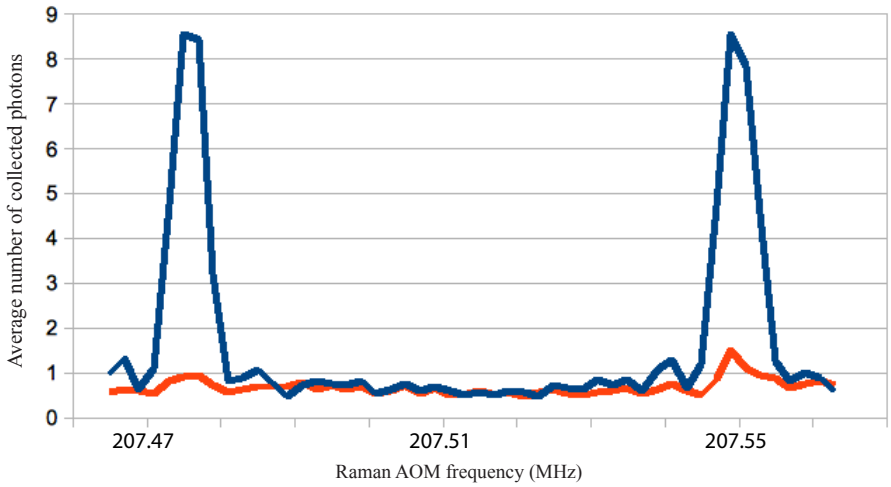

Figure 4.7: Two ion sideband cooling.
A Raman sideband scan shows the strength of the red sideband transition with (red) and without (blue) sideband cooling both modes.

immediately by the gate. For the data plotted in Fig. 4.6, the gate duration is 100 µs. The shaped pulses consist of five concatenated 20 µs flat segments. The last coherent operation before detection is the application of the global analyzer pulse described in the previous section, which effectively rotates the measurement basis by rotating the qubits themselves. Finally, the detection beam is applied for 500 µs while the collected fluorescence photons are counted. This sequence is repeated 1000 times to acquire a statistically accurate histogram (see Sec. 2.4.3). The populations are calculated by fitting the measured histogram to a superposition of dark, single bright, and double bright state Poissonians. These three basis state histograms are separately measured prior to the experiment using appropriate state preparation with resonant microwaves.

All coherent operations are controlled by the AWG driving the global Ra-

man beam (see Sec. 2.5.3). For the two ion chain, the addressing beam is not tightly focused in order to equally illuminate the ions. For the constant pulse gates, the optimal pulse amplitude was found empirically by simply varying the 355 nm power in real time while equalizing the $|00\rangle$ and $|11\rangle$ populations. The worse the gate performance, the higher the odd parity population is as the result of residual spin-motion entanglement. For the five segment pulse experiments, the optimal amplitudes applied at each detuning are calculated based on the measured trap frequencies obtained from a sideband scan. Similar to the constant pulse case, we apply the calculated pulse *profile* given by the relative segment amplitude values, but empirically find the optimal absolute optical power by equalizing the even parity state populations. To accurately implement the segmented pulse gate, the calculated segment amplitudes must be calibrated against the nonlinearity of the AWG amplitude values. The AWG output rf power is controlled by a simple digital number ranging from 0 to 2047. By varying the AWG amplitude and measuring the carrier Rabi rate for a single ion corresponding to each value (at a constant optical intensity), we establish a calibration curve that maps the calculated optimal pulse shape to the corresponding AWG amplitude values that are actually input to the control software.

A detuning with a particularly stark contrast between the constant and segmented pulse gates is given by $r_C = 23$, $r_T = 1$, which is very close to the tilt mode. Figures 4.8 and 4.9 plot the measured parity curves for these two gates. The constant pulse parity curve shows a small offset in addition to its small amplitude. Recalling the form of the parity function, this offset ideally represents undesired

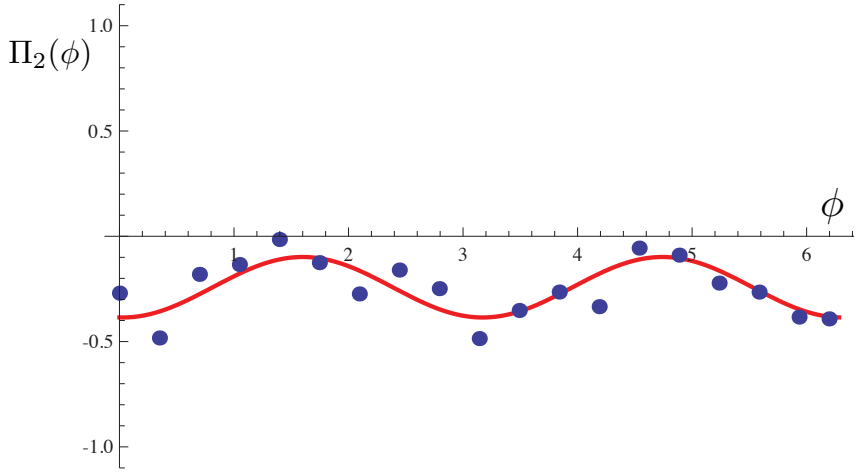

Figure 4.8: Low contrast two ion parity for a constant pulse. Gate detuning is $r_C = 23$, $r_T = 1$ for the 0.1 ms gate. $\mathcal{F} = 30\%$.

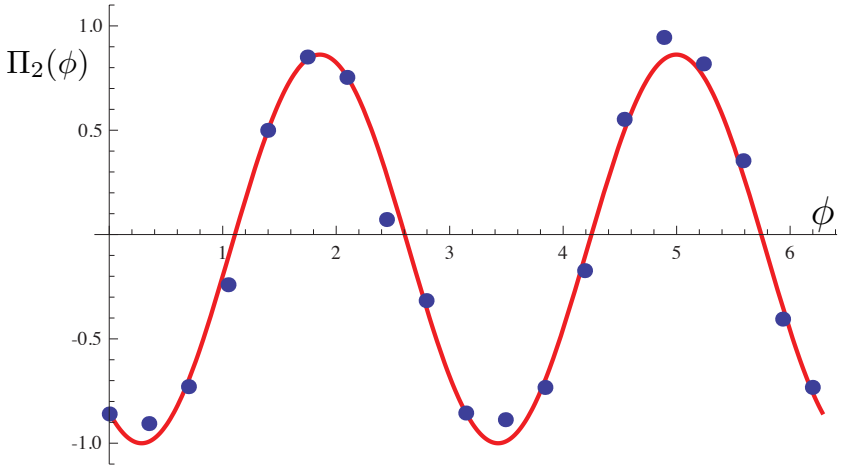

Figure 4.9: High contrast two ion parity for a five segment pulse. Gate detuning is $r_C = 23$, $r_T = 1$ for the 0.1 ms gate. $\mathcal{F} = 94\%$.

population in the odd parity states $|01\rangle$ and $|10\rangle$; hence, such an offset can only appear when the fidelity is low by conservation of probability. In our experiments, however, this offset is usually explained by the more mundane fact that the histogram fit to the single bright histogram is more sensitive to minor drifts in ion brightness.

4.4 Three ion data

The two ion data from the previous section was the simplest test of the pulse shaping scheme without the additional complications from individual addressing and individual qubit state detection. When working with three and, in the next section, five ion chains, we use the multi-channel PMT array described in Sec. 2.4.3 to measure the state of each qubit individually. The ion spacing was set to 5.2 µm, with transverse trap frequencies $2\pi \times \{2.60,\ 2.55,\ 2.48\}$ MHz and a $2\pi\times$400 kHz axial frequency. In order to address only two of the three, we focus the addressing beam tightly between the pair using a Ronar Smith 115 mm doublet such that the Rabi rates for the two ions are equal. The resulting beam waist of $w_0 = 2.8$ µm was determined by measuring single ion fluorescence as a function of the lateral position of the doublet, shown in Fig. 4.4. Since the beam is incident at 45° to the chain, the effective waist focused between the target pair is $w = w_0\sqrt{2} \approx 4$ µm. The theoretical spillover assuming a perfect Gaussian beam is 3% for these crystal parameters. The beam profile was not ideally Gaussian, however. Due to spherical aberrations introduced by the lens system and diffraction from unavoidable clipping of the beam

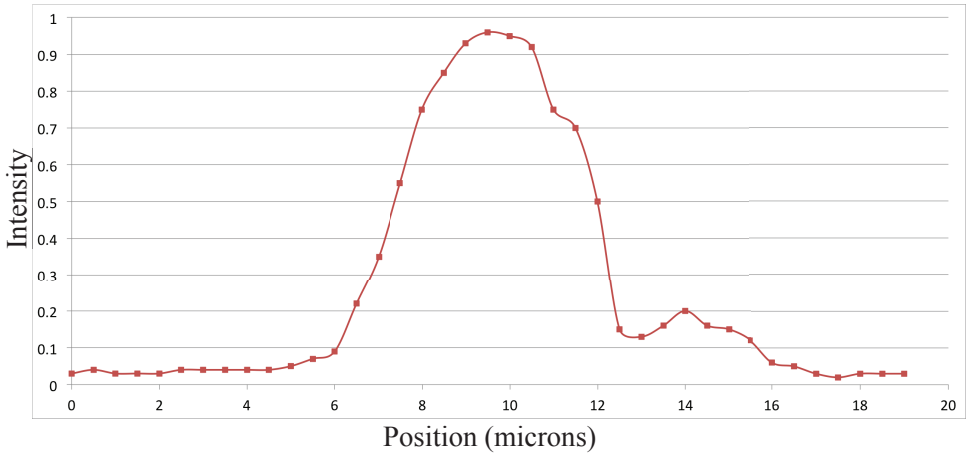

Figure 4.10: Addressing beam profile.
Relative intensity plotted as normalized ion brightness vs doublet displacement in microns.

on part of the ion trap assembly inside the vacuum chamber, half of the beam profile is steeper than it should be with a significant bump in the intensity. To avoid this feature, we positioned the third ion on the smoother side of the profile.

The spillover on the third ion is defined as the fraction of the third ion's Rabi rate to the target pair Rabi rate. This value is measured on a daily basis by driving carrier Rabi oscillations on the target pair and independently measuring each ion's Rabi frequency by aligning each ion to a separate PMT channel. The spillover was minimized by adjusting the beam focus and alignment and ranged typically between 2% and 5%. Figure 4.11 shows an example of a carrier pulse duration scan over 300 µs, where the third ion Rabi rate is much lower than the target pair. The sideband scan of the motional mode frequencies shown in Fig. 4.12 illustrates both the addressing as well as the motional mode coupling parameters. The third ion (blue) remains dark while the first (green) and middle ion (red) are excited. Both the target ions participate equally in the center of mass mode, but the middle ion

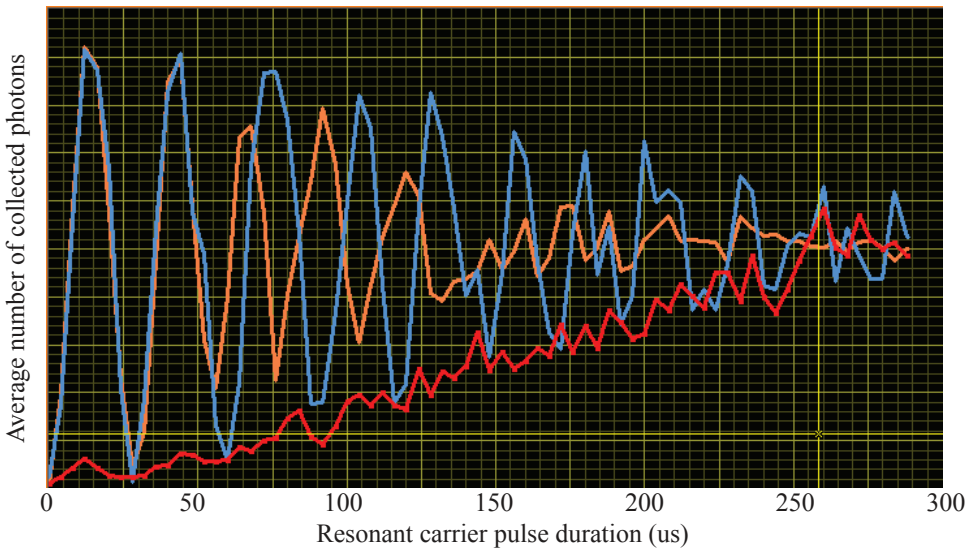

Figure 4.11: Spillover measurement for three ion chain.
Rabi oscillations for three ions over 300 µs show a spillover of 3% on the third ion (red).

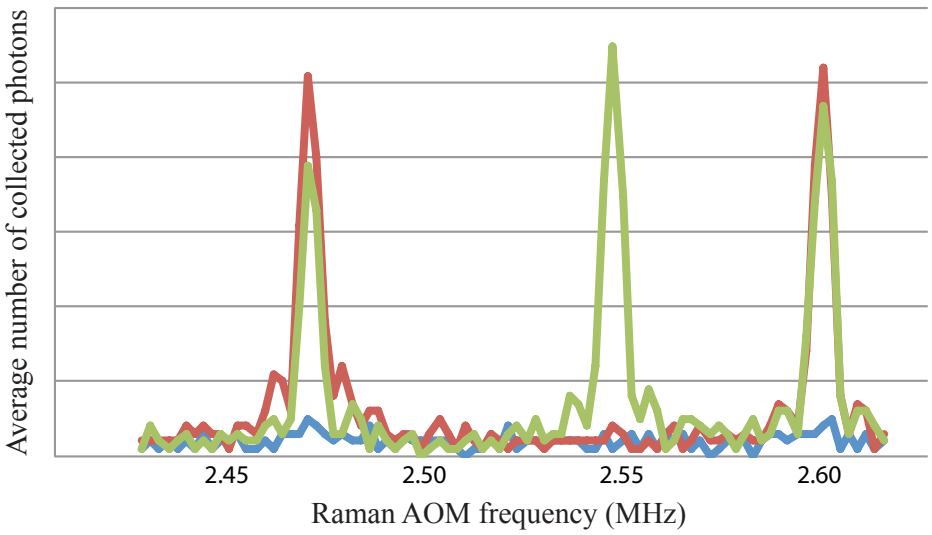

Figure 4.12: A sideband scan for three ions.
The individual state detection shows the coupling of the two target ions (ion 1: green, ion 2: red) to the three motional modes. The third ion (blue) is dark because the spillover is low.

does not couple to the tilt mode, so it remains dark at that frequency. The middle ion couples more strongly to the zig-zag mode than the outer ions, so the middle qubit rotates further during the 300 µs pulse than the first qubit does.

Similar to the two ion crystal data, the data taken with the three ion chain consists of measuring the two-ion entangled state fidelity at various detunings for different numbers of pulse segments. Theoretically the optimal fidelity should approach unity as the number of segments increases to the $2N + 1 = 7$ segments required for "full control". The theoretical fidelity curves for the 100 µs gate time are shown in Fig. 4.13. In contrast to the theoretical curve for the constant pulse solutions on a two ion chain, these optimal constant pulse solutions never quite achieve a perfect gate. This is a direct result of the incommensurability of the three mode frequencies. The best detuning for the constant pulse gate turns out to be just blue of the CM mode, and this is true as the number of ions increases as well. This is the detuning where the coupling is predominantly to the CM and tilt mode and where the higher modes are far enough away not to trace large trajectories in phase space. Considering the required optical power curves, however, the lower power solutions are found within the transverse mode bandwidth, where the performance of the constant pulse suffers the most due to the more equal coupling to all the modes. As the gate time decreases, the best detuning for the constant pulse mode gets pushed further blue into increasingly high power solutions.

The three ion data is plotted in Fig. 4.14, encompassing 25 separate entangled state fidelities for various detuning and numbers of segments. The experimental procedure was the same as in the two ion data. Overall the trend of improvement

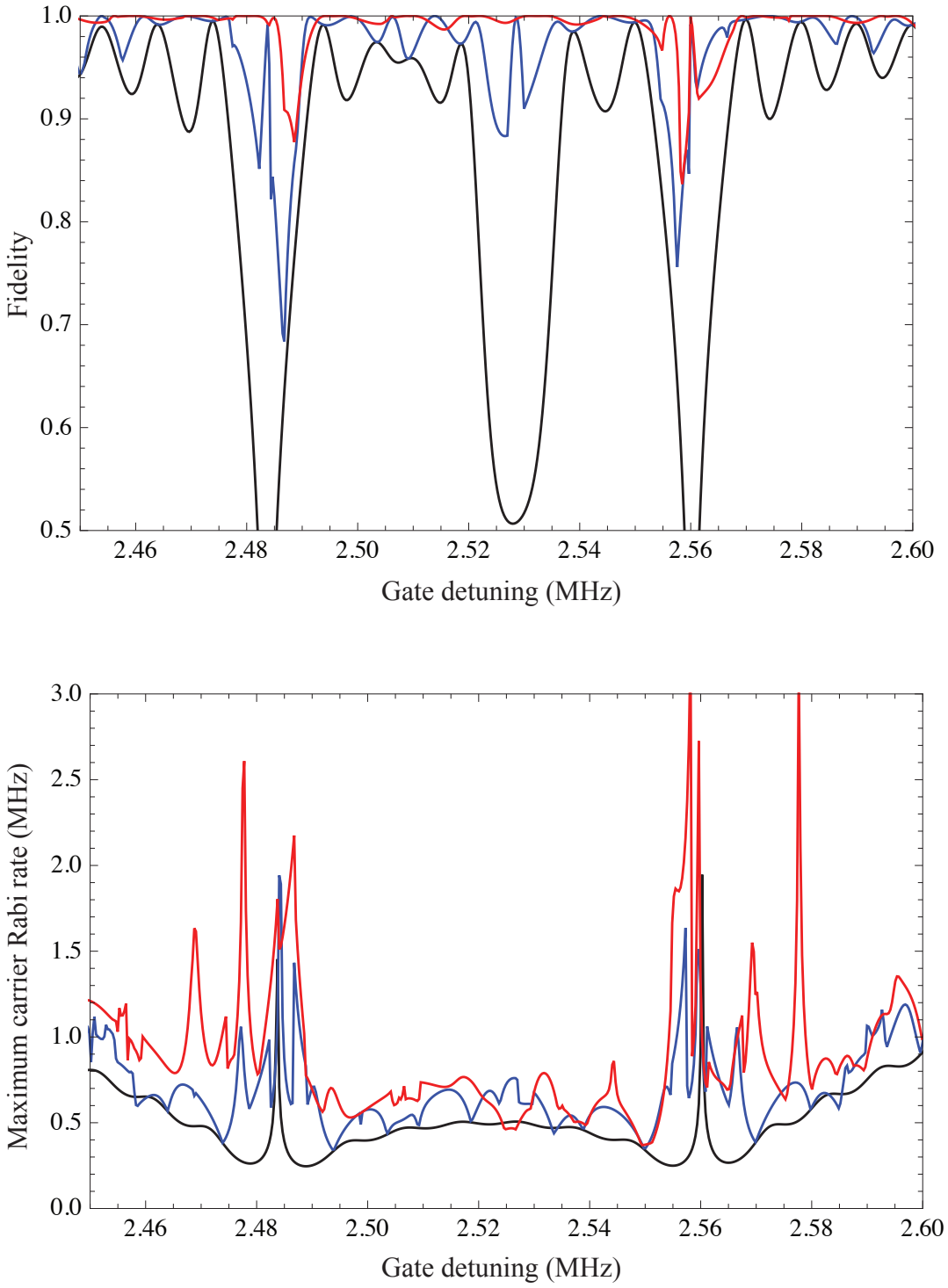

Figure 4.13: Three ion theoretical fidelity and maximum power plots. Theoretical fidelity and maximum carrier Rabi rate for the optimized pulse shapes on a three ion chain given a 100 µs gate time. Number of segments: 1 (black), 3 (blue), and 5 (red).

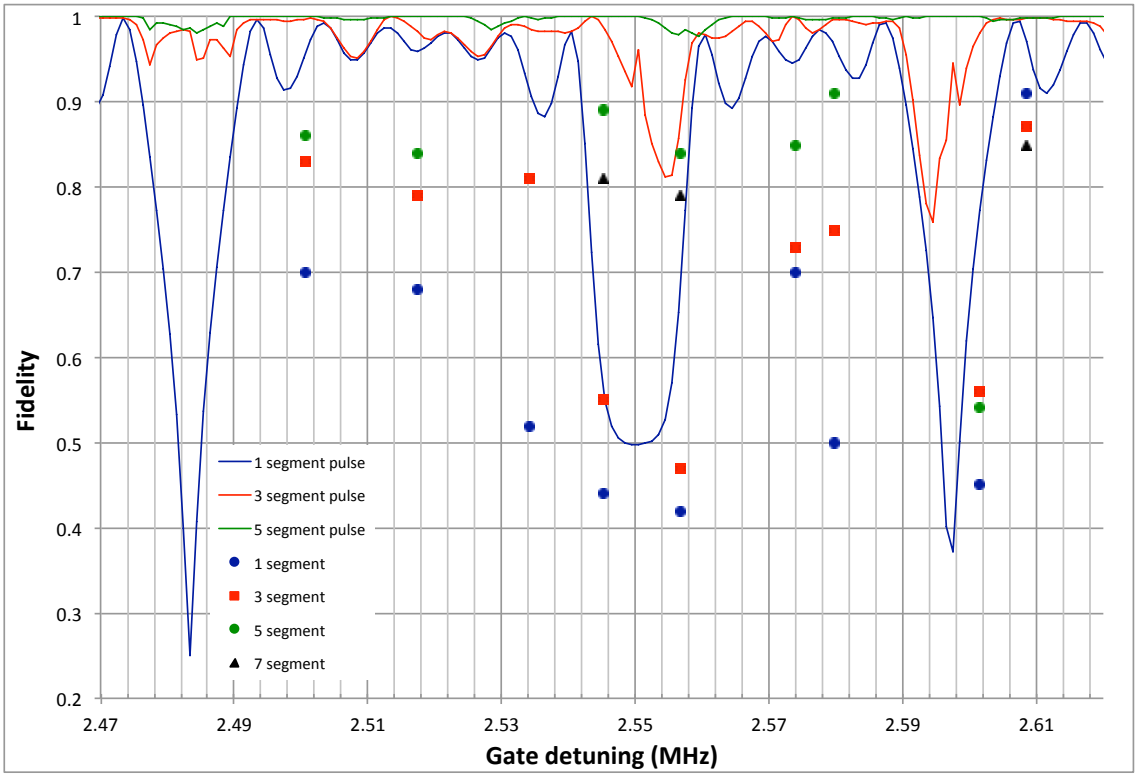

Figure 4.14: Complete three ion data.
The theoretical and measured fidelities are plotted for gates between ion pair $\{1, 2\}$ with a gate time 100μs. Pulse shapes with 1, 3, 5, and 7 segments were applied for comparison.

with segment number is clear, but the seven segment pulses are conspicuously worse than the five segment pulses. This was due to the fact that the required power increased such that 355 nm beam scatter was inducing charge that pushed the ions during the course of the gate.

All of the measured fidelities fall short of theory on an absolute scale. Some of the this is because not all the data points shown had proper sideband cooling, as we discovered after the fact. Recalling Fig. 4.1, the higher the initial temperature, the worse the optimal fidelities are, getting worse as the number of ions increases. Much of the shortcoming can be contributed to errors due to simple beam steering. The addressing beam is focused to effectively $\sim 2.8\sqrt{2}$ µm in the z direction due to the beam geometry and is aligned directly between the ions. This means that they are each on the slope of the beam profile, where they are most sensitive to fluctuations in position. This kind of beam steering is caused by air currents across the optical table, due in large part to the HEPA air filters that continually blow clean air across the optics from above. Although the Raman beam paths are enclosed in boxes to protect from these small currents, they still drive intensity fluctuations at the ions. The amplitude of the beam steering can be estimated by performing carrier Rabi oscillations and fitting the decaying sinusoid to a simulated curve. We find that the target ions' Rabi oscillations decay to about 60% after four to five flops. The Rabi rate is proportional to $\sqrt{I_A I_G}$ for the two-photon Raman transition, so assuming the global beam is broad enough to be unaffected by beam steering, the single qubit rotations will be proportional to $\Omega \propto \sqrt{I_A} \propto e^{-z^2/w^2}$. The scale factor for the

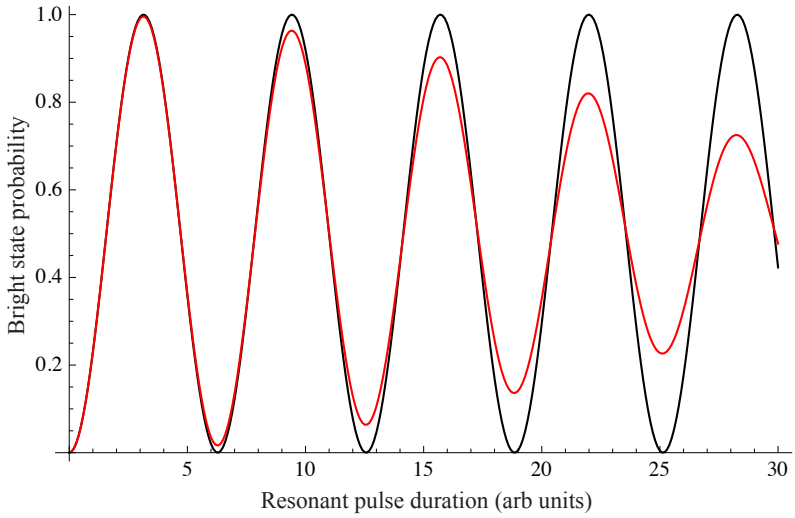

Figure 4.15: Simulated decay of carrier Rabi oscillations.
The black curve assumes no beam steering. The red curve simulates a ±200 nm beam steering amplitude.

intensity at each ion can be written as

$$g(z,y) = g_0 e^{-(d+z)^2/w^2} e^{-y^2/w^2} \tag{4.16}$$

where $g_0 \equiv e^{d^2/w^2}$ and d is half of the distance between the target ion pair. In the actual experiment, the intensity fluctuations occur on a timescale on the order of 1 ms, and since each experimental cycle is several milliseconds long, the decay manifests itself in the average over many experiments. To produce the simulated Rabi oscillation in Fig. 4.4, the value of z and y are selected by a random number generator between $\{-s, s\}$, where s is the beam steering amplitude. The evolution of the $|0\rangle$ state is calculated as a function of time by applying the single qubit rotation operator with the intensity $g(z,y)$ over a duration of several flops. The plotted curve is simply the average of this calculation repeated a sufficient number

(∼300) of times. For $s \approx 200$ nm, the decay matches our observations. Assuming for simplicity that the beam steering only effects the single qubit rotations of the analyzer pulse, the next task is to estimate the reduction in parity contrast we expect for a given beam steering amplitude. The calculation is similar, except that the rotation angles for the two qubits are now interrelated. In the z direction, a beam deflection *toward* one ion is identically *away* from the other. In the y direction they are decoupled. Assuming the qubits start in the ideal final entangled state, then, the state after the analyzer pulse is given by

$$|\psi\rangle = \hat{R}_2\left(\frac{\pi}{2}e^{-(d+z)^2/w^2+d^2/w^2}e^{-y^2/w^2}, \phi\right)\hat{R}_1\left(\frac{\pi}{2}e^{-(d+z)^2/w^2+d^2/w^2,\phi}e^{-y^2/w^2}\right)|\psi_{ideal}\rangle$$

where the parity is defined as above for the pure state density matrix,

$$\rho(y,z) = |\psi(y,z)\rangle\langle\psi(y,z)|.$$

The parity Π thus becomes a function of y and z as well, with the measured parity curve being the average parity function given by

$$\Pi = \frac{1}{(2s)(2s)}\int_{-s}^{s}\int_{-s}^{s} dydz\ \Pi(y,z) \tag{4.17}$$

Figure 4.4 shows simulated parity curves for an ideal final state followed by an analyzer pulse that has an increasing beam steering amplitude. In actuality, the beam steering affects the gate itself as well, but since the coupling strength is proportional to the square root of the product of the intensities on the ions, the coupled nature

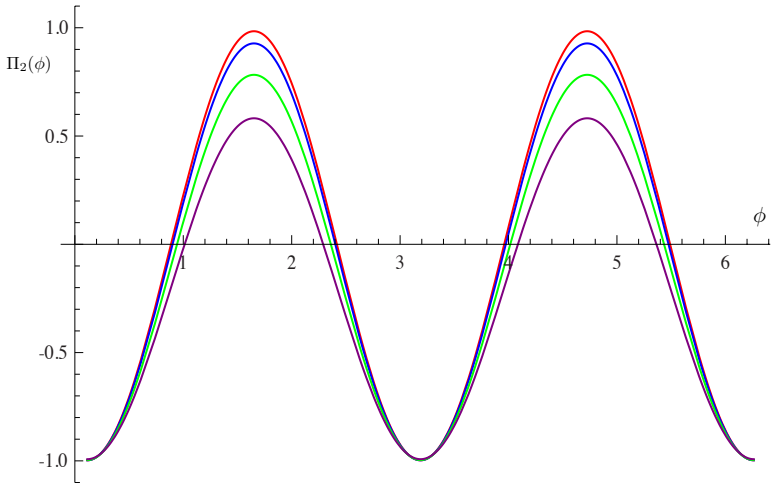

Figure 4.16: Simulated decay of two ion parity from beam steering. No steering: red, 200 nm amplitude: blue, 400 nm amplitude: green, 600 nm amplitude: purple.

of the z deflection error pushes the error to second order. This is not true for the vertical direction, but even with that error, the effect on the gate evolution operator is only to add a slight error to the geometric phase term. All together, beam steering alone contributes an offset of $\sim$5% to the measured fidelity. This remains true for the five ion data in the next section.

4.5 Five ion data

For the next set of experiments, we increased the number of ions in the chain to five (Fig. 4.17). For five ions, the superiority of the multi-segment pulse scheme is even clearer. Instead of scanning a range of detunings to verify the theory as in the two and three ion data, with the five ion chain the goal was to show more of a practical advantage to the technique by demonstrating that the best multi-segment gate is significantly better that the constant pulse gate, regardless of detuning.

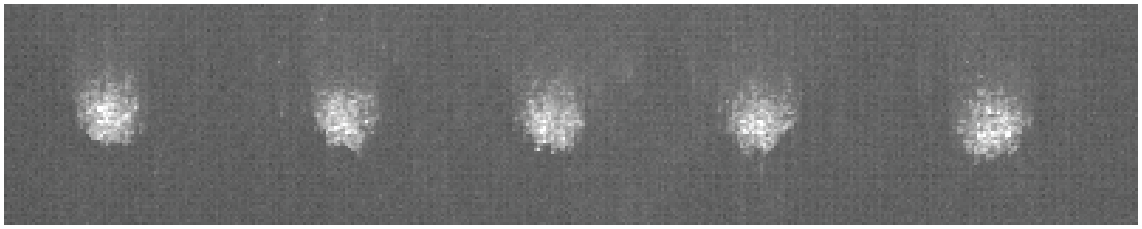

Figure 4.17: Image of five ion chain on intensified CCD camera.

Along the way we discovered some additional advantages to the scheme, including the robustness against detuning fluctuations and the opportunistic suppression of optical spillover effects. These topics are covered in the next few sections. Finally, we used the pulse shaping technique to perform sequential two-ion entangling gates to create a genuinely tripartite entangled "cat" state of three ions out of the five ion chain. This last demonstration required us to shuttle the ions between the coherent operations to pairwise and individually address the qubits.

The theoretical plots for constant, five segment, and nine segment pulses for a $\sim$200 µs gate are shown in Fig. 4.18 for ion pairs $\{1,2\}$ and $\{2,3\}$ for transverse trap frequencies $2\pi \times \{2.47,\ 2.51,\ 2.54,\ 2.57,\ 2.59\}$ MHz and a $2\pi\times$315 kHz axial frequency. We found that there was no noticeable improvement in the entangled state fidelity when using more than nine segments across a range of detunings. This is expected, because the theoretical difference between the eleven segment "full control" pulse shapes and the nine segment pulses is less than a percent for almost all detunings, which is unresolvable given our experimental errors. The best fidelities we achieved for the nine segment gates were 95% for both the $\{1,2\}$ and the $\{2,3\}$ pairs, as shown in Fig. 4.19. The best constant pulse gate performance we attained was a fidelity of 81% for pair $\{1,2\}$. Each of these gates were driven

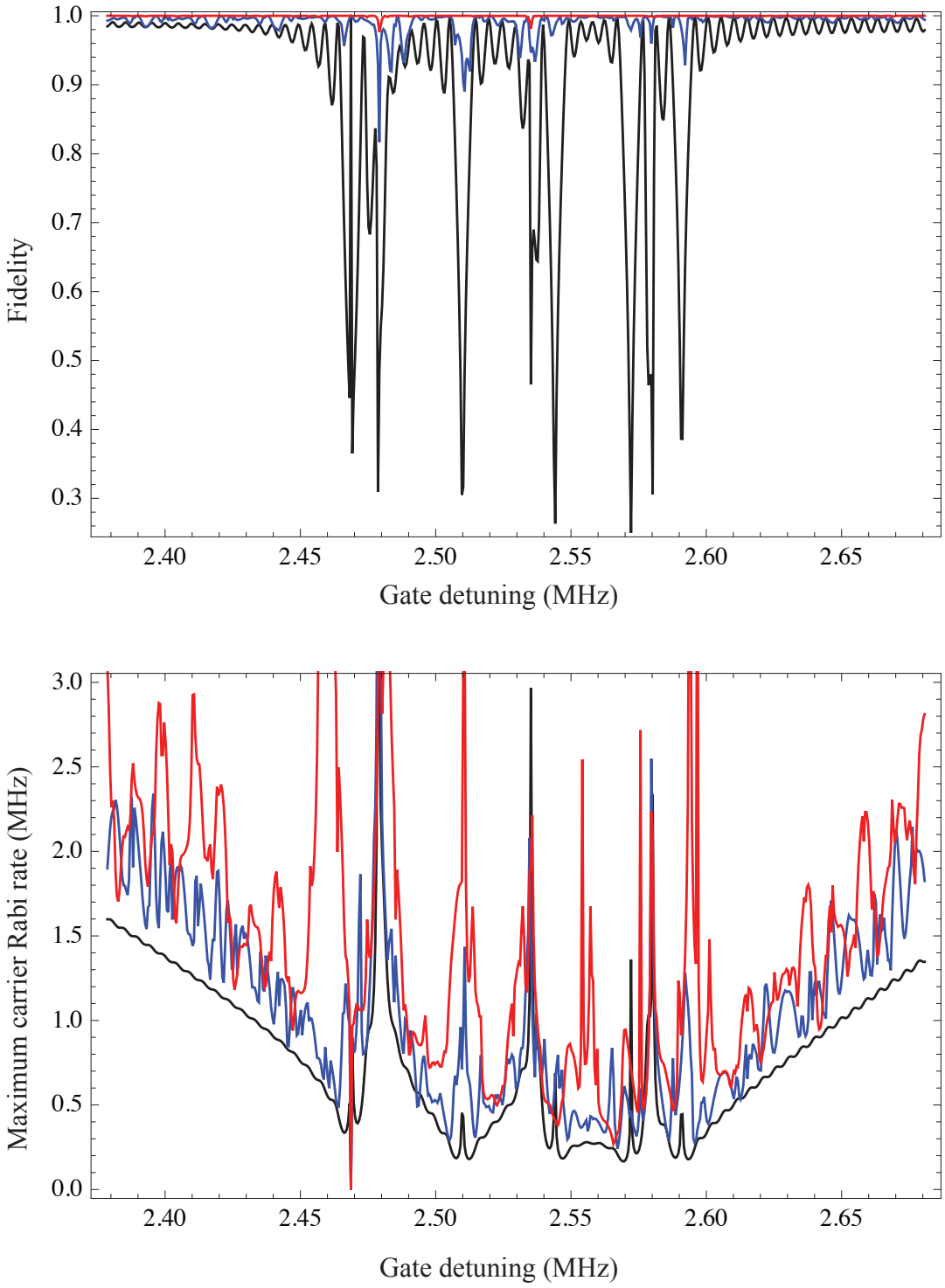

Figure 4.18: Theoretical fidelity and power curves for a five ion chain. Fidelity and associated maximum pulse amplitudes for optimized constant (black) gate pulses, and five (blue) and nine (red) segment gate pulses on ion pair $\{1, 2\}$.

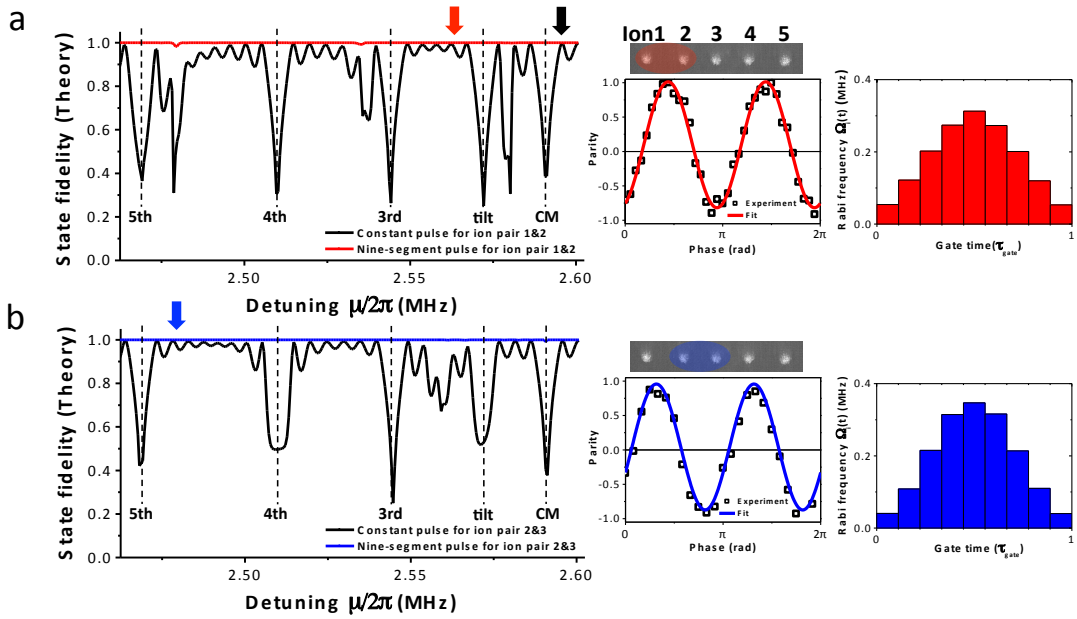

Figure 4.19: High fidelity entanglement of different pairs in a five ion chain. (a) Ion pair $\{1, 2\}$ detuning and corresponding pulse shape and parity curve. (b) Ion pair $\{2, 3\}$ detuning and corresponding pulse shape and parity curve.

at different detunings, selected to maximize both the two-qubit fidelity as well as to optimize the sequential gate performance. The gate on $\{1, 2\}$ was performed at a gate detuning given by (r_C, r_T) = (-3.3125, -1). The gate on $\{2, 3\}$ was performed at a gate detuning given by (r_C, r_T) = (-2.701, -1). And the constant pulse gate on $\{1, 2\}$ was performed at a gate detuning given by (r_C, r_T) = (1, 5).

4.6 Robustness to detuning fluctuations

The constant pulse gate performed significantly worse than the theoretical curve predicts. Part of this is explained by beam steering as detailed above, but part of it has to do with the fact that our trap frequencies drifted in unpredictable

ways during the course of the experiments. Due to an unfortunate feature of the trap assembly design, heat from the Yb ovens has a conductive path to the trap structure. During loading, the trap frequencies shift on the order of 10 kHz and slowly drift back as the trap structure cools. The random duty cycle of loading ions throughout the day causes the speed and even direction of the sideband drift to be unpredictable, making it infeasible to characterize and compensate for it. To perform gates, we monitored the sideband frequencies and waited until the drift speed was about 1 kHz/min or slower if possible. Even so, the drift effectively created a detuning error on most of the operations.

One of the practically useful features of the segmented pulse gates is that they are typically more robust against detuning errors or fluctuations. As the number of segments increases and the gate performance approaches the ideal, there is more detuning bandwidth within which the optimal pulse shape solutions do not rapidly change. Figure 4.20 shows a theory plot comparing a constant (blue) vs a nine segment (black) pulse. The upper portion is the optimal fidelity curve for each. The lower portion is a plot of a parameter that characterizes the stability of the solutions against detuning fluctuations. To simulate a detuning fluctuation, each pulse shape is applied to neighboring detunings within a small bandwidth. The resulting fidelities are fit to a second order polynomial, and the quadratic coefficient is taken to characterize the stability of the solution. For the regions of interest, where the optimal fidelity curve is maximal, the stability parameter will therefore be small negative numbers, approaching zero for increasingly stable solutions. In the figure, the blue dashed line shows the detuning for the best constant pulse gate, and

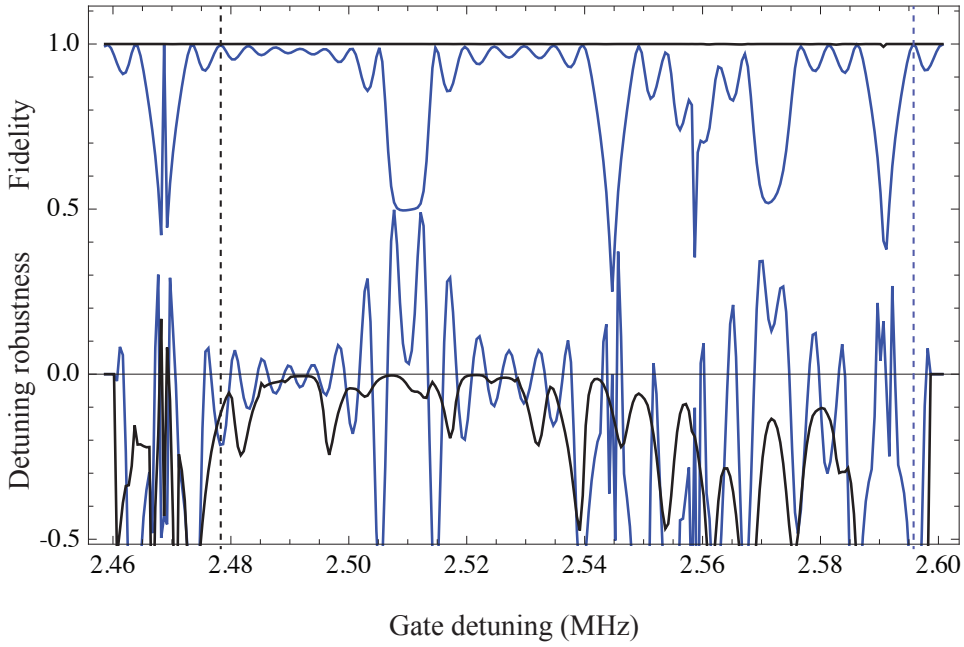

Figure 4.20: Detuning stability comparison.
The detuning stability for constant (blue) vs nine segment (black) pulses on ion pair $\{2, 3\}$. The bottom curves represent the robustness of the pulse solutions to fluctuations in detuning. The magnitude is proportional to the sensitivity of the solution to detuning errors, so closer to zero is more stable. The bandwidth sampled for the polynomial fit is ± 2 kHz.

the black dashed line shows the detuning at which the high fidelity nine segment gate was performed. In the constant pulse case, the stability parameter is very large (literally off the chart), while the nine segment pulse solution is much more stable. It is not surprising then, that given an equal amount of detuning drift in our experiments, the constant pulse gate suffered significantly more. When selecting a detuning to perform a gate, sometimes compromises must be made between the detuning stability and minimizing the required power; hence, the chosen detuning for the nine segment pulse is not quite the most stable point, but it demands less optical power. Fortunately, as the number of segments increases, it is easier to satisfy both of these criteria.

4.7 Suppression of optical spillover effects

As described above, the focused beam profile was not ideal, and the intensity lobe on the one side resulted in significant spillover on the first ion when ion pair $\{2, 3\}$ was addressed. The consequence of spillover is the unintended spin-spin coupling produced between the spillover ion and the target pair. Instead of only one geometric phase term in the gate evolution operator, $\chi_{2,3}$, there are now two additional terms $\chi_{1,2}$ and $\chi_{1,3}$. Given a spillover fraction f, the Rabi rates involved in the terms are simply $\Omega_1\Omega_2 = \Omega_1\Omega_3 = f\Omega_2\Omega_3$. The resulting undesired entanglement with the spillover qubit degrades the fidelity, as this introduces uncontrolled spin-motion entanglement to the system.

The multi-segment pulse scheme provides an opportunistic way to suppress the

effects of this kind of spillover. Using a constant pulse restricts us to effectively one detuning, which couples strongly to the CM mode. The mode coupling parameter for the first ion to this mode is relatively large, so spillover intensity will cause it to accrue non-negligible geometric phase. To suppress this, we choose a detuning between the fourth and fifth modes, to which the first ion couples most weakly. Mathematically, the effective scale factor f is reduced by the additional factor $\eta_{4,1}$ or $\eta_{5,1}$ in the evolution operator.

While this method of suppression is not generally available, it was crucial for allowing us to overcome a technical challenge with the beam focusing, and it was accomplished simply by exploiting the freedom of detuning provided by the segmented pulse scheme.

Chapter 5: Gate sequences with shuttling

After demonstrating the power and versatility of the pulse shaping technique by entangling various pairs of ions in chains of different lengths, we combined the scheme with ion shuttling to demonstrate the programmable nature of our platform by executing sequences of single qubit and pairwise entangling gates. First, we concatenated the two nine segment gates described in the previous chapter to generate a tripartite entangled state of three qubits in a chain of five ions, and we used a method of post-selection to measure all six coherences of the state needed to calculate the state fidelity. Next, we followed the two entangling gates by individual qubit gates to transform the state into a "cat" state. By directly measuring the contrast of the three-qubit parity, we were able to prove that the state exhibited genuine tripartite entanglement. For fun, we also demonstrated a simple Grover search on a two-qubit state immersed in a five ion chain using the same system.

5.1 Tripartite entanglement via sequential gates

In order to execute sequences of gates on different sets of ions in the chain, we had to implement ion shuttling. That is, we displaced the ions along the axial direction by smoothly varying the trapping potential. For this purpose we switched

away from the Iseg EHS-80-05XK3 dc voltage supply used in the two and three ion experiments and instead used a National Instruments PXI-6713 card. The PXI-6713 is a high-speed DAC that can update eight independent output analog voltage channels at a maximum speed of 740 kS/s, which corresponds to a minimum update interval of 1.56 µs. It has a 14-bit DAC, and since the output ranges from ±10 V, the available resolution provides a precision of $10/(2^{(14-1)}) \approx 1$ mV. The card is powered by a PXI-1000 chassis that connects it to the control computer via a PXI-to-PCI interface card. Normally the DAC runs in a static output operating mode. To shuttle the ions, an array of voltages, separated by uniform time intervals, is specified for each electrode. These arrays of voltages as a function of time comprise individual waveforms for the electrodes. The DAC is switched to a triggered output modes such that upon receiving a trigger pulse from the sequencer FPGA, the DAC outputs the waveforms and holds on the final value until it receives another trigger to output the waveform again. Thus, the sequencer FPGA outputs a trigger pulse for each execution of the experimental sequence.

The shuttling waveform is calculated automatically in a relatively simple way. After specifying the voltage sets corresponding to each ion chain configuration in the gate sequence, the voltages are linearly interpolated according to the specified shuttling time, t_s. The duration t_m over which the DAC changes the output from one voltage set to the next is given by $t_m = t_s - t_b$, where t_b is a buffer that allows the ions to complete their motion. In most of the gate sequences, $t_s = 100$ µs and $t_b = 30$ µs. The discrete jumps between the points in the linear ramp are made as small as possible by updating the voltage at the maximum update rate of the

DAC. The π filters before the dc electrodes have a cut-off frequency of $\sim$100 kHz to ensure as little rf voltage leaks onto the dc electrodes as possible. This filter has the side effect of smoothing out voltage changes driven by the DAC. Thus, even though the slew rate of the DAC is on the order of 10 V/µs, a stepwise change to the input voltage takes about 10µs to occur. This works to our advantage. The primary concern when shuttling ions is that the act of applying the static force will heat the motional modes, either directly or indirectly by pushing them off the rf null where the trap rf can add heat [65]. Once the gate sequence has begun after sideband cooling, it is currently impossible for us to cool the qubits again without destroying the quantum state. Theoretically this could be accomplished with ancilla ions in the chain whose sole purpose is to cool the crystal [66], but we do not have this capability. The ions must therefore be moved adiabatically to avoid direct heating. If the shuttling time is much longer than the trap period, and the acceleration is small and smooth at the beginning and end of the transport, then mode heating is avoidable. Our slow, linear ramp between voltages, coupled with the smooth interpolation between the discrete DAC output voltages due to the π filters, satisfies the adiabaticity criteria. Additionally, any small amount of heating would predominantly be to the axial modes, since that is the direction of travel, which would not significantly affect the transverse modes used by the gate.

The voltage sets corresponding to the single and two-qubit gates are determined prior to executing the sequence by statically setting them and adjusting the voltages manually according to the performance of each gate. For the two entangling gates, the position of the ions is adjusted to equalize the carrier Rabi rates

on the target ion pairs. Then the first entangling gate on pair $\{1,2\}$ is performed to determine the required 355 nm power. Using this optical power, the second gate on pair $\{2,3\}$ is performed, scaling the pulse shape as necessary to achieve a good gate. This is necessary because the ion spacing is not uniform, so the equalized intensity on pair $\{2,3\}$ is lower than for $\{1,2\}$. Single qubit rotations require aligning a single ion to the center of the addressing beam and relaxing the axial confinement to separate the ions enough to reduce spillover. The alignment of the ions to the addressing beam is very sensitive to the voltage, and since the ion position drifts on the order of 500 nm/min, the voltage sets need to be optimized as fast as possible before immediately executing the gate sequence.

The state resulting from the application of two sequential entangling gates $U_1(\phi_1)$ on ion pair $\{1,2\}$ and $U_2(\phi_2)$ on $\{2,3\}$ is (neglecting the normalization factors)

$$\begin{aligned}
|\psi_{GHZ}\rangle &= U_2(\phi_2)U_1(\phi_1)|000\rangle \\
&= U_2(\phi_2)\left(|00\rangle - ie^{i\phi_1}|11\rangle\right)|0\rangle \\
&= |000\rangle - ie^{i\phi_2}|011\rangle - e^{i\phi_1}|101\rangle - ie^{i\phi_1}|110\rangle \\
&= \left(|00\rangle - ie^{i\phi_1}|11\rangle\right)|0\rangle - ie^{i\phi_2}\left(|01\rangle - ie^{i(\phi_1-\phi_2)}|10\rangle\right)|1\rangle
\end{aligned} \tag{5.1}$$

This state is genuinely tripartite entangled [67–69] and is in the GHZ class of tripartite entangled states. It has the same type of entanglement as the well known "Schrödinger cat" state with the form $|\psi_{cat}\rangle = \left(|000\rangle + e^{i\phi}|111\rangle\right)/\sqrt{2}$, where ϕ is just some phase. These two states share the same class of entanglement because one

can be transformed to the other by only local operations and classical communication [69]. To transform our state $|\psi_{GHZ}\rangle$ to the cat state, we must shift the phase of the second qubit by $\pi/2$ and then apply a global $\pi/2$ pulse to the three qubits. The qubit phase shift operator $\hat{R}_z(\phi)$ rotates the qubit around the z axis of the Bloch sphere, thereby advancing its phase only. Since our $\hat{\sigma}_\phi$ interaction does not allow this operation directly, we can produce the same result using two $\hat{R}_x$ and one $\hat{R}_y$ operators:

$$\begin{aligned}\hat{R}_z(\phi) &= \hat{R}_{-x}(\pi/2)\hat{R}_y(\phi)\hat{R}_x(\pi/2) \\ &= \hat{R}(\pi/2,\pi)\hat{R}(\phi,\pi/2)\hat{R}(\pi/2,0)\end{aligned}$$

Setting the gate phases to zero for clarity, and defining the global rotation operator $\hat{R}^G(\theta,\phi) \equiv \hat{R}^1(\theta,\phi)\hat{R}^2(\theta,\phi)\hat{R}^3(\theta,\phi)$, the transformation is performed by (again neglecting normalization factors)

$$|\psi_{cat}\rangle = \hat{R}^G(\pi/2,0)\hat{R}_z^2(\pi/2)|\psi_{GHZ}\rangle \tag{5.2a}$$

$$= \hat{R}^G(\pi/2,0)\hat{R}_z^2(\pi/2)\left(|000\rangle - i|110\rangle - i|011\rangle - |101\rangle\right) \tag{5.2b}$$

$$= \hat{R}^G(\pi/2,0)\left(|000\rangle - |110\rangle - |011\rangle - |101\rangle\right) \tag{5.2c}$$

$$= |000\rangle + i|111\rangle \tag{5.2d}$$

The next few sections describe how we measured the fidelity for the state $|\psi_{GHZ}\rangle$ in Eq. 5.1 by using post-selection to extract the required coherence amplitudes from two-qubit parity curves (see Fig. 5.1). Then we applied the transfor-

mation in Eq. 5.2d followed by a global analyzer pulse to measure the three-qubit parity to prove the state was genuinely tripartite entangled (see Fig. 5.2).

5.2 Fidelity measurement using post-selection

The last line of Eq. 5.1 is written the way it is to highlight the structure of the entangled state $|\psi_{GHZ}\rangle$. Any pair of qubits out of the three are in one of two Bell states depending on the state of the remaining qubit. One of the Bell states has odd parity ($|01\rangle + |10\rangle$) and the other has even parity ($|00\rangle + |11\rangle$). This structure makes it possible to measure the necessary coherences of the three-qubit density matrix using parity curves in order to calculate the fidelity of the state. To see how this works, first we look at the ideal state density matrix,

$$\rho_{ideal} = \begin{pmatrix} \frac{1}{4} & 0 & 0 & \frac{i}{4} & 0 & -\frac{1}{4} & \frac{i}{4} & 0 \\ 0 & 0 & 0 & 0 & 0 & 0 & 0 & 0 \\ 0 & 0 & 0 & 0 & 0 & 0 & 0 & 0 \\ -\frac{i}{4} & 0 & 0 & \frac{1}{4} & 0 & \frac{i}{4} & \frac{1}{4} & 0 \\ 0 & 0 & 0 & 0 & 0 & 0 & 0 & 0 \\ -\frac{1}{4} & 0 & 0 & -\frac{i}{4} & 0 & \frac{1}{4} & -\frac{i}{4} & 0 \\ -\frac{i}{4} & 0 & 0 & \frac{1}{4} & 0 & \frac{i}{4} & \frac{1}{4} & 0 \\ 0 & 0 & 0 & 0 & 0 & 0 & 0 & 0 \end{pmatrix} \tag{5.3}$$

and identify the six coherences $\rho_{03}, \rho_{05}, \rho_{06}, \rho_{35}, \rho_{36}$, and ρ_{56}. Given a general three-qubit density matrix ρ_{gen} defined similarly to the two-qubit density matrix in Eq. 4.12,

the fidelity of the experimentally created state is given by $\mathcal{F} = \mathrm{Tr}\left[\rho_{ideal} \cdot \rho_{gen} \cdot \rho_{ideal}^{\dagger}\right]$, which can be written

$$\mathcal{F} = \frac{1}{4}\left(\rho_{00} + \rho_{33} + \rho_{55} + \rho_{66}\right) + \frac{1}{2}\left(A_{03} + A_{05} + A_{06} + A_{35} + A_{36} + A_{56}\right) \qquad (5.4)$$

if the phases of the coherences are allowed to be free parameters. In other words, for the purpose of measuring how well the tripartite entangled state was produced, the amplitudes of the coherences are all that really matter. The phases are critically important, however, for the transformation to the cat state as discussed in the next section.

Post-selection is the process of reducing the density matrix based on knowledge of a qubit state. In the pure state of Eq. 5.2b, a post-selection of the third qubit in the $|1\rangle$ state means that the first two qubits were in the state $|01\rangle - ie^{i(\phi_1 - \phi_2)}|10\rangle$. A post-selection of the third qubit in the $|0\rangle$ state means that the first two qubits were in the state $|00\rangle - ie^{i\phi_1}|11\rangle$. This method is distinct from projection, in which the state of the third qubit is measured before disturbing the coherence of the other two, resulting in the probabilistic collapse of the two-qubit state into either of the Bell states depending on the measured state of the third. Post-selection is performed after the qubit states have all been measured.

To extract the coherences for the fidelity, we generated six unique two-qubit parity curves after creating the ρ_{GHZ} state by scanning the phase of one or both of the analyzer pulses we applied to each two-qubit subset of the three entangled qubits. For example, if we apply analyzer pulses to qubits 2 and 3 of the general

state ρ_{gen} and scan the phases of both, then post-select the data in which qubit 1 is in the $|0\rangle$ state, the resulting parity curve is:

$$\begin{aligned}\Pi(\phi) &= \text{Select}[|0\rangle_1]\hat{R}^2(\theta,\phi)\hat{R}^3(\theta,\phi)|\psi_{GHZ}\rangle \\ &= \frac{1}{\rho_{00}+\rho_{11}+\rho_{22}+\rho_{33}} 2\left(A_{12}\cos\left(\phi_{12}\right) - A_{03}\cos\left(2\phi+\phi_{03}\right)\right)\end{aligned}$$

As before, the two-qubit parity curve is a sinusoid of period π with an amplitude proportional to a coherence, with an offset given by the amplitude and phase of another coherence. For the ideal state, this operation yields a sinusoid with an amplitude equal to that of the coherence ρ_{03}. If instead we post-select the $|1\rangle$ state for qubit 1, and only scan the phase of one of the analyzer pulses, the parity curve becomes

$$\begin{aligned}\Pi(\phi) &= \text{Select}[|1\rangle_1]\hat{R}^2(\theta,\phi)\hat{R}^3(\theta,0)|\psi_{GHZ}\rangle \\ &= \frac{1}{\rho_{00}+\rho_{11}+\rho_{22}+\rho_{33}} 2\left(A_{56}\cos\left(\phi+\phi_{56}\right) - A_{47}\cos\left(\phi+\phi_{47}\right)\right)\end{aligned}$$

This parity curve is slightly different, in that the periodicity of the sinusoid is 2π instead of π, and the undesired coherence ρ_{47} contributes a competing sinusoid (depending on its phase) instead of simply adding an offset. The important point is that for small values of ρ_{47}, the parity curve amplitude measures the desired coherence ρ_{56}. The other four permutations of post-selecting the state of qubits 2 and 3 in states $|0\rangle$ and $|1\rangle$ yield parity curves proportional to the remaining four coherences required to measure the fidelity of the state $|\psi_{GHZ}\rangle$.

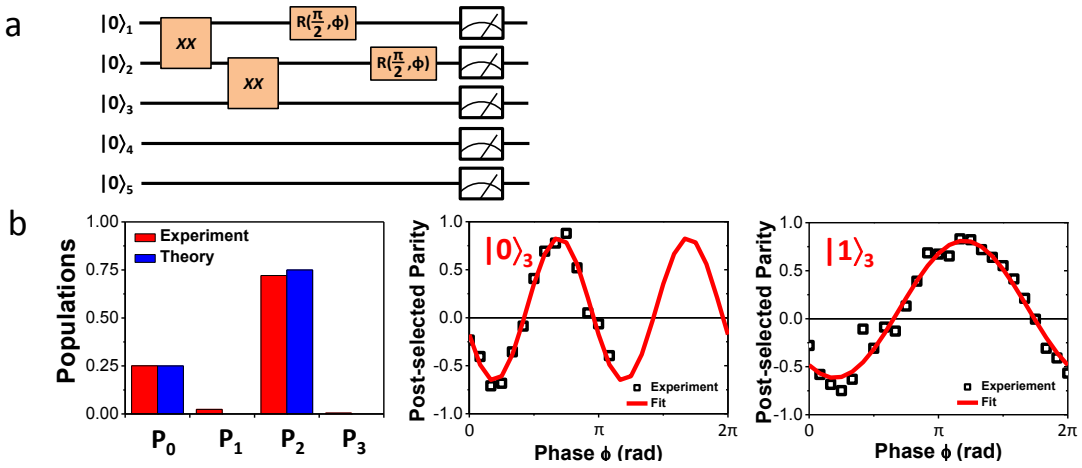

Figure 5.1: Post-selected parity curve and the measured populations. (a) The gate sequence, including the analyzer pulse to generate the parity curves. (b) An example of the population and parity curve contrast data to measure two coherence amplitudes.

The parity curves required individual addressing of two out of the five qubits, due to the fact the post-selected qubit could not be allowed to rotate while the analyzer pulse was applied to the other two. Figure 5.1(a) illustrates the procedure by showing the gate sequence for measuring the two-qubit parity between qubits 1 and 2 while post-selecting on qubit 3. The ideal state populations have 75% in a state with two bright ions and 25% in a state with all dark. Part (b) of the figure shows the measured populations and the two parity curves measured.

The final state fidelity we calculated after measuring the populations and the six coherences was 79%. This value is very close to what we expected, given that each gate fidelity was about 95% and the post-selection procedure had a 7% error ($95\% \times 95\% \times 93\% = 84\%$). The error in the post-selection was a direct consequence of our pathological bright state histogram (see Sec. 2.4.3). The post-selection process is a "single shot" determination of the state of a qubit based on the number of photons

collected during the detection cycle. Our optimized state detection fidelity using this method of discrimination was abnormally low due to the mysterious optical pumping of the bright state during the detection cycle that we were unable to suppress.

5.3 Proving genuine tripartite entanglement

To demonstrate the programmable nature of our system, we performed the gate sequence in Eq. 5.2d to create a cat state and then proved that the state was genuinely tripartite entangled by measuring the amplitude of the three-qubit parity curve. The successful application of this gate sequence required careful calibration and control of the optical phase at each ion for each gate. As mentioned in Ch. 3, the optical phase is mapped onto the entangled state and also directly determines the phase of the individual qubit rotations. For ions in a constant position relative to the Raman beams, the phases can simply by defined as zero and are no longer a concern. For our gate sequences, however, the two-qubit entangling gates and the single qubit gates see different optical phases because the ion positions change with respect to the laser beam for each gate.

We measured the phase shift across the addressing beam profile by applying two $\pi/2$ pulses to a single ion at different positions relative to the center of the beam, compensating for the variation in Rabi rate due to the drop in intensity. By scanning the phase of the $\pi/2$ pulse at the displaced position, the resulting Ramsey type fringes are shifted by the difference in optical phase between the two positions. A simple sinusoidal fit yields the phase offset as a function of displacement. The

measured profile was consistent with a misalignment of the $\Delta\mathbf{k}$ by about 1°, for which the optical phase shifts about 45° over ∼2 µm, with some distortion due to spherical aberrations on the beam.

In addition to the operations required to create the cat state in Eq. 5.2d, we applied an analyzer pulse to each qubit as shown in Fig. 5.2. The parity curve in the figure was produced by scanning the phase of these analyzer pulses together and plotting the three-qubit parity given by

$$\Pi_3(\rho) \equiv (\rho_{00} + \rho_{33} + \rho_{55} + \rho_{66}) - (\rho_{11} + \rho_{22} + \rho_{44} + \rho_{77})$$

The fitting of the state detection histograms for the three-qubit state required the additional basis histogram for the $|111\rangle$ state. Thus, the parity is calculated experimentally by the sum $P_0+P_2-(P_1+P_3)$, where the populations P_j are determined by fitting the histograms as described in Sec. 2.4.3. If the contrast of this parity curve is above 50%, the coherence ρ_{07} of the three qubit density matrix is large enough to prove that the state has genuine tripartite entanglement. By fitting the measured parity curve to a simple sinusoid of periodicity $2\pi/3$, we calculated a contrast of ∼70%.

The parity curve contrast is the strictest possible measure of the entanglement and is highly susceptible to the various gate errors. Figure 5.2 also shows a simulated curve (blue) of the parity curve we would expect given a *perfect* cat state but including known errors in our single qubit gates. Specifically, these errors are the result of the fact that the ion position drifted due to charging issues as mentioned

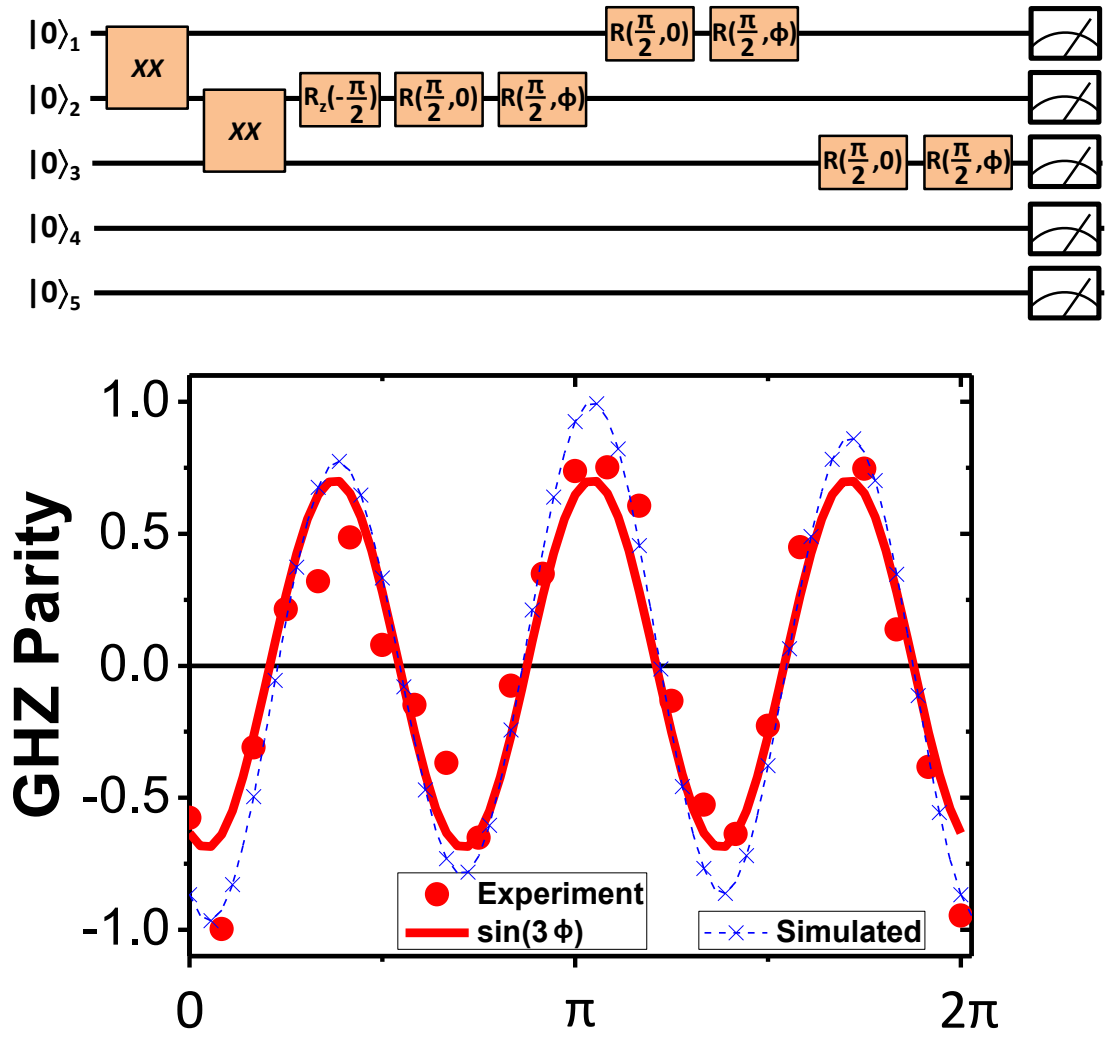

Figure 5.2: Three-qubit parity curve showing genuine tripartite entanglement. (top) Gate sequence on the five ion chain. XX denotes the entangling gate and R_z denotes the $R_{-x}R_yR_x$ rotations that produce a z rotation. (bottom) The cat state parity curve. The red curve is a strict sinusoid fit with frequency 3. The dashed blue curve is a simulated parity curve assuming a perfect cat state but accounting for known gate errors.

earlier. This drift caused errors in the rotations because the the intensity at the ions changed, leading to under-rotations on the order of 5-10%. Additionally, the position drift shifted the optical phase on the ion, causing a phase error on the order of 10°. The resulting curve manifests asymmetries in the shape that are not intuitively obvious but that match our measured curve fairly well. This leads us to conclude that our actual cat state fidelity was significantly higher than the strict parity curve fit would suggest.

5.4 Simple Grover search algorithm on two qubits

The gate sequence we used to perform the cat state experiment is similar in complexity to the sequence required to execute the simplest Grover search algorithm on two qubits in a chain of five ions. Without going into more detail than necessary, the Grover search algorithm is a method of searching an unsorted database quadratically faster than any current classical algorithm [9]. The perhaps over-used analogy is searching a phonebook of N entries for a name based given a known phone number. Classically this would take on the order of N queries, but if the correlation between the names and numbers were encoded in qubits, the Grover search algorithm would only require on the order of $\sqrt{N}$ queries. Brickman describes in her thesis [70] how to implement the algorithm in a simple way on a two-qubit system. We reproduced a small portion of her results using the method she details. The gate sequence is shown in Fig. 5.3, displaying only the two target qubits since the other three are simply spectators that complicate the mode structure in this

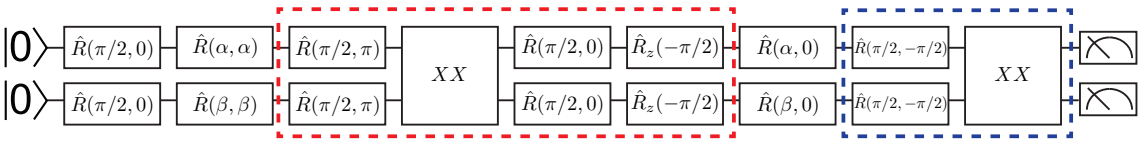

Figure 5.3: Grover search algorithm on two qubits.
The red dashed box comprises the "oracle" that marks the desired state by inverting its phase relative to the other states. The blue dashed box is the amplification stage.

demonstration. The algorithm is as follows: After initializing the qubits to the $|0\rangle$ state, a $\pi/2$ pulse is applied to both ions to place them in an equal superposition of all four two-qubit basis states. This state represents the database of four elements that will be searched. The rotations $\hat{R}(\alpha,\alpha)$ and $\hat{R}(\beta,\beta)$ select which of the four entries are to be found. The values $\alpha = \beta = 0$ correspond to a search for the state $|11\rangle$. The next sequence of gates, enclosed by the dashed red line, execute a controlled-Z gate that "marks" the desired state by flipping its phase relative to the other states. This part of the algorithm is called the "oracle". Once marked, an amplification step is performed that increases the population in the search query state (if the state is indeed in the database). This step is repeated as many times as necessary to reach a sufficient level of certainty about whether or not the query was found. In the two-qubit case, only one amplification step is required to provide 100% certainty about whether or not the state has been found. This step is outlined by the dashed blue line. It consists of another $\pi/2$ pulse on each ion followed by a second entangling gate.

The resulting population in state $|11\rangle$ was measured to be 70(2)%, with 16(2)% in the odd parity states and the remainder in the $|00\rangle$ state. The search was thus

successful, and the algorithm unambiguously exceeded the classical limit of 50%. It is unclear why the value is so much lower than the ∼90% expected based on the gate fidelity and the fact that this search did not require shuttling. Unfortunately, we did not have much time to troubleshoot this fun side project as we were beginning work on the next version of our linear trapped ion crystal quantum information processor, which is described in the next chapter.

Chapter 6: Outlook

Virtually all of the errors and limitations of our current system are due to the ion trap and chamber design; the chamber was simply not designed for these experiments. We are in the process of constructing a new ion trap and chamber suited beautifully to our needs, and in this brief chapter a description of the new apparatus is presented.

6.1 Improved ion trap and vacuum chamber

The new ion trap is a "blade" trap, consisting of four planar electrodes arranged into a geometry with a cross section resembling an 'X'. The angle and spacing of the blades are configured to provide high numerical apertures for both the counter-propagating Raman beams, which are aligned in the horizontal direction perpendicular to the ion chain, and the imaging objective, which collects fluorescence perpendicular to the chain in the vertical direction. Two opposing blades each have five dc electrodes, with a total length sufficient to ensure a high degree of linearity to the trap potential. Five electrodes will allow for the application of a quartic term to the axial potential to enable uniform ion spacing in chains with more ions, which will be critical for both individual addressing and individual state detection

with the multichannel PMT array. The other two blades supply the rf voltages and are independently dc biased to provide principal axis rotation. Reentrant viewports will allow the focusing objectives for both Raman beams to achieve sub-micron spot sizes for ideal individual addressing with exceptionally low spherical aberration on the beams, drastically reducing spillover on neighboring qubits and charging from 355 nm scatter on the trap electrodes and assembly. Optical access along the ion chain axis will allow for extremely uniform intensities of the 369 nm optical pumping and detection beams with maximally efficient use of available optical power. This will be important as more of the 369 nm power must be diverted to the cooling beam for holding long chains. The vacuum chamber sports a new ion pump with an integrated NEG cartridge *, as well as vastly superior vacuum conductance between the ion pump and the spherical cube that houses the ion trap. Additionally, strips of NEG material will be placed nearby the ion trap assembly to add strong local pumping. The enhanced quality of the vacuum will be necessary for longer chains to remain crystallized long enough to perform complex gate sequences. The Yb ovens will be small resistively heated metallic tubes positioned relatively far from the trap assembly and having no thermal contact with it. This should aid in maintaining stable motional mode frequencies independent of loading duty cycles.

6.2 True arbitrary pair entanglement

Currently there is only one addressing beam, limiting us to performing entangling gates between adjacent pairs only. True arbitrary two-qubit gates require two

*SAES NEXTorr pump

addressing beams, assuming the counterpropagating Raman beam is still a global one. Given that the act of cleanly focusing onto single ions should be relatively trivial in the new design, there are multiple ways we can implement arbitrary sequences of single and two-qubit gates. The first way is by combining our shuttling capability with a stationary addressing beam and a dynamic addressing beam steered by an EO deflector*. One ion in the target pair can be aligned to the stationary beam by shuttling the entire chain. The other ion would be addressed by deflecting the dynamic beam using the EO deflector. Since the beam deflection is proportional to a ± 2 V analog signal input to the EO deflector controller, the DAC system that generates the shuttling waveforms can be duplicated to drive the EO deflector in identical and parallel fashion.

Alternatively, we are exploring the possibility of using a unique multi-channel AOM† that could produce up to 32 independently controllable 355 nm beams from a single input. The array of beams could be focused in parallel with fixed alignment to each ion in the crystal, with one or more AWGs multiplexed to simultaneously drive the appropriate channels for a specified gate. The obvious advantage to this scheme is that the slow down and complications associated with shuttling disappear, but probably at the cost of focused beam quality. There is a recent proposal [71] that would be perfectly suited to this system. Using multiple phase coherent beams to address ions neighboring the target ions, it should be possible to cancel spillover from the primary beam by careful calibration of the extra beam amplitudes. These

*ConOptics Model M310A
†Harris Model H-601

compensation beams need not be perfectly aligned or have ideal mode profiles either; they simply need to be coherent and stationary. Such a scheme would require some additional laser power as well as either additional AWGs or low-noise, dynamic rf attenuators since the compensation beam amplitudes should have fixed ratios with respect to the primary beam.

6.3 Conclusion

The experiments detailed in this thesis are exciting for both the trapped ion quantum information community and for our lab's future. They benefit the community by conclusively demonstrating the power and versatility of the pulse shaping technique for improving the fidelity of entangling gates on trapped ion chains. For our research group, the hardware and software developed to make the experiments possible comprise an essentially complete toolbox for performing arbitrary gate sequences in future experiments. The potential for the variety of physics we can do with such a system is limited only by our creativity and the support of theorists.

Bibliography

[1] J. Sterk, L. Luo, T. Manning, P. Maunz, and C. Monroe, "Photon collection from a trapped ion-cavity system," *Physical Review A*, vol. 85, no. 6, p. 062308, 2012.

[2] "Climbing mount everest is work for supermen," *New York Times*, March 18 1923.

[3] E. Schrödinger, "Die gegenwärtige situation in der quantenmechanik," *Naturwissenschaften*, vol. 23, pp. 807–812, 1935.

[4] A. Einstein, B. Podolsky, and N. Rosen, "Can quantum-mechanical description of physical reality be considered complete?," *Phys. Rev.*, vol. 47, pp. 777–780, May 1935.

[5] R. P. Feynman, "Simulating physics with computers," *International Journal of Theoretical Physics*, vol. 21, p. 467, 1982.

[6] D. Deutsch, "Quantum theory, the church-turing principle and the universal quantum computer," *Proc. Royal Society of London A*, vol. 400, p. 97, 1985.

[7] P. Shor, "Algorithms for quantum computation: discrete logarithms and factoring," in *Proc. 35th Ann. Sym. Found. Comp. Sci.*, p. 124, 1994.

[8] D. Deutsch and R. Jozsa, "Rapid solution of problems by quantum computation," *Proc. R. Soc. Lond. A*, vol. 439, pp. 553–558, 1992.

[9] L. K. Grover, "Quantum mechanics helps in searching for a needle in a haystack," *Phys. Rev. Lett.*, vol. 79, pp. 325–328, Jul 1997.

[10] K.-A. Brickman, P. C. Haljan, P. J. Lee, M. Acton, L. Deslauriers, and C. Monroe, "Implementation of grover's quantum search algorithm in a scalable system," *Phys. Rev. A*, vol. 72, p. 050306, Nov 2005.

[11] S. Gulde, *Experimental realization of quantum gates and the deutsch-josza algorithm with trapped 40Ca+ ions*. Doctoral thesis, Universität Innsbruck, 2003.

[12] P. W. Shor, "Fault-tolerant quantum computation," *Proc. 37th Annual Symposium on Foundations of Computer Science*, pp. 56–65, 1996.

[13] A. Steane, "The ion trap quantum information processor," *Applied Physics B*, vol. 64, no. 6, pp. 623–643, 1997.

[14] J. S. Bell, "On the einstein podolsky rosen paradox," *Physics*, vol. 1, p. 195, 1964.

[15] S. J. Freedman and J. F. Clauser, "Experimental test of local hidden-variable theories," *Phys. Rev. Lett.*, vol. 28, pp. 938–941, Apr 1972.

[16] A. Aspect, P. Grangier, and G. Roger, "Experimental realization of einstein-podolsky-rosen-bohm gedankenexperiment: A new violation of bell's inequalities," *Phys. Rev. Lett.*, vol. 49, pp. 91–94, Jul 1982.

[17] J. F. Clauser, M. A. Horne, A. Shimony, and R. A. Holt, "Proposed experiment to test local hidden-variable theories," *Phys. Rev. Lett.*, vol. 23, pp. 880–884, Oct 1969.

[18] D. P. DiVincenzo, "The physical implementation of quantum computation," *Fortschr. Phys.*, vol. 48, p. 771, 2000.

[19] T. D. Ladd, F. Jelezko, R. Laflamme, Y. Nakamura, C. Monroe, and J. L. O'Brien, "Quantum computers," *Nature*, vol. 464, pp. 45–53, March 2010.

[20] C. Monroe and J. Kim, "Scaling the ion trap quantum processor," *Science*, vol. 339, no. 6124, pp. 1164–1169, 2013.

[21] M. A. Nielsen and I. L. Chuang, *Quantum Computation and Quantum Information*. Cambridge University Press, 2000.

[22] C. Monroe, R. Raussendorf, A. Ruthven, K. R. Brown, P. Maunz, L.-M. Duan, and J. Kim, "Large scale modular quantum computer architecture with atomic memory and photonic interconnects," *arXiv:1208.0391 [quant-ph]*, 2012.

[23] P. T. H. Fisk, M. J. Sellars, M. A. Lawn, and C. Coles, "Accurate measurement of the 12.6 ghz "clock" transition in trapped $^{171}yb^{+}$ ions," *IEEE Trans. Ultrasonics, Ferroelectrics, and Frequency Control*, vol. 44, p. 344, 1997.

[24] R. Casdorff, V. Enders, R. Blatt, W. Neuhauser, and P. E. Toschek, "A 12-ghz standard clock on trapped ytterbium ions," *Annalen der Physik*, vol. 503, no. 1-3, pp. 41–55, 1991.

[25] H. G. Dehmelt, "Radiofrequency spectroscopy of stored ions i: storage," *Adv. At. Mol. Phys.*, vol. 3, p. 53, 1967.

[26] W. Paul, "Electromagnetic traps for charged and neutral particles," *Rev. Mod. Phys.*, vol. 62, p. 531, 1990.

[27] P. Lucey, Korotev, R. L, and et al., "Understanding the lunar surface and space-moon interactions," *Reviews in Mineralogy and Geochemistry*, vol. 60, p. 83, 2006.

[28] P. Langevin *Ann. Chem. Phys.*, vol. 5, p. 245, 1905.

[29] D. J. Griffiths, *Introduction to Electrodynamics*. Prentice Hall, 3rd ed., 1999.

[30] M. G. RAIZEN, J. M. GILLIGAN, W. M. I. J. C. BERGQUIST, and D. J. WINELAND, "Linear trap for high-accuracy spectroscopy of stored ions," *Journal of Modern Optics*, vol. 39, no. 2, pp. 233–242, 1992.

[31] W. K. Hensinger, S. Olmschenk, D. Stick, D. Hucul, M. Yeo, M. Acton, L. Deslauriers, J. Rabchuk, and C. Monroe, "T-junction ion trap array for two-dimensional ion shuttling, storage and manipulation," *App. Phys. Lett.*, vol. 88, p. 034101, 2006.

[32] W. W. Macalpine and R. O. Schildknecht, "Coaxial resonators with helical inner conductor," *Proc. IRE*, p. 2099, 1959.

[33] A. I. Zverev and H. J. Blinchikoff, "Realization of a filter with helical components," *IRE Trans. Compon. Parts*, vol. Sept., p. 99, 1961.

[34] M. Madsen, *Advanced Ion Trap Development and Ultrafast Laser-Ion Interactions*. Doctoral thesis, University of Michigan, 2006.

[35] L. Deslauriers, *Cooling and Heating of the Quantum Motion of Trapped Cd+ Ions*. Doctoral thesis, University of Michigan, 2006.

[36] P. M. Fitzpatrick, *Advanced Calculus: A Course in Mathematical Analysis*. PWS Publishing Company, 1st ed., 1996.

[37] J. Mizrahi, *Ultrafast Control of Spin and Motion in Trapped Ions*. Doctoral thesis, University of Maryland, 2013.

[38] W. C. Campbell, J. Mizrahi, Q. Quraishi, C. Senko, D. Hayes, D. Hucul, D. N. Matsukevich, P. Maunz, and C. Monroe, "Ultrafast gates for single atomic qubits," *Phys. Rev. Lett.*, vol. 105, p. 090502, Aug 2010.

[39] D. T. C. Allcock, J. A. Sherman, D. N. Stacey, A. H. Burrell, M. J. Curtis, G. Imreh, N. M. Linke, D. J. Szwer, S. C. Webster, A. M. Steane, and D. M. Lucas, "Implementation of a symmetric surface-electrode ion trap with field compensation using a modulated raman effect," *New J. Phys.*, vol. 12, p. 053026, 2010.

[40] D. H. E. Dubin, "Theory of structural phase transitions in a trapped coulomb crystal," *Phys. Rev. Lett.*, vol. 71, pp. 2753–2756, Oct 1993.

[41] J. P. Schiffer, "Phase transitions in anisotropically confined ionic crystals," *Phys. Rev. Lett.*, vol. 70, pp. 818–821, Feb 1993.

[42] D. J. Berkeland, J. D. Miller, J. C. Bergquist, W. M. Itano, and D. J. Wineland, "Minimization of ion micromotion in a paul trap," *J. Appl. Phys.*, vol. 83, p. 5025, 1998.

[43] J. Song, Q. An, and S. Liu, "A high-resolution time-to-digital converter implemented in field-programmable-gate-arrays," *Nuclear Science, IEEE Transactions*, vol. 56, p. 236, 2006.

[44] W. M. Itano and D. J. Wineland, "Laser cooling of ions stored in harmonic and penning traps," *Phys. Rev. A*, vol. 25, pp. 35–54, Jan 1982.

[45] D. J. Wineland, C. Monroe, W. M. Itano, D. Leibfried, B. E. King, and D. M. Meekhof, "Experimental issues in coherent quantum-state manipulation of trapped atomic ions," *Journal of Research of the National Institute of Standards and Technology*, vol. 103, p. 259, 1998.

[46] D. J. Wineland and W. M. Itano, "Laser cooling of atoms," *Phys. Rev. A*, vol. 20, pp. 1521–1540, Oct 1979.

[47] R. D. Cowan, *The Theory of Atomic Structure and Spectra*. University of California Press, 1981. Details of the level coupling notation can be found here, e.g. pages 128-132.

[48] D. J. Berkeland and M. G. Boshier, "Destabilization of dark states and optical spectroscopy in zeeman-degenerate atomic systems," *Phys. Rev. A*, vol. 65, p. 033413, 2002.

[49] M. Acton, K.-A. Brickman, P. C. Haljan, P. J. Lee, L. Deslauriers, and C. Monroe, "Near-perfect simultaneous measurement of a qubit register," *Phys. Rev. A*, vol. 65, p. 033413, 2002.

[50] A. Lee, "Ytterbium ion qubit state detection on an iccd camera," undergraduate thesis, University of Maryland, 2012.

[51] E. D. Black, "An introduction to pound-drever-hall laser frequency stabilization," *Am. J. Phys.*, vol. 69, p. 79, 2001.

[52] A. Chew, "Doppler-free spectroscopy of iodine at 739nm," undergraduate thesis, University of Maryland, 2008.

[53] P. J. Lee, *Quantum information processing with two trapped cadmium ions*. Doctoral thesis, University of Michigan, 2006.

[54] D. Hayes, *Remote and Local Entanglement of Ions using Photons and Phonons*. Doctoral thesis, University of Maryland, 2012.

[55] D. Hayes, D. N. Matsukevich, P. Maunz, D. Hucul, Q. Quraishi, S. Olmschenk, W. Campbell, J. Mizrahi, C. Senko, and C. Monroe, "Entanglement of atomic qubits using an optical frequency comb," *Phys. Rev. Lett.*, vol. 104, p. 140501, Apr 2010.

[56] R. K. Islam, *Quantum Simulation of Interacting Spin Models with Trapped Ions*. Doctoral thesis, University of Maryland, 2013.

[57] R. Islam, W. C. Campbell, T. Choi, S. M. Clark, S. Debnath, E. E. Edwards, B. Fields, D. Hayes, D. Hucul, I. V. Inlek, K. G. Johnson, S. Korenblit, A. Lee, K. W. Lee, T. A. Manning, D. N. Matsukevich, J. Mizrahi, Q. Quraishi, C. Senko, J. Smith, and C. Monroe, "Beat note stabilization of mode-locked lasers for quantum information processing," *ArXiv e-prints*, Dec. 2013.

[58] L. Allen and J. Eberly, *Optical Resonance and Two-level Atoms*. Dover Books on Physics Series, Dover, 1987.

[59] D. F. V. James, "Quantum dynamics of cold trapped ions with application to quantum computation," *Appl. Phys. B*, vol. 66, p. 181, 1998.

[60] C. Marquet, F. Schmidt-Kaler, and D. F. V. James, "Phonon-phonon interactions due to non-linear effects in a linear ion trap," *Appl. Phys. B*, vol. 76, p. 199, 2003.

[61] A. Sørensen and K. Mølmer, "Quantum computation with ions in thermal motion," *Phys. Rev. Lett.*, vol. 82, p. 1971, 1999.

[62] K. Mølmer and A. Sørensen, "Multiparticle entanglement of hot trapped ions," *Phys. Rev. Lett.*, vol. 82, p. 1835, 1999.

[63] S.-L. Zhu, C. Monroe, and L.-M. Duan, "Arbitrary-speed quantum gates within large ion crystals through minimum control of laser beams," *EPL (Europhysics Letters)*, vol. 73, no. 4, p. 485, 2006.

[64] S.-L. Zhu, C. Monroe, and L.-M. Duan, "Trapped ion quantum computation with transverse phonon modes," *Phys. Rev. Lett.*, vol. 97, p. 050505, Aug 2006.

[65] D. Hucul, M. Yeo, W. K. Hensinger, J. Rabchuk, S. Olmschenk, and C. Monroe, "On the transport of atomic ions in linear and multidimensinal ion trap arrays," *Quant. Inf. Comp.*, vol. 8, p. 501, 2008.

[66] G. D. Lin, S. L. Zhu, R. Islam, K. Kim, M. S. Chang, S. Korenblit, C. Monroe, and L. M. Duan, "Large-scale quantum computation in an anharmonic linear ion trap," *Europhys. Lett.*, vol. 86, p. 60004, 2009.

[67] A. I. Solomon and C.-L. Ho, "Condition for tripartite entanglement," in *Journal of Physics: Conference Series*, vol. 343, p. 012114, IOP Publishing, 2012.

[68] O. Gühne and M. Seevinck, "Separability criteria for genuine multiparticle entanglement," *New Journal of Physics*, vol. 12, no. 5, p. 053002, 2010.

[69] O. Gühne and G. Toth, "Entanglement detection," *Physics Reports*, vol. 474, no. 1-6, pp. 1–75, 2009.

[70] K. A. Brickman, *Implementation of Grover?s Quantum Search Algorithm with Two Trapped Ions*. Doctoral thesis, University of Michigan, 2007.

[71] C. Shen, Z.-X. Gong, and L.-M. Duan, "Individual addressing in quantum computation through spatial refocusing," *Phys. Rev. A*, vol. 88, p. 052325, Nov 2013.